

Utah State University

DigitalCommons@USU

All Graduate Theses and Dissertations


Graduate Studies

8-1995

Structure and Interaction Energies of Kr Atoms Adsorbed on Graphitic Amorphous Carbon

Sang -Joon Lee
Utah State University

Follow this and additional works at: <https://digitalcommons.usu.edu/etd>

 Part of the [Physics Commons](#)

Recommended Citation

Lee, Sang -Joon, "Structure and Interaction Energies of Kr Atoms Adsorbed on Graphitic Amorphous Carbon" (1995). *All Graduate Theses and Dissertations*. 2091.

<https://digitalcommons.usu.edu/etd/2091>

This Thesis is brought to you for free and open access by the Graduate Studies at DigitalCommons@USU. It has been accepted for inclusion in All Graduate Theses and Dissertations by an authorized administrator of DigitalCommons@USU. For more information, please contact digitalcommons@usu.edu.



STRUCTURE AND INTERACTION ENERGIES OF Kr ATOMS
ADSORBED ON GRAPHITIC AMORPHOUS CARBON

by

SANG-JOON LEE

A thesis submitted in partial fulfillment
of the requirements for the degree

of

MASTER OF SCIENCE

in

Physics

Approved:

John Robert Dennison
Major Professor

D. Mark Riffe
Committee Member

Jan J. Sojka
Committee Member

James P. Shaver
Dean of Graduate Studies

UTAH STATE UNIVERSITY
Logan, Utah

1995

Copyright © SANG-JOON LEE 1995

All rights reserved

ABSTRACT

Structure and Interaction Energies of Kr Atoms Adsorbed on

Graphitic Amorphous Carbon

by

Sang-Joon Lee, Master of Science

Utah State University, 1995

Major Professor: Dr. John Robert Dennison
Department: Physics

The physisorption of Kr on graphitic amorphous carbon (g-C) has been investigated using a statistical approach. The interaction energy calculation process (i) established a structural model of g-C and (ii) determined the adsorbate-adsorbate and the adsorbate-substrate interaction potentials on g-C.

The structural model of g-C was divided into three regions. For the interaction potential between a Kr atom and a carbon atom, the short and medium range order of g-C was described with a discrete medium model based on three ring clusters using ring statistics from Beeman's continuous random network C1120 model of g-C. For the intermediate distance region, Beeman's radial distribution function was used to model g-C. A homogeneous and isotropic continuous medium model was used at large distances.

The Kr - Kr and Kr - g-C interaction potentials used for Kr on g-C, which are pair-wise Lennard-Jones 6-12 potentials, are similar to Kr on graphite potentials. The

validity of the model for g-C and the potentials were verified through calculations for Kr on graphite. Results compared favorably with recent literature values.

The interaction energy calculation results for Kr on a g-C substrate assert that (i) Kr adlayers will form on g-C, (ii) the structure of the Kr adlayer is governed by the substrate corrugation at low coverage and by the Kr - Kr interaction at high coverage, and (iii) there is no direct relation between the structure of Kr adlayers on g-C and those on graphite. The average binding energy of Kr on g-C is comparable with that on graphite, but the corrugation of g-C is perhaps six times that of a graphite substrate. The wrinkling of the g-C surface, due to the presence of a distribution of 5-, 6-, and 7-membered rings, is responsible for this large corrugation of the g-C substrate.

(166 pages)

ACKNOWLEDGMENTS

I wish to thank Dr. John Robert Dennison for his guidance, support, and encouragement throughout the course of this thesis research. His advice, wisdom, and support are deeply appreciated. I also wish to acknowledge Dr. D. Mark Riffe and Dr. Jan J. Sojka for their invaluable advice and support. I would like to thank Dr. Greg Swain for his guidance in the scanning tunneling microscopy measurements. I would also like to thank Dr. Chao Gao for providing the results of optical interferometry measurements. To my friends (especially to Kwangsoo Kim and Ali Sabbah), I wish to say thanks for their humor, encouragement, and support. I wish to thank my parents, brothers, and sister for their constant concern and encouragement. Finally, I would like to express my deepest gratitude to my wife, Sung-Hye Kwon, and daughters, Min-Ah and Minryoung, for their love and patience.

Sang-Joon Lee

CONTENTS

	Page
ABSTRACT	ii
ACKNOWLEDGMENTS	iv
LIST OF TABLES	vii
LIST OF FIGURES	iv
LIST OF DEFINITIONS	xiii
CHAPTER	
1. INTRODUCTION	1
A. Adsorption of rare gases on graphite.....	1
B. Adsorption on amorphous substrates.....	3
C. Thesis objectives	6
2. STRUCTURE AND STRUCTURAL MODEL OF GRAPHITIC AMORPHOUS CARBON	10
A. Necessity of a structural model of graphitic amorphous carbon	10
B. Structure and physical properties of graphite	12
C. Structure and properties of graphitic amorphous carbon	12
D. The surface structure of graphitic amorphous carbon	28
E. Structural model for interaction energy calculations	42
3. INTERACTION ENERGY CALCULATION	55
A. Introduction	55
B. The Lennard-Jones 6-12 potential	56
C. Kr - C-atom interaction potential on g-C	56
D. Interaction potential between two Kr atoms on g-C	58
E. Methods of interaction energy calculations on graphitic amorphous carbon	63
F. Kr- graphite interaction energy calculation	66
G. Interaction energy calculation results on g-C	71
4. DISCUSSION: Kr ON GRAPHITIC AMORPHOUS CARBON	90
A. Discussion about Kr-g-C interaction energy calculation	90
B. Prediction of the structures of Kr adlayers	102

C. Limitation of the model of g-C	104
5. CONCLUSIONS	108
REFERENCES	110
APPENDICES	115
APPENDIX 1: CALCULATION OF INTERACTION ENERGY BETWEEN Kr AND GRAPHITE ALONG THE SYMMETRIC LINE OF A HEXAGON	116
APPENDIX 2: CALCULATION OF RING STATISTICS AND THREE RING CLUSTER PROBABILITY DISTRIBUTION	119
APPENDIX 3: DETERMINATION OF THE COORDINATES OF CARBON ATOMS OF DISCRETE MEDIUM MODEL	123
APPENDIX 4: CALCULATION OF INTERACTION ENERGY BETWEEN A Kr ATOM AND A SEMI-INFINITE GRAPHITE WITH CMM	137
APPENDIX 5: INTERACTION ENERGY OF A SINGLE Kr ATOM WITH A 2D TRIANGULAR LATTICE OF Kr ATOMS	139
APPENDIX 6: CALCULATION OF POTENTIAL ENERGY SUMMATION FOR A Kr ATOM ABOVE A CARBON RING	141

LIST OF TABLES

Table		Page
I	Physical properties of graphite, typical g-C samples, and ACF g-C films.....	14
II	Room temperature conductivity (σ), energy gap, (E_g) density (ρ) and hardness of typical glassy carbon, evaporated a-C, ion-beam a-C, and a-C:H samples.....	16
III	Physical properties of graphite, diamond and a-C's. n_1 , r_1 , r_2 , and ρ are the coordination number, the nearest neighbor distance, the second nearest neighbor distance, and the density, respectively.....	21
IV	Probability distribution of three ring clusters.....	27
V	Results of g-C surface structure measurements.....	32
VI	Force constants of graphite in dyne/cm.....	48
VII	Number of C-atoms in the circle with radius R.....	53
VIII	Crossover radius R of three ring clusters.....	54
IX	Kr-graphite interaction energies determined by various methods.....	67
X	Interaction energy of a single Kr atom with a 2D triangular lattice of Kr atoms as a function of the nearest neighbor distance b.....	73
XI	Minimum and maximum binding energies and corrugations for three ring clusters.....	83
XII	The contribution of each three ring cluster to the total weighted average minimum and maximum interaction energies and corrugations.....	85
XIII	Coordinates of the central Kr atom at the physisorption sites corresponding to the minimum and maximum interaction energies.....	86
XIV	The weighted average binding energy of Kr on each DMM ensemble element and the weighted average binding energy of Kr on g-C.....	89
XV	(a) Ring angle of each convex ring cluster. (b) Ring depth of each concave ring cluster.....	93
XVI	(a) The relation between corrugation and ring angle for convex three ring clusters. (b) The relation between corrugation and ring depth for concave three ring clusters.....	95

Table

Page

XVII	Probability distribution of three ring clusters	121
XVIII	The probability of physisorption on a given ring of a three ring cluster.....	122
XIX	(a) Coordinates of the C-atoms of convex DMM three ring clusters, (b) Coordinates of the C-atoms of concave DMM three ring clusters, and (c) Coordinates of the C-atoms of flat DMM three ring clusters.....	131

LIST OF FIGURES

Figure	Page
1 Structural phases for rare gases adsorbed on graphite. (a) Commensurate, $(\sqrt{3} \times \sqrt{3})R30^\circ$ phase, (b) incommensurate, rotated phase, and (c) incommensurate nonrotated phase	4
2 (a) Simplified diagram of Kr on graphite, where "C-" and "I-" indicate commensurate and incommensurate, respectively. The coverage of commensurate monolayer is scaled to one. (b) Simplified diagram of Xe on graphite. The solid layers are incommensurate. The coverage of the most stable 2-dimensional triangular lattice is scaled to one.....	5
3 (a) Structure of graphite ¹² , (b) The basal plane of graphite	13
4 (a) 2D structure of graphite, (b) 2D CRN structure of g-C.....	18
5 (a) Local polyhedra represented by the nearest neighbors and bond angles (b) Definition of dihedral angle ϕ	19
6 Radial distribution functions of Beeman's models of g-C ²⁹ and Mildner's neutron diffraction measurements of a-C ³⁰	24
7 Possible combinations of 5-, 6-, and 7-membered rings in three ring clusters	25
8 (a) Zachariassen schematic of a quasi-2D CRN raft similar to that predicted in the C1120 structural model of g-C ¹² , and (b) the corresponding ring statistics histogram.....	26
9 2D honeycomb lattice with an embedded pentagon	29
10 Surface morphology of g-C thin films with optical microscopy. (a) ACF g-C on mica. Magnification, 40x. The central feature is a pin hole in the g-C film. (b) ACF g-C on glass. Magnification, 40x. Feature in up left is a crack in film.....	34
11 Schematic diagram of a scanning electron microscope	35
12 Surface morphology of g-C thin films. (a) ACF g-C on glass. $1.8 \times 10^4 \times$ magnification. The image size is $3.78 \times 3.06 \mu\text{m}^2$. (b) ACF g-C on mica. $1.8 \times 10^4 \times$ magnification. The image size is $3.78 \times 3.06 \mu\text{m}^2$	36
13 A schematic diagram of an optical interferometer	38
14 (a - b) 3D diagram of the surface morphology of g-C obtained by optical interferometry. (c) 2D profile of the surface morphology of g-C.....	39

Figure	Page
15	Surface morphology of g-C thin film with scanning tunneling microscope..... 41
16	A schematic diagram of the hierarchy of the structural model of g-C..... 44
17	A schematic diagram indicating the three angles defined by the intraplanar sp^2 bonds 49
18	The variation of the density $\rho(r)$ calculated with $J(r)$ of C1120 50
19	(a) An appropriate model of the near region of g-C with only a quasi-planar DMM region and a bulk RDM region. (b) Preferred division of g-C into a surface layer component and a bulk component..... 51
20	(a) Typical form of the Lennard-Jones 6-12 potential and (b) its derivatives ... 57
21	The effect of the substrate on the interactions between adatoms..... 59
22	The effective number of valence electrons per atom, n_{eff} , versus photon energy for several a-C's..... 62
23	Physisorption sites on a 567 three ring cluster 65
24	Coordinates of Kr-graphite interaction energy calculations 68
25	Graph of the interaction energy of a single Kr atom with a 2D triangular lattice of Kr atoms as a function of the nearest neighbor distance b 74
26	Mesh plots of the interaction energies of three ring clusters 75
27	(a) Definition of ring angle in a convex three ring cluster and (b) definition of ring depth in a concave three ring cluster 92
28	(a) The corrugation of Kr on g-C versus the convex ring cluster angle, and (b) the corrugation of Kr on g-C versus concave ring cluster depth..... 94
29	(a) The universal relation between corrugation per C-atom of Kr on g-C and the convex ring cluster angle, (b) the universal relation between corrugation of Kr on g-C and the convex ring cluster angle, (c) the universal relation between corrugation of Kr on g-C and concave ring cluster depth, and (d) the universal relation between corrugation per C-atom of Kr on g-C and concave ring cluster depth..... 96
30	Definition of physisorption height on a typical dented region of g-C..... 100
31	Coordinates of a 5-membered ring C-atom 126
32	Coordinates of a 6-membered ring C-atom 127

Figure	Page
33 Coordinates of a 7-membered ring C-atom	128

LIST OF DEFINITIONS

1. a-C amorphous carbon
2. ACF Arizona Carbon Foil Co., Inc.
3. C-atom carbon atom
4. central Kr atom the Kr atom for determining the positions of carbon atoms
5. CMM continuous medium model
6. CRN continuous random network
7. d-C diamond-like amorphous carbon
8. DMM discrete medium model
9. f_f out-of-plane bond-angle-bending force constant
10. f_q in-plane bond-angle-bending force constant
11. f_r bond-stretching force constant
12. g-C graphitic amorphous carbon
13. IRMRO intermediate-range medium range order
14. $J(r)$ radial distribution function
15. LRMRO long-range medium range order
16. LRO long-range order
17. MRO medium range order
18. RDF radial distribution function
19. RDM radial distribution model
20. rms root mean square
21. SEM scanning electron microscopy
22. SRMRO short-range medium range order
23. SRO short-range order
24. STM scanning tunneling microscopy

25. 2D

2-dimensional

CHAPTER 1

INTRODUCTION

In our daily lives, we are always surrounded by surfaces. These surfaces can be the surfaces of solid-state materials or those of liquid-state materials. Since most physical or chemical processes, which cause changes in our environments and even in ourselves, take place at these surfaces, it is hard to understate the importance of surfaces in our lives.

Adsorption, which is defined as the accumulation of particles at a surface,¹ is one of the most common processes at surfaces. Thus, we cannot truly understand the characteristics of interactions on surfaces without understanding adsorption on them. So it is natural that the study of adsorption has taken an important position in surface physics. We can divide adsorption into two types: physisorption and chemisorption. In chemisorption, a chemical bond (significant sharing or exchange of electrons) is formed between the adsorbed molecule and the substrate.² However, in physisorption, chemical bonds are not formed between the adsorbed molecule and the substrate.² Since the energies involved in physisorption are usually less than chemisorption energies and since the electronic wave functions of the adsorbate and the substrate are perturbed less in physisorption than in chemisorption,³ it is easier to investigate the static and dynamic aspects of the physisorption. Therefore, the study of physisorption has proven a good starting point toward the complete understanding of adsorption.

A. Adsorption of rare gases on graphite

Among the physisorption systems that have been investigated theoretically as well as experimentally, rare gas atoms adsorbed on the basal plane of graphite have been studied most actively. Because of the advantages discussed below, these systems have played a central role in studying basic aspects of physisorption. The energetics of these systems can be divided into adsorbate-adsorbate interactions and adsorbate-substrate

interactions⁴ and have been reviewed by Birgeneau,⁴ Gordon and Villain,⁵ and Steele,³ among others.

The interactions between rare gas atoms are simple and well known. First, the interactions are spherically symmetric. Thus, we do not have to consider the orientation of a rare gas atom. This makes conceptual and computational tasks easier. Second, the interactions are well represented with a Lennard-Jones 6-12 potential form.⁶ With appropriate coefficients, the interaction energies between rare gas atoms calculated with a Lennard-Jones 6-12 potential are quite consistent with experimental data.⁶ Although the Lennard-Jones 6-12 potential is a more complicated form than the inverse square law (Coulomb) potential, the Lennard-Jones 6-12 potential is still easy to handle in calculations and to interpret physically. Finally, it is a good approximation to treat the interactions between rare gas atoms pair wise.^{4,5} Thus it is possible to avoid intricate many body system calculations to figure out the interactions in a rare gas system. We only have to consider the interaction between two rare gas atoms at a time. The total interaction energy of rare gas system is given by the summation of each pair interaction energy.

The basal plane of graphite can be easily prepared as a relatively inert substrate with a very high, homogeneous (001) surface area with few defects:⁶ this provides good conditions for the adsorption of rare gas films. The interactions between rare gas atoms and carbon atoms (C-atom's) of graphite can also be described by a Lennard-Jones 6-12 potential as in the case of the interactions between two rare gas atoms.⁷ It has also been shown that the pair-wise approximation for interaction between a rare gas atom and a C-atom gives good agreement with experimental results (see Appendix 1).

Basic structures of solid rare gas adlayers on the basal graphite plane can be classified as commensurate and incommensurate phases. Fig. 1 shows examples of these structural phases for rare gases on the graphite basal plane.⁸ If there exist integers

N and M such that $N\bar{K} = M\bar{k}$ where \bar{K} and \bar{k} are the shortest reciprocal lattice vectors of the substrate and adlayer, respectively, then the adlayer is a commensurate adlayer. Layers that do not satisfy the above condition are incommensurate.²

The low temperature full-coverage Kr adlayer phase has a commensurate structure, $(\sqrt{3} \times \sqrt{3})R30^\circ$. Here $\sqrt{3}$ means that the lattice vectors of a Kr monolayer physisorbed on the basal graphite plane are $\sqrt{3}$ times longer than those of the primitive cell of graphite (001) and $R30^\circ$ means the unit cell of the Kr adlayer is rotated by 30° with respect to the primitive cell of graphite (001).⁴ A simplified phase diagram of Kr on graphite is shown in Fig. 2 (a).⁹ By contrast, the low temperature full-coverage phases of Ne, Ar, and Xe on graphite are incommensurate. The phase diagram of Xe on graphite is also shown in Fig. 2 (b).⁹

B. Adsorption on amorphous substrates

Unlike crystalline materials, amorphous materials do not have long-range translational order (periodicity). The lack of the long-range translational order of amorphous materials makes it difficult to set up universal models describing the structure and physical properties of amorphous materials. Because of this difficulty, studies of adsorption on amorphous substrates are only in a preliminary state.³ However, this difference also results in some distinctive features (e.g., resistance, magnetic properties, and thermal conductivity) for amorphous materials.

Recently, as new methods for controlling and exploiting these features of amorphous materials have been introduced, the technological and scientific importance of amorphous materials has greatly increased.¹⁰ Amorphous materials have many advantages for material applications. First, many amorphous materials are more easily prepared than their crystalline counterparts. In general, it can be very difficult to make perfect crystalline solids but is comparatively easier to make some amorphous solids.

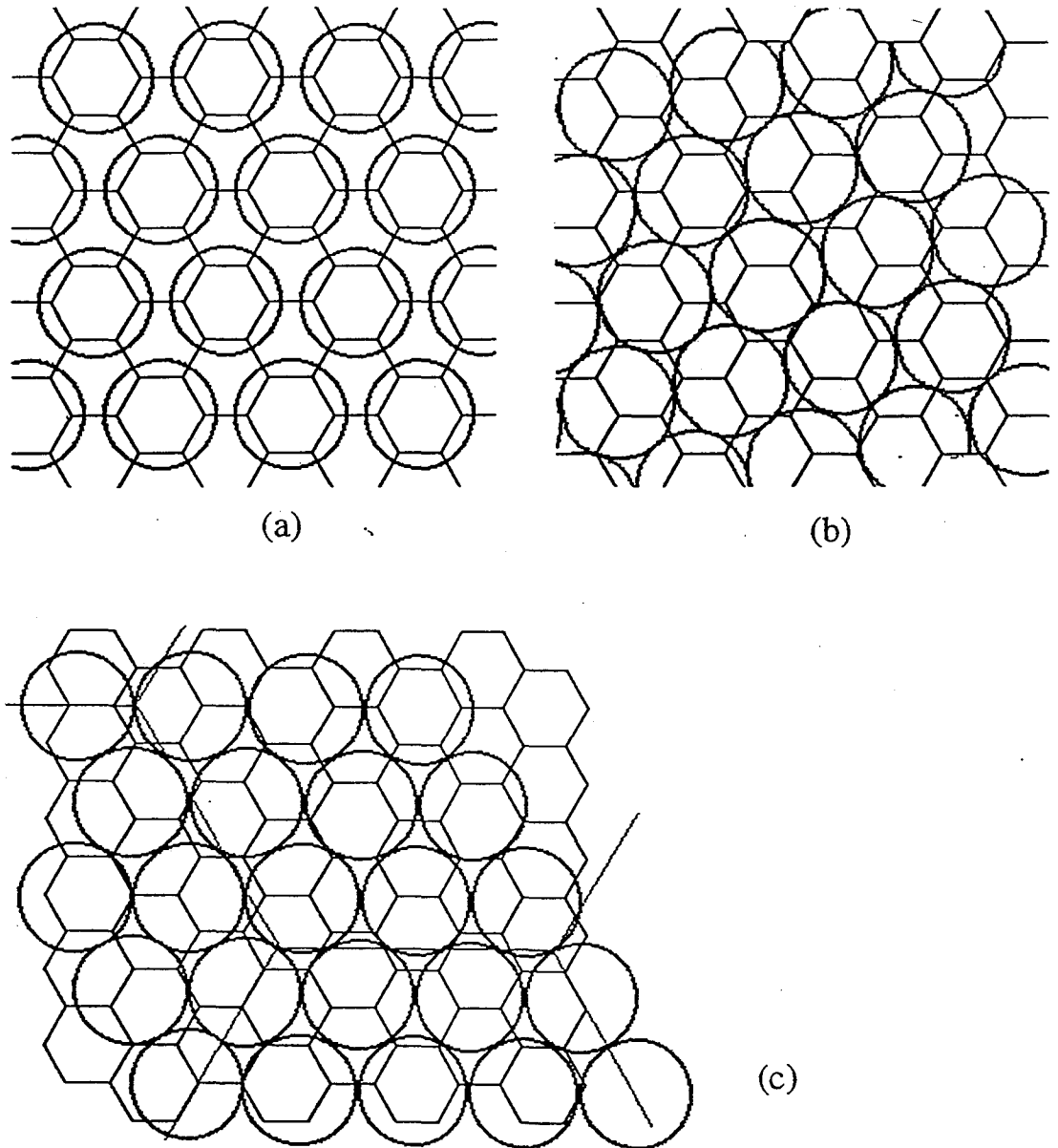


FIG.1. Structural phases for rare gases adsorbed on graphite. (a) Commensurate, $(\sqrt{3} \times \sqrt{3})R30^\circ$ phase, (b) incommensurate, rotated phase, and (c) incommensurate, nonrotated phase. After ref. 5.

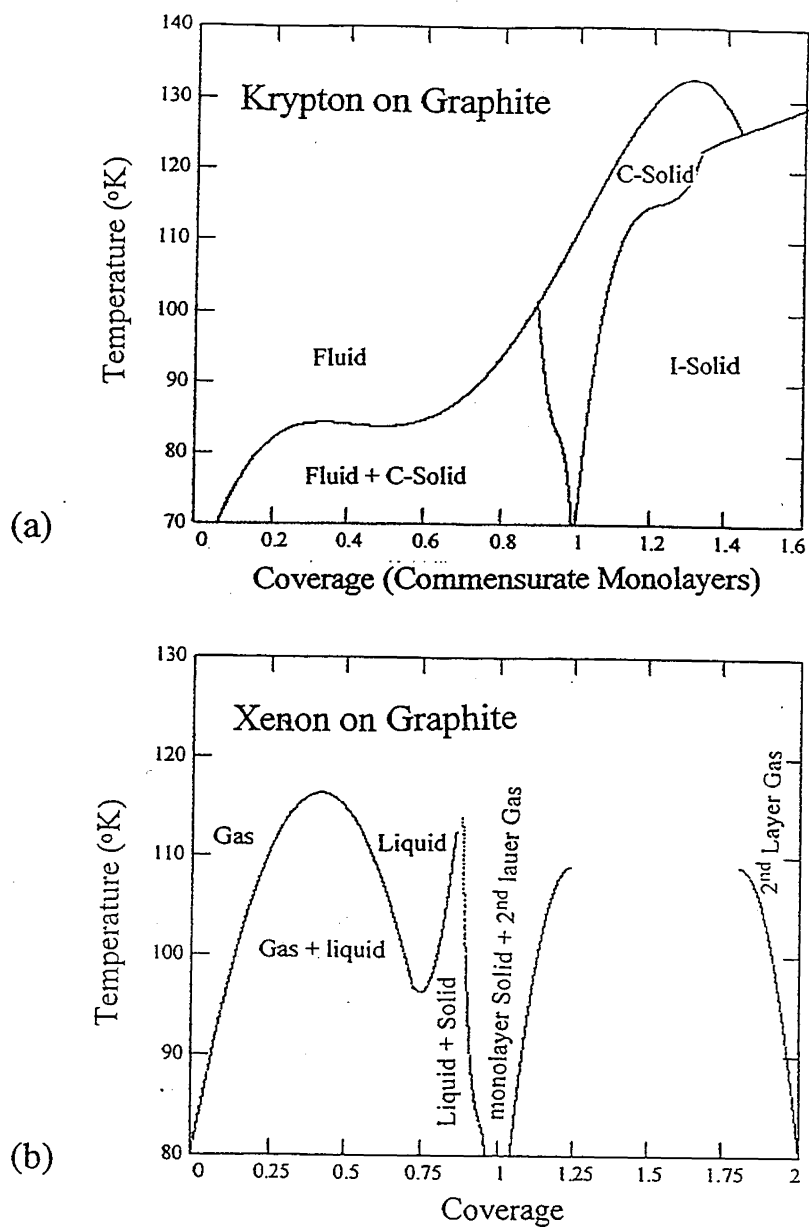


FIG. 2. (a) Simplified diagram of Kr on graphite, where "C-" and "I-" indicate commensurate and incommensurate, respectively. The coverage of commensurate monolayer is scaled to one. (b) Simplified diagram of Xe on graphite. The solid layers are incommensurate. The coverage of the most stable 2D triangular lattice is scaled to one. After ref. 9.

Furthermore, the viscosity of amorphous materials is relatively low over a range of temperatures near the glassy-transition temperature. As a result, amorphous materials can be more easily formed to various shapes. Second, amorphous materials are often homogeneous and isotropic on a macroscopic scale. By contrast, crystalline solids are generally anisotropic. As a consequence, physical properties of amorphous materials are often homogeneous and isotropic unlike crystalline solids. Third, amorphous materials can be formed homogeneously with various component materials over wide range of component proportions. In many cases this can be used to adjust their physical properties rather continuously.

Most of surfaces have a variety of surface defects. Since these defects have peculiar physical properties unlike perfect crystalline parts, the surface defects are used for a special purpose.² Heterogeneous catalysis is an example of this. The basic principle of heterogeneous catalysis is that chemical reactions occur at a certain type of adsorption sites much more preferentially. The surface defects or terrace edge sites of substrates are good candidates of the favorable adsorption sites.³ Such heterogeneous surfaces are closely related to amorphous substrates. To understand adsorptions on heterogeneous substrates, it is necessary to understand adsorptions on amorphous substrates as well as on perfect crystalline substrates.

For these reasons, amorphous materials are indispensable to modern industry. At the same time, adsorption on amorphous material surfaces has been raised as an important research field in surface physics.

C. Thesis objectives

The principal goal of this thesis research is to study the physisorption of Kr atoms on graphitic amorphous carbon (g-C). To demonstrate this, we will address the following three questions:

- (i) Will Kr adlayers form on g-C?
- (ii) What will their structures be?
- (iii) How will these differ from the structures of corresponding adlayers on graphite?

Kr physisorbed on g-C is an ideal starting point for the general investigation of adsorption on amorphous substrates. As mentioned above, Kr full-coverage adlayers physisorbed on the basal graphite plane at low temperatures have a commensurate structure unlike Ne, Ar, and Xe adlayers. For this reason, Kr has been chosen as the adsorbate for the preliminary study in this thesis. Graphitic amorphous carbon is an appropriate choice for an amorphous substrate, because g-C has many physical characteristics, (e.g., density, type of the bonds between C-atoms, and bond length) similar to those of graphite (see Table I). These similarities may make it possible for us to apply the abundant information about Kr adlayers physisorbed on the basal plane of graphite to our study of Kr adlayers adsorbed on g-C.

To study the aspects of Kr adsorbed on g-C, we have to know three things:⁴ (i) the lateral adsorbate-adsorbate interaction energy between two Kr atoms on g-C, (ii) the average binding energy of a Kr atom on g-C, and (iii) the corrugation of the g-C surface potential, which is defined as the difference between the maximum and minimum binding energies of one Kr atom physisorbed on g-C. The average binding energy of a Kr atom on g-C determines whether Kr adlayers will form on g-C. The lateral interaction energy between two Kr atoms and the corrugation of g-C surface binding energy are keys to predicting the structure of Kr adlayers on g-C. More specifically, the competition between the Kr - Kr interactions and the Kr - g-C interactions determines the structure of Kr adlayer physisorbed on g-C.⁴

To investigate these three physical properties, we first need a structural model for g-C. There are two requirements for a good g-C model. One is that the model has as many similarities in physical characteristics as possible with graphite; this facilitates

exploiting our knowledge about graphite. The other requirement is that it effectively models the structure and physical properties of g-C. To satisfy the latter, the model for g-C should be compared with the experimentally measured structure of g-C. A review of standard models of g-C and the specific model used in this work are given in Chapter 2. Chapter 2 also provides a description of our measurements of the surface structure of g-C and a review of related previous studies.

We also need specific forms for the adsorbate-adsorbate and adsorbate-substrate interaction potentials for the Kr on g-C adsorption system. Typically, these expressions are determined empirically. However, we do not as yet have experimental results to determine them, so it is necessary to perform theoretical modeling of the system. Chapter 3 describes the theoretical models of the interaction energies developed for this thesis. g-C has a lot of physical properties which are similar to those of graphite. Therefore, the interaction energy expressions for g-C will be based on corresponding expressions on graphite. However, our assumptions have to be carefully justified. Based on reasonable assumptions, the average binding energy of a Kr atom on g-C, the Kr - Kr interaction energy on g-C, and the corrugation of the g-C surface potential are calculated. Results of these calculations are also reported in Chapter 3.

Chapter 4 contains a discussion of the applications of these results. By using our calculation results, the structures of Kr adlayers adsorbed on g-C are predicted. We also compare the calculated structures of Kr adlayer adsorbed on g-C with those physisorbed on graphite. Then, the facts that determine the structural differences of Kr adlayers on the two substrates are discussed. We carefully assess the assumptions in the structural model for g-C and the interaction potential expressions for the Kr on g-C adsorption system, and then discuss the validity and applicable range for which the results of this thesis should be considered.

Chapter 5 provides a summary of conclusions drawn from this thesis and

discusses possible research directions for the study of adsorption on amorphous material substrates.

CHAPTER 2
STRUCTURE AND STRUCTURAL MODEL OF
GRAPHITIC AMORPHOUS CARBON

A. Necessity of a structural model of graphitic amorphous carbon

If an interaction potential is a central potential (a function only of the distance between two molecules), it is essential to know the relative position of one molecule with respect to the others in order to calculate the interaction energy between them. The Kr - Kr and Kr - C-atom interactions can be described by the Lennard-Jones 6-12 potentials,¹¹ and Lennard-Jones 6-12 potentials are such central potentials. Therefore, the first step in calculating the interaction energies for Kr and graphite or for Kr and g-C is to obtain sufficient information about positions of all carbon atoms relative to a certain adsorbed Kr atom. Let us call this Kr atom the "central Kr atom."

For a crystalline solid, the relative positions of all atoms in the solid are determined from the position of atoms in the primitive unit cell by translation. For infinite or semi-infinite crystals, if we have specific forms of potential energies for the interactions, we can calculate the interaction energies explicitly based solely on knowledge of the primitive unit cell. If the boundary except the surface considered here is far enough from the central Kr atom that the contribution of the boundary to the interaction energy is negligible, then we can assume that the system is infinite. This is the situation for our calculation of the interaction energies for system with rare gas adsorbates and crystalline substrates such as the Kr on graphite system. Boundaries, crystal truncations, or crystal defects relatively close to the central Kr atom make calculations much more difficult; such complications will not be considered here.

Amorphous materials do not have long-range translation order (periodicity). That is, the local structure of amorphous materials varies from place to place. Thus,

information about the local positions of some atoms in an amorphous material is insufficient to determine the exact locations of other atoms at a distance. This lack of periodicity prohibits applying standard methods used for crystalline materials to the amorphous materials themselves.

Then, if the interaction energies depend on the relative distance between atoms and if we do not know the exact position of every atom in an amorphous solid, is it possible to calculate the interaction energies in and on the amorphous solid? Precisely, the answer for this question is "No." However, it is the goal of this thesis work to produce an *approximate* answer to the question.

The approach taken here is a statistical approach, in a vein similar to ensemble theory used in statistical mechanics. Let us assume that we know the exact positions of all atoms in a hypothetical amorphous solid. Selecting one substrate atom to be at the origin, we could calculate exactly the interaction energy with a single central adsorbed atom near the origin if we have the exact expression for the interaction potential between atoms. However, this interaction energy depends on *which* substrate atom was selected to be at the origin. Selecting a different substrate atom (i.e., a different region for adsorption of the adatom) will lead to a different interaction energy because the spacing of substrate atoms from a different origin is not the same. We can view adsorption near each individual substrate surface atom as one member of an ensemble and then determine the ensemble average energies and fluctuations. Further, at relatively large distances from the origin, we can model the structure of the amorphous material in statistical sense, rather than requiring specific knowledge of the exact location of each substrate atom.

To take such a statistical approach requires a statistical model of the structure of the amorphous substrate. We begin by reviewing the structure of graphite and develop a statistical model of the structure of g-C appropriate for our adsorption calculations.

B. Structure and Physical Properties of Graphite

Bulk graphite has a simple hexagonal Bravais lattice with four C-atoms per primitive cell⁶ as shown in Fig. 3(a). The graphite lattice plane perpendicular to the c-axis of the primitive cell is called the basal plane of graphite. The structure of this basal plane is the 2D hexagonal lattice shown in Fig. 3(b).⁶ Lattice constants of graphite are $b=2.461(1)\text{\AA}$ and $c=6.7079(10)\text{\AA}$ at 15°C ¹² where b and c are indicated in Fig. 3(a) and Fig. 3(b), respectively.

Graphite consists of sp^2 bondings between C-atoms. This sp^2 bonding can be divided into two types: extremely strong intraplanar σ bonding and very weak interplanar π bonding.¹² The bond length of the σ bond is the intraplanar nearest neighbor distance of graphite, a , which is related to b by

$$b = \sqrt{2}a. \quad (2-B-1)$$

The bond length of π bond is exactly a half of the lattice constant c .

Other physical properties of graphite, including coordination number (defined as the number of the nearest neighbors,⁶ nearest neighbor separation, density, hardness, resistivity, and band gap, are presented in Table I.¹²

C. Structure and properties of graphitic amorphous carbon

1. Types of amorphous carbon (a-C)

a-C shows wide variations in physical properties from soot-like g-C to diamond-like a-C (d-C). The local structures of a-C's are the most important fact in deciding their physical properties, and usually their local structures are characterized by two parameters: the ratio of sp^2 and sp^3 bonds and the hydrogen content.¹⁶ sp^2 bonding leads to 3-fold coordination and graphitic-like carbon. By contrast, sp^3 leads to 4-fold coordination and diamond-like carbon.

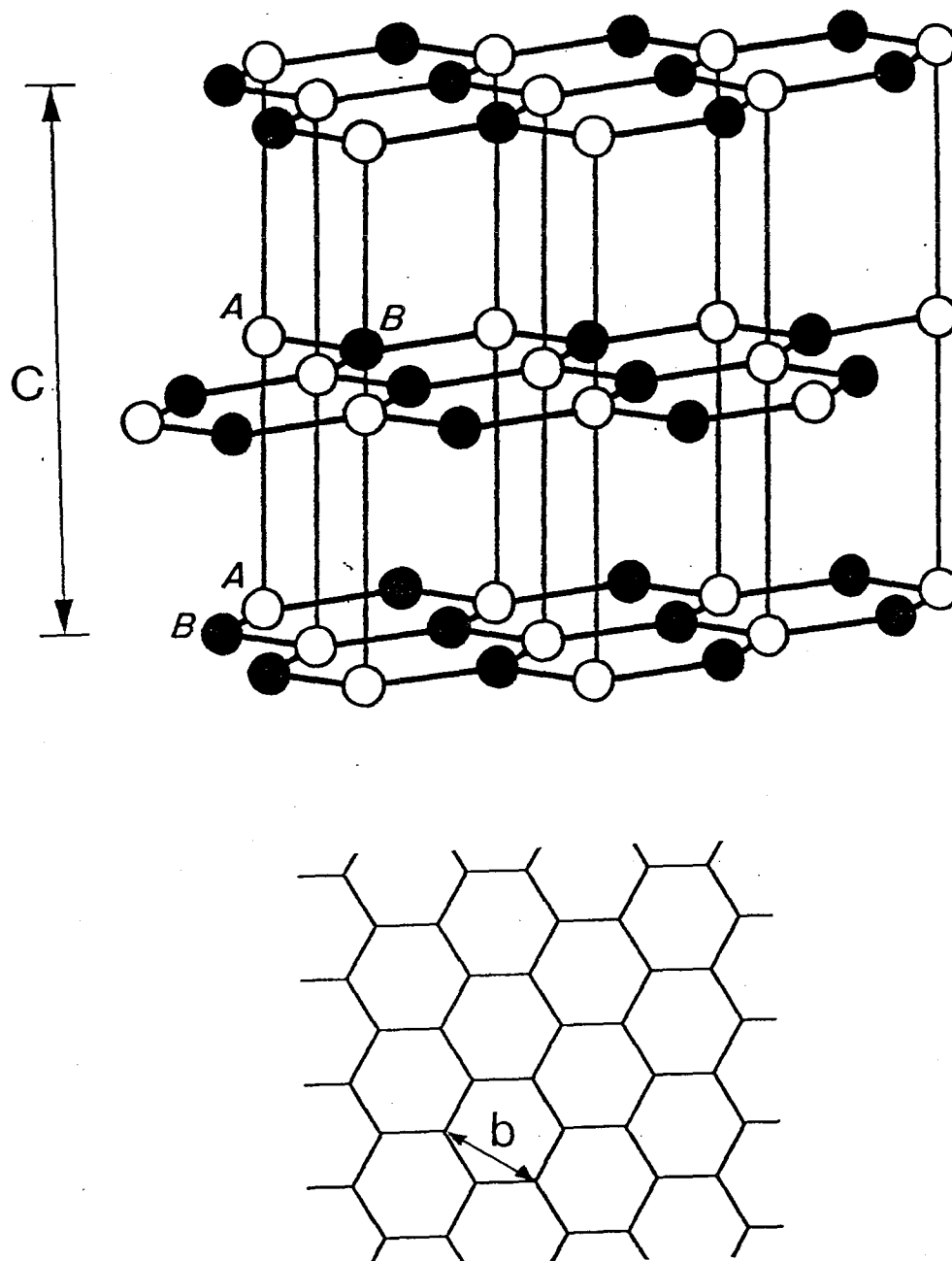


FIG. 3. (a) Structure of graphite,¹² (b) The basal plane of graphite.

TABLE I. Physical properties of graphite, typical g-C samples, and ACF g-C films.
After ref.12.

Property	Graphite	Typical g-C Samples	ACF g-C Films
Lattice Constant (Å)	a=2.4612(1) c=6.7079(10) @15°C	--	--
Coordination Number	3	3 or 4	--
Nearest Neighbor Separation (Å)	1.415 (intraplanar) 3.345 (interplanar)	--	--
Density (g/cm ³)	2.2670(4)	1.7 ~ 2.2	1.82±0.01 ¹³
Hardness (Mohs scale)	1 ~ 2	~ 6	~ 6
Resistivity (room temperature) (Ω-cm)	4×10 ⁻⁵ (interplanar) 5×10 ⁻² (intraplanar)	1 ~ 10	0.5 ¹⁴
Band Gap (eV)	0.0 ¹⁵	0.5 ~ 2.0 ¹⁶	--

Based on the ratio of sp^2 and sp^3 bonds, a-C can be classified into two broad categories: g-C and d-C. Formation methods, substrate condition, hydrogen content, and post-growth heat-treatment further subdivide g-C and d-C.¹⁶ g-C has approximately 90% to 100% sp^2 bonds. On the other hand, d-C's, which have high sp^3 bonding, are subdivided into ion-beam a-C and hydrogenated a-C (a-C:H). a-C:H contains 30% to 60% hydrogen, typically with >25% of the carbon sites having sp^2 bonds.¹⁶ Room-temperature conductivity, energy gap, density, hardness of glassy carbon (nanocrystalline graphite), evaporated a-C, ion-beam a-C, and a-C:H are presented in Table II.¹⁶ Based on the conductivity, we can see that glassy carbon and evaporated a-C are semi-metals. From the hardness of a-C:H, we can easily verify that a-C:H belongs to the d-C category.

The work described in this thesis deals exclusively with adsorption on *graphitic amorphous carbon*. The measured physical properties of the typical g-C class of materials shown in Table I include coordination number, density, hardness, resistivity, and energy gap. As pointed out, g-C consists of one type of atom (C-atom) and one dominant intraplanar sp^2 bond type. Due to these characteristics, g-C is generally treated as the prototype of a 2D continuous random network material.

2. Bulk properties of g-C

This thesis contains measurements of g-C surfaces with various direct surface structure probes to determine its surface morphology and comparison of the morphology with structural models for g-C in Section E. The thin-film g-C samples used for these measurements were made commercially by arc evaporation from high purity carbon rods onto $25 \times 76 \text{ mm}^2$ detergent-coated microscope slides or cleaved mica substrates at approximately room temperature using Dearnaley's method.¹⁷ The g-C films, which are between $0.05 \text{ }\mu\text{m}$ and $1 \text{ }\mu\text{m}$ thick, can be floated off their substrates and adhered to other surfaces. Physical properties of our samples have been determined

TABLE II. Room temperature conductivity (σ), energy gap, (E_g) density (ρ) and hardness of typical glassy carbon, evaporated a-C, ion-beam a-C, and a-C:H samples. After ref. 16.

	σ ($\Omega^{-1}\text{-cm}^{-1}$)	E_g (eV)	ρ ($\text{g}\text{-cm}^{-3}$)	Hardness ($\text{kg}\text{-mm}^{-2}$)
Glassy carbon	$10^2 \sim 10^3$	10^{-2}	1.3 ~ 1.5	800 ~ 1200
Evaporated a-C	$\sim 10^3$	0.4 ~ 0.7	~ 2.0	20 ~ 50
Ion beam a-C	$\sim 10^{-2}$	0.4 ~ 3.0	1.8 ~ 2.7	
a-C:H	$10^{-7} \sim 10^{-16}$	1.5 ~ 4	1.4 ~ 1.8	1250 ~ 6000

including density ($1.82 \pm 0.01 \text{ g/cm}^3$),¹⁷ hardness (about 6 in Mohs scale¹²), and resistivity ($0.5 \Omega\text{-cm}$);¹⁴ these are consistent with values for other g-C samples (see Table I). Furthermore, Dennison and Doyle¹⁸ measured the Raman spectra of these samples and have found good agreement with typical g-C spectra. Gao *et al.* confirmed that these samples are g-C using transmission electron microscopy (TEM)¹⁹ and electron energy loss spectroscopy (EELS)¹⁴ This large body of data clearly demonstrates that the samples used in this thesis are in the g-C category.

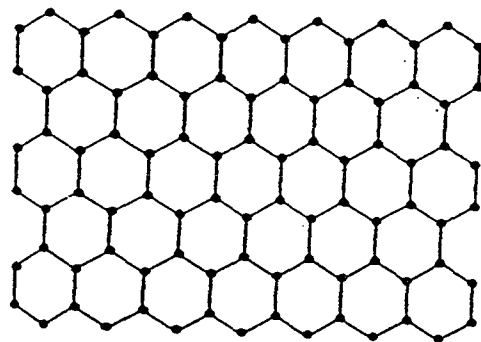
3. Continuous random network models

This section provides a brief review of continuous random network (CRN) structural models of amorphous solids. CRN's are disordered arrangements of atoms or molecules in which have bonds that are highly directional and usually covalent.²⁰ Zallen²¹ and Elliott²² discussed the structure of the CRN based on Zachariasen's pioneering work.²³ The simplest CRN structure is a 2D CRN with one type of atom and bond. g-C is the prototype of such a 2D CRN, since it is made up only of C-atoms

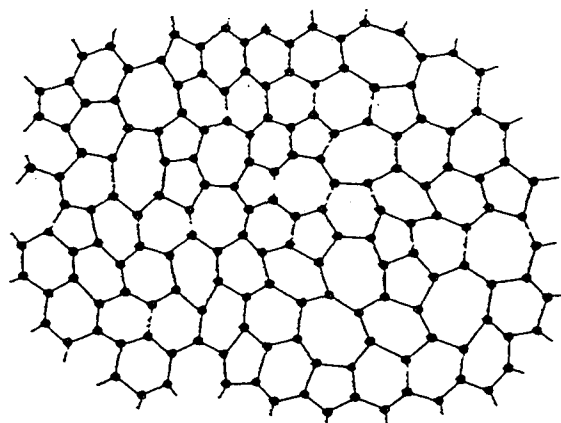
with one predominate type of bond (85% to 100% sp^2 bondings). The 2D CRN concept has also been successfully applied to binary composition glasses with directional covalent bondings, such as As_2Se_3 or As_2S_3 .^{20,23} Fig. 4 represents the 2D CRN structure of g-C and the 2D structure of the corresponding crystalline graphite counterpart.

The structural order in CRN's can be viewed in terms of short-range order (SRO), medium order (MRO), and long-range order (LRO). SRO is defined as structure between nearest neighbors over length scale up to about 3 Å. SRO is parameterized by the coordination number, nearest-bond length, and bond angle. Thus, SRO describes well-defined local polyhedra like these shown in Fig. 5(a).

MRO includes the structure of next-nearest neighbors to several-nearest neighbors. MRO can be further subdivided into short-range MRO (SRMRO), intermediate-range MRO (IRMRO), and long-range MRO (LRMRO).²⁰ SRMRO refers to next-nearest neighbor structure with length scales of 3 Å to 5 Å. Over these length scales, SRMRO describes the type of connections within local polyhedra and their relative orientations. The relative orientations are well characterized by the dihedral angle, which is defined as the angle between two projections of bonds that belong to different local polyhedra on the plane perpendicular to the connection of the two local polyhedra [see Fig. 5(b)]. IRMRO (5 Å to 15 Å) is characterized in terms of n-membered rings or clusters of atoms of a certain shapes or sizes. Rings or three-ring clusters, which will be discussed in Section E, are examples of this range structure. On a length scale greater than 10 Å to 20 Å, LRMRO describes the local dimensionality of the covalently bonded network. CRN's do not have the long-range order (periodicity), in contrast to crystalline materials.

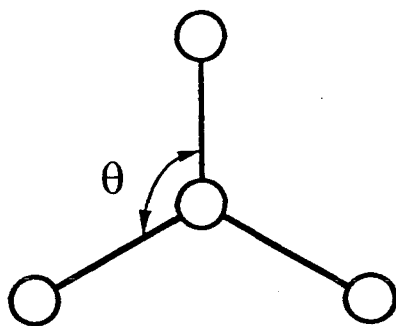


(a)

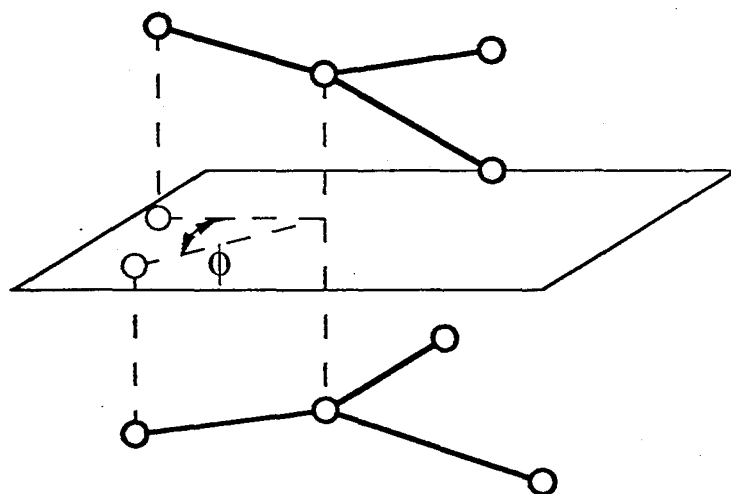


(b)

FIG. 4 . (a) 2D structure of graphite, (b) 2D CRN structure of g-C. After ref.12.



(a)



(b)

FIG. 5. (a) Local polyhedra represented by the nearest neighbors and bond angles (b) Definition of dihedral angle ϕ . After ref. 20.

4. Structural models of a-C

Robertson¹⁶ identified three types of structural models for disordered and amorphous carbon; (i) glassy carbon models composed of structural layers comprised of microcrystals of graphite stacked in disordered structures,²⁴ (ii) models of a random networks consisting of nanometer diameter regions of sp^2 bonding linked by sp^3 bonds,²⁵⁻²⁸ and (iii) models of random networks with mixed sp^2 and sp^3 bonding characterized by the ratio of sp^2 and sp^3 sites.²⁹ Among these three structural models, the third case, typified by a modeling study by Beeman *et al.*,²⁹ is most appropriate to the g-C material of the present study. Thus, let us look into Beeman's models more specifically.

We begin by considering the parameters describing the SRO (coordination number, bond length, and bond angle) of g-C to determine which of Beeman's models is most applicable. Beeman *et al.* constructed four structural models for a-C containing different ratios of sp^2 and sp^3 bonds (refer to Table III). The model "C1120" was made up exclusively of sp^2 bonds. "C340" had 9.1% sp^3 -site C-atoms and "C356" contained roughly 50% sp^3 bonding C-atoms. "C519" model was composed of only sp^3 bondings. Since g-C is a mixture of sp^2 and sp^3 bondings dominated by sp^2 bonds (greater than 85%¹⁶), the coordination of g-C should be close to 3.¹² From the ratio of sp^2 to sp^3 sites alone, it can be seen that C1120 and C340 are the best candidates for structural models of g-C.

For all Beeman's models, bond lengths between three coordinated atoms were relaxed to approximately 1.42 Å (the intraplanar bond length in graphite), bond lengths between four coordinated atoms were relaxed to 1.56 Å (the diamond bond length), and those between three coordinated atoms and four coordinated atoms were adjusted to 1.51 Å (the bond length of toluene). The minimal distribution in bond lengths results from the fact that typically the bond-stretching force constants (f_r) are a factor of five

TABLE III. Physical properties of graphite, diamond and a-C's. n_1 , r_1 , r_2 , and ρ are the coordination number, the nearest neighbor distance, the second nearest neighbor distance, and the density, respectively. After ref. 16.

Sample	n_1	r_1 (Å)	r_2 (Å)	ρ (g/cm ³)
Graphite	3	1.42	2.45	2.25
Diamond	4	1.55	2.52	3.51
a-C:				
Mildner ³⁰	2.99	1.425	2.45	1.49
Kakinoki ³¹	3.45	1.5	2.53	2.4
Boiko ³²	3.30	1.43	2.53	2.1
Models: ²⁹				
C1120	3.00	1.42	2.44	2.11
C340	3.28	1.42	2.43	2.69
C356	3.53	1.51	2.55	3.21
C519	4.00	1.55	2.52	3.39

greater than the in plane bond-angle bending force constants (f_{θ}) for CRN materials.²⁰ Thus, the bond lengths of sp^2 and sp^3 bonds of g-C change minimally from those of sp^2 bonds in graphite and those sp^3 bonds in diamond, while the bond angles have a much wider distribution. The bond length variation is reflected in the radial distribution function (RDF), $J(r)$, which is defined as the number of atoms lying at radial distances between r and $r+(\text{unit radial distance})$ from a selected atom located at the origin. The calculated RDF's for each Beeman's four models are shown in Fig. 6 where they are compared with an experimental RDF of g-C measured by Mildner and Carpenter³⁰ using neutron diffraction. As can be seen in Fig. 6, the RDF of C1120 shows the best agreement with Mildner's RDF of g-C. The related physical properties of Mildner's g-C sample are quite similar to those of g-C listed in Table I. We also note that the density of the C1120 model is most similar to the density of graphite and g-C as listed in Table III.

We therefore conclude that Beeman's C1120 model is the best structural model for the class of g-C material studied in this thesis. Beeman also reached the conclusion that his C1120 model best describes g-C based on comparison with ir, Raman, electron diffraction, x-ray diffraction, neutron diffraction, NMR, and EXAF data.²⁹ For the C1120 model, Beeman estimates the bond length of g-C is $a=1.42\pm 0.01$ Å and the bond angle is $\theta=117\pm 6^\circ$, with ring statistics of 21% 5-membered rings, 59% 6-membered rings, and 20% 7-membered rings and a density of $\rho_o=2.11$ g/cm³.

The SRMRO of g-C is represented by the ring structure. The wide variation of the bond angles in g-C allows the existence of significant number of 5- and 6-, and 7-membered rings and even perhaps some 4-, 8-, and 9-membered rings.²⁵ The CRN's of C1120, C340, C356, and C519 are comprised of 5-, 6-, and 7-membered rings. Beeman estimated the number of 5-, 6-, and 7-membered rings per C-atom for C1120, C340, C356, and C516 from which we determined the ring statistics (see Appendix 2).

The ring statistics (the probability distribution of 5-, 6-, and 7-membered rings) of the C1120 CRN are given in Table XVI (Appendix 2).

As discussed above, the IRMRO for g-C (on a length of 5 Å to 15 Å) can best be characterized in terms of collections of rings. Fig. 7 shows the possible three ring clusters composed of 5-, 6-, and 7-membered rings. The probability of encountering each of the three ring clusters in Fig. 7 are calculated in Appendix 2, based on the ring statistics for the C1120 model, and are listed in Table IV.

Beeman's C1120 model predicts an IRMRO structure of sp^2 -bonded C-atoms which form rafts of quasi-2D CRN rings on the order of 10 Å to 20 Å in diameter. Fig. 8¹² shows a Zachariassen schematic of one such quasi-2D CRN raft similar to that in the C1120 model. The constituent atoms in this figure are all 3-coordinated, with nearly uniform bond lengths and a broad bond-angle distribution centered near 120°. The structure in Fig. 8 is comprised of 5-, 6-, and 7-membered rings. The ring statistics [indicated in Fig. 8(b)] and the three ring cluster probability distribution (see Table IV) are quite similar to those of the C1120 model. The two circles in Fig. 8 indicate 20 Å and 30 Å diameter circular rafts, respectively.

The presence of 5-, 7-, 8-, and 9-membered rings in the quasi-2D CRN of g-C suggests warping or bending within a raft on the LRMRO length scale.²⁰ This is discussed in more detail in Section D.1 below. Galli *et al.*²⁵ estimated that this local warping is less than 1Å within a particular raft. Isotropic structure, lacking LRO, is achieved by random orientation of the raft planes. The necessity of dangling bonds resulting from the unconnected, randomly oriented rafts can be avoided by connection with a few sp^3 C-atoms as suggested by Robertson.¹⁶ However, the extent of layering, the specific correlation of adjacent rafts, and the presence and distribution of sp^3 bonded C-atoms are not well understood.

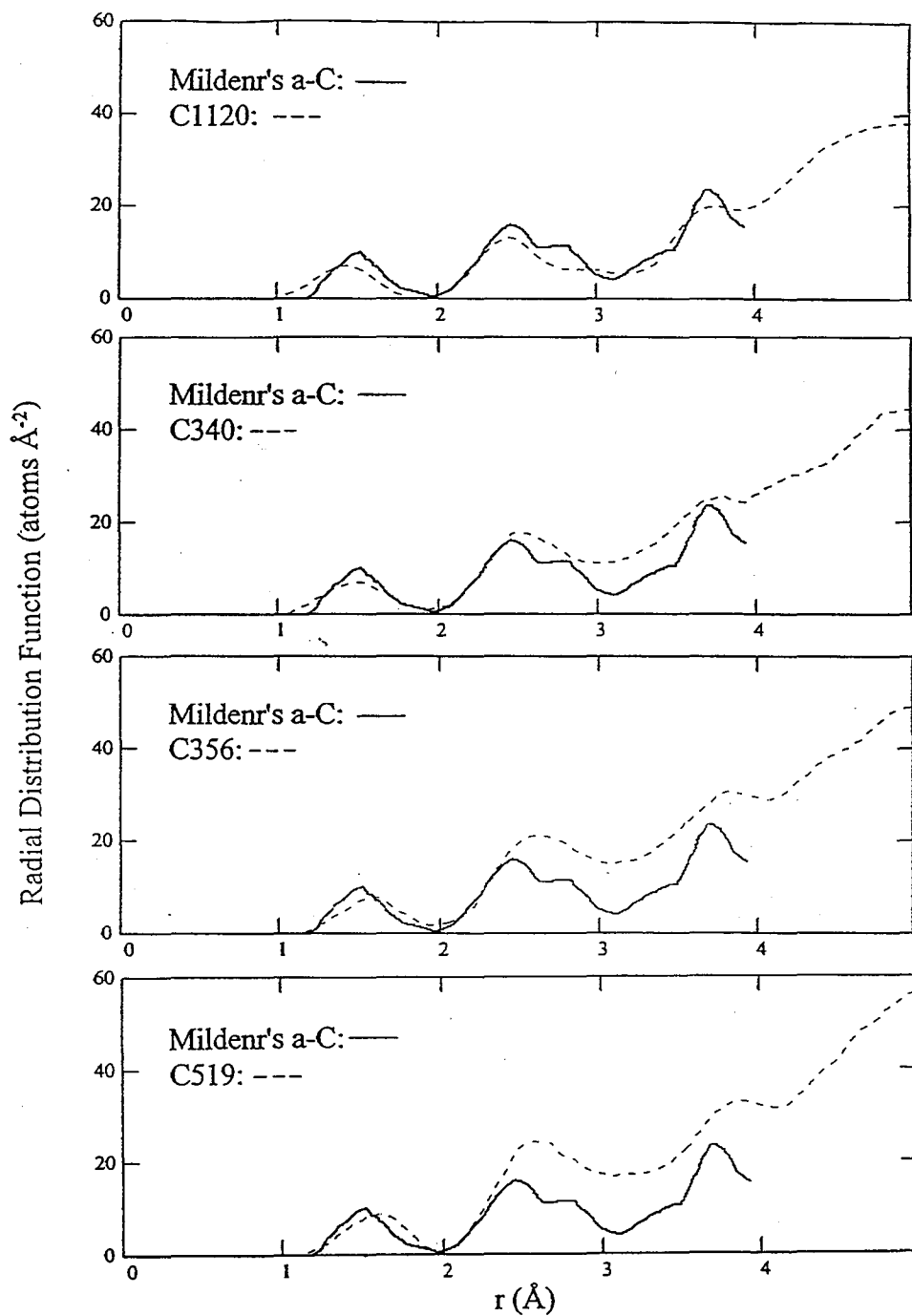


FIG. 6. Radial distribution functions of Beeman's models of g-C²⁹ and Mildner's neutron diffraction measurements of a-C.³⁰

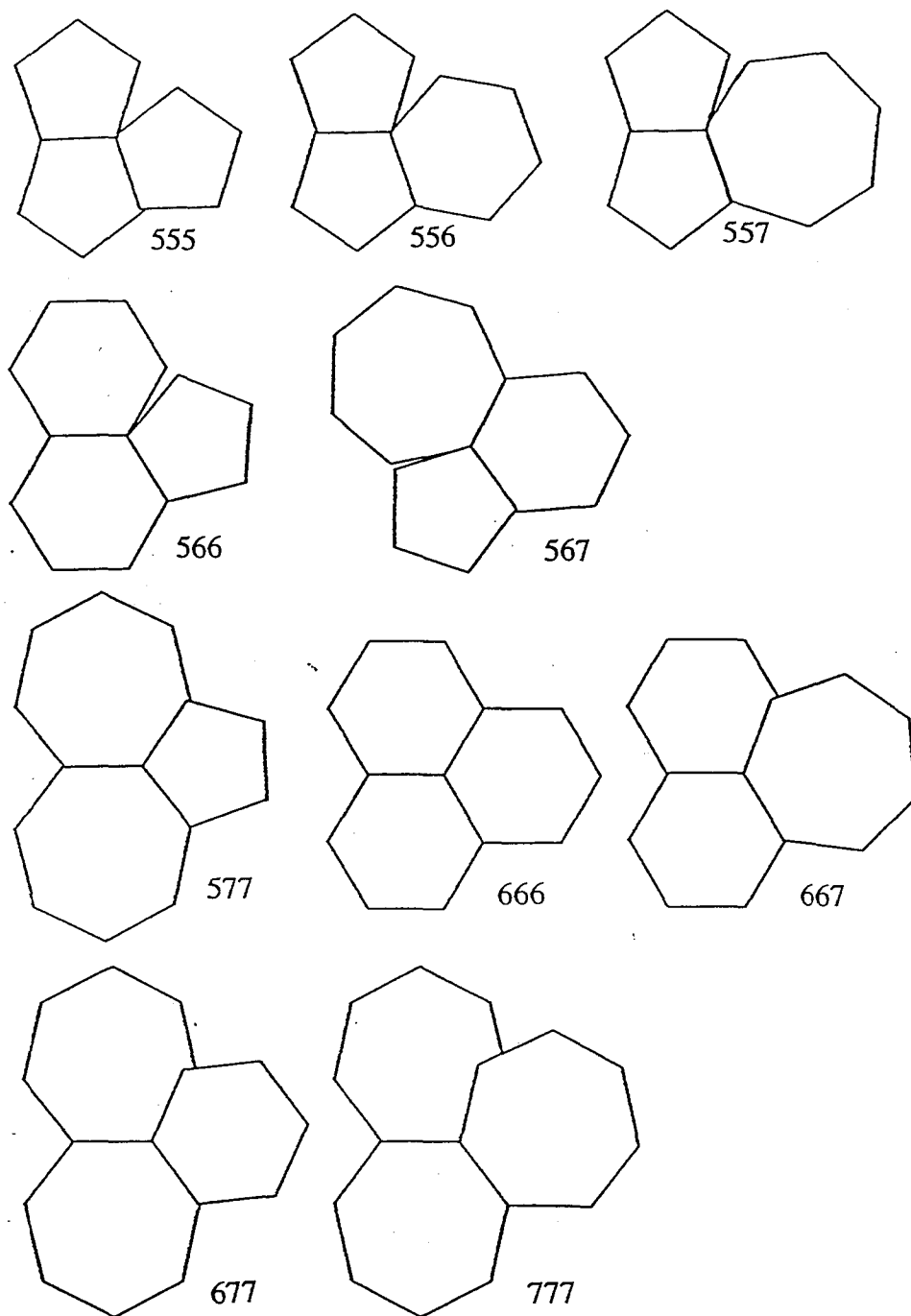


FIG. 7. Possible combinations of 5-, 6-, and 7-membered rings in three ring clusters.

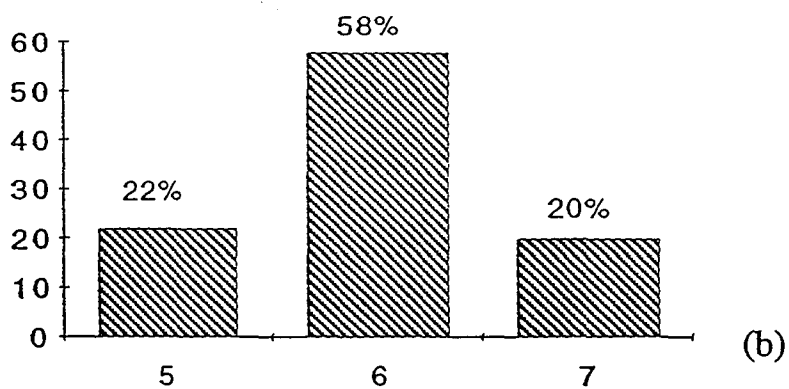
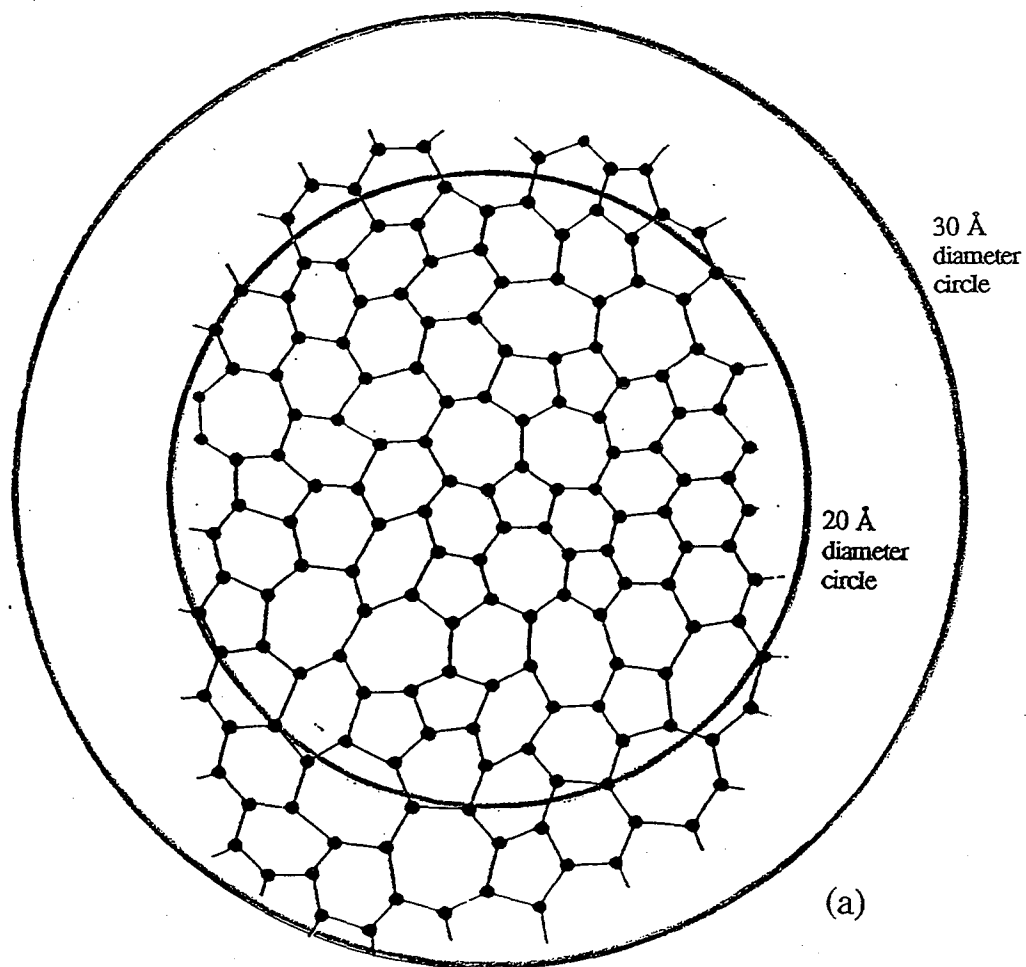


FIG. 8. (a) Zachariassen schematic of a quasi-2D CRN raft similar to that predicted in the C1120 structural model of γ -C,¹² and (b) the corresponding ring statistics histogram.

TABLE IV. Probability distribution of three ring clusters. Refer to Appendix 2 for details.

Three ring cluster	Calculated three ring cluster probability distribution based on Beeman C1120 ring statistics (%)	Empirical three ring cluster probability distribution for structure in Fig. 7 (%)
555	1.1	0
556	8.5	1
557	2.7	3
566	23.2	16
567	14.7	24
577	2.3	4
666	19.9	24
667	21.0	22
677	6.3	6
777	0.7	0

D. The surface structure of graphitic amorphous carbon

1. Geometrical properties of the surface of g-C

The presence of rings other than 6-membered rings has a major impact on the structure of g-C, particularly its surface structure. In a 2D honeycomb lattice, the presence of 5-, and 7-membered rings cause change of local curvatures around them.²⁰ Addition of 5-membered rings (or other sized rings with less than six members) produces “spherical curvature” (or positive curvature), which is the curvature of convex or concave surfaces. Addition of 7-membered rings (or other sized rings with more than six members) causes “hyperbolic curvature” (or negative curvature), which is the curvature of a saddle surface.³³

As an example of the introduction of positive curvature, consider a pentagon embedded in a honeycomb lattice. The modified lattice can not remain in a plane even when both bond angle and bond length variations in the hexagons are permitted. Begin by considering the regular pentagon in Fig. 9; setting the origin at the center of the pentagon, the lattice has five-fold symmetry. If we attach hexagons sequentially to this pentagon, the sides of hexagons are located alternatively on the A and B lines and they are connected by the other sides of hexagons, 1, 2, *and so on*, as in Fig. 9. As the distance from the origin increases, the distance between lines A and B also increases linearly. As a result, at large enough distances, we cannot connect the hexagon sides on lines A and B with the remaining side of a hexagon. This means that we cannot make the modified honeycomb lattice be 2D. The only way to make the distance between the lines A and B be finite and have the modified lattice maintain five-fold symmetry is to change its structure from a planar structure to a spherically curved surface (convex or concave structure). Similarly, it has been shown that the honeycomb lattice, with an embedded heptagon, should have a saddle-like structure with negative curvature.³⁴⁻³⁷

As a result, it is generally impossible to make a honeycomb lattice, which has 5-

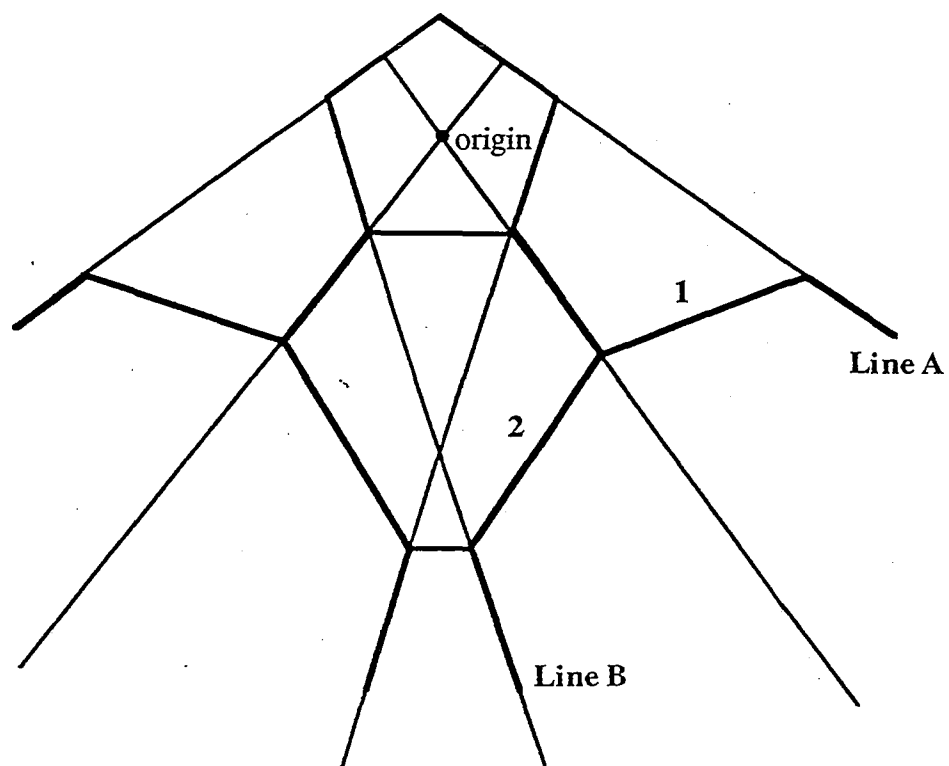


FIG. 9. 2D honeycomb lattice with an embedded pentagon.

or 7-membered rings, be perfect flat. This is the fundamental reason that the rafts of g-C have warping or bending.

2. Previous theoretical and experimental results

Galli *et al.*²⁵ investigated the structural and electrical properties of amorphous carbon theoretically. They modeled the structure of a-C using computer simulations based on first-principles tight-binding molecular dynamics. Their sample had 85% sp² site C-atoms and 15% sp³ C-atoms. The authors showed that the physical properties of their a-C model agree with various experimental and theoretical properties of g-C. The resultant structure of their a-C model was composed of several thick planes, which were connected by a few orthogonal planes. These thick planes were quasi-2D CRN's and their root mean square (rms) roughness was about 1Å. More recent models of tight-binding molecular dynamics calculations²⁷⁻²⁸ predict similar structures.

Marchon *et al.*³⁸ investigated the surface morphology of g-C thin films prepared by dc magnetron sputtering onto ~100°C substrates with STM (scanning tunneling microscopy) using the "constant height" mode. They obtained atomic resolution images of the g-C films and observed the existence of small (~15 Å) graphitic domains with localized π bonding. The regions exhibited predominately 6-membered rings, but 5-membered rings and other nonperiodic structures were also seen. Their results also show that g-C films have graphitic short-range order with rms roughness much less than 1 Å over 1×1 nm² lateral dimensions. Additional STM studies of a-C have observed similar features, but their results are less conclusive.³⁹⁻⁴⁰ Weissmantel *et al.*⁴¹ have also suggested the presence of 5-, 6-, and 7-membered rings on sputtered a-C films based on their electron diffraction measurements. These results are consistent with the structural models of Beeman, Galli, and others discussed above.

3. Measurement of the Topography of Graphitic Amorphous Carbon

The Kr - g-C and the Kr - Kr on g-C interactions are functions of the positions of C-atoms in g-C. Thus, the surface topography of g-C is an important factor in determining the structure of Kr adlayers on g-C. Therefore, we have studied the topography of g-C samples through surface probe measurements directly, so as to compare the structure of a specific, real g-C material with our structural model and to deduce how reliable are our model of g-C and the interaction energies calculated with this model.

To investigate the topography of g-C, the height variations of g-C surfaces were measured with several complimentary experimental methods, which explored several lateral dimensions determined by the characteristics of experimental probes. The measurement techniques used were (i) optical microscopy, (ii) SEM (scanning electron microscopy), (iii) optical interferometry, and (iv) STM. Our experimental results are summarized in Table V.

Let us look into the possible information about the topography of g-C obtainable with these structural probes. First, the optical microscopy will provide information about the sub-millimeter surface structure of g-C. Since one millimeter is a huge length on the atomic scale, we expected that optical microscopy can only observe the gross defects existing on g-C surfaces. If some wrinkling of g-C surface is observed, then this wrinkling will not be due to the nanoscale structure of g-C itself, but rather due to some other factors, *e.g.*, the internal stresses of the g-C films or substrate irregularities. SEM and the optical interferometry have submicron resolution. These techniques have the potential to give us (i) gross surface features of g-C which include rafts, raft edges, and defects, and (ii) rms roughness. In amorphous materials, it is hard to define defects clearly, but it may be possible to observe something like holes due to defects of sp^2 and sp^3 bonds of g-C. STM can have subnanometer resolution power. Therefore,

TABLE V. Results of g-C surface structure measurements.

Experimental Method	Optical Microscopy	SEM	Optical Interferometry		STM	
Image Size	--	3.78 x 3.06 μm^2	245 x 239 μm^2	140 x 185 μm^2	500 x 500 nm^2	9 x 9 nm^2
Magnification	40.0 x	1.8x10 ⁴ x	206.6 x	555.6 x	1.6x10 ⁵ x	8.0x10 ⁶ x
Vertical Resolution Limit	--	7 nm to 8 nm	0.1 nm	0.1 nm	≤ 0.1 nm	≤ 0.1 nm
Horizontal Resolution Limit	--	4 nm to 6 nm	50 nm	50 nm	≤ 0.2 nm	≤ 0.2 nm
Measured rms Roughness	< 1 μm	< 0.1 μm	< 1 nm	< 0.6 nm	< 0.5 nm	0.08 nm
Conclusions	Sample is smooth to within vertical resolution over ~ 1mm lateral length scale.	Macroscopic wrinkling of the g-C was observed.	Significant height variation was measured at this lateral dimension.	rms roughness is reduced as the lateral dimension is reduced.	The surface roughness of g-C was clearly observed.	< 1 Å rms surface roughness of the g-C was measured at these lateral dimensions.

we can hope to observe (i) roughness of g-C surface within rafts, (ii) raft size, and (iii) atomic structures of rings as were observed by Marchon *et al.*³⁸

The g-C thin films used for the surface measurements were made by Arizona Carbon Foil Co., Inc. (ACF). An arc-evaporation method was used for making these films.¹³ These films were deposited at room temperature on 25×76 mm² detergent-coated glass and mica microscope slides. Their physical properties are listed in Table I.

a. Optical microscopy: The g-C films were observed through an optical microscope with $40 \times$ maximum magnification. The results of this experiment show that the surfaces of the carbon films too smooth to observe wrinkling at this magnification. Fig. 10 shows the results.

b. SEM: The g-C films were mounted on flat aluminum disks for SEM studies, following the instruction of ACF⁴² and were then dried in air.

A Hitachi S4000 Field Emission SEM equipped with light element capability was used at the USU Electron Microscopy Center. Let us consider the basic operating principles of SEM. A schematic diagram of an SEM is shown in Fig. 10. The secondary electrons emitted from the sample are collected in a detector. The detector signal is synchronized with the electron beam scan and the cathode ray tube scan to produce an SEM image.⁴³ Typically, an SEM has a 7-nm to 8-nm vertical resolution limit⁴⁴ and a 4 nm to 6 nm horizontal resolution limit.⁴³

Our experiments studied the submicron aspects of the g-C surfaces. Under low magnification, macroscopic wrinkling of the g-C surface was observed. As the resolution of SEM was increased, only smooth g-C surfaces were observed. These observations provide the justification for the approximations in the calculations of Kr-g-C interactions which assume the g-C surfaces are flat at large distances from an adsorbed atom (the RDM and CMM regions treated in detail in Section E). Fig. 12 shows the experimental results.

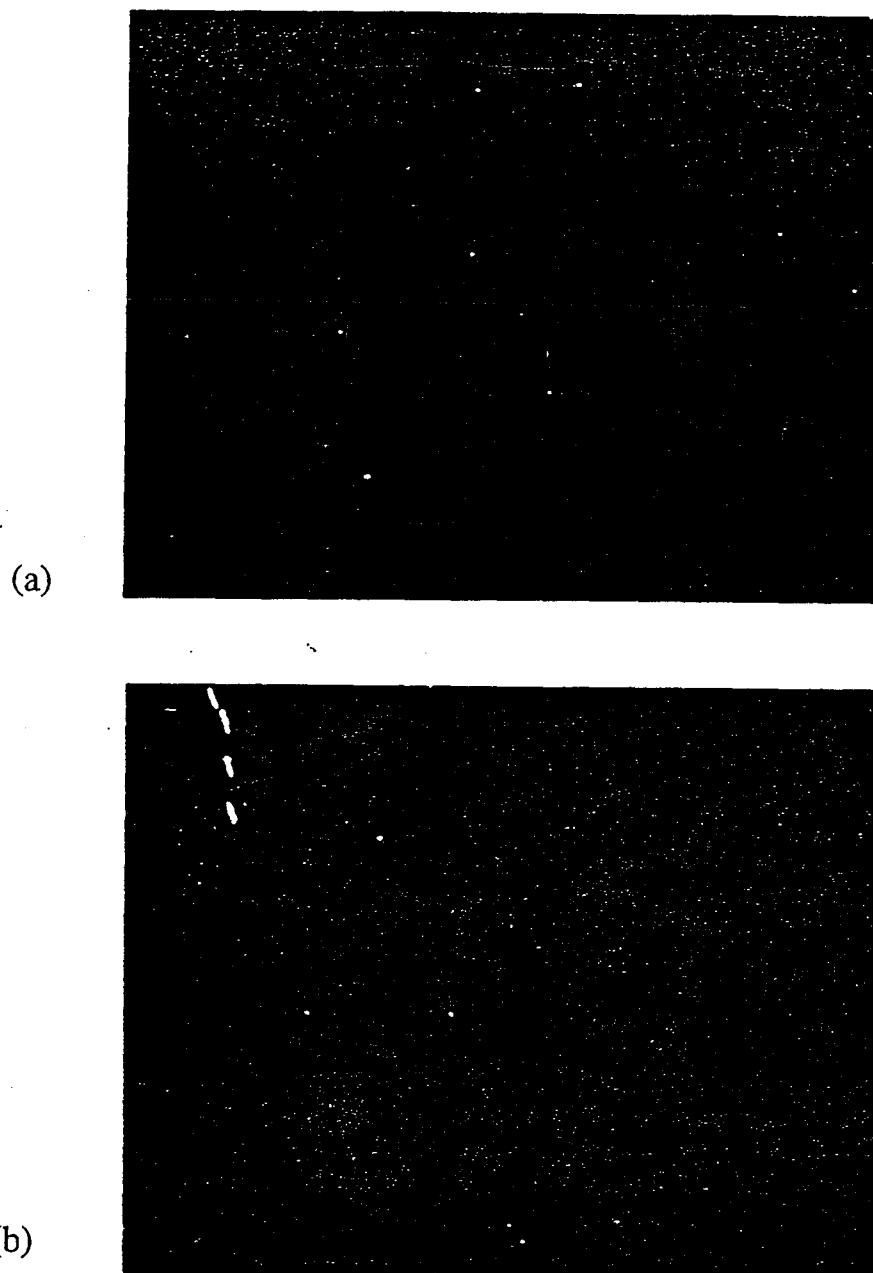


FIG. 10. Surface morphology of g-C thin films with optical microscopy. (a) ACF g-C on mica. Magnification, 40x. The central feature is a pin hole in the g-C film. (b) ACF g-C on glass. Magnification, 40x. Feature in up left is a crack in film.

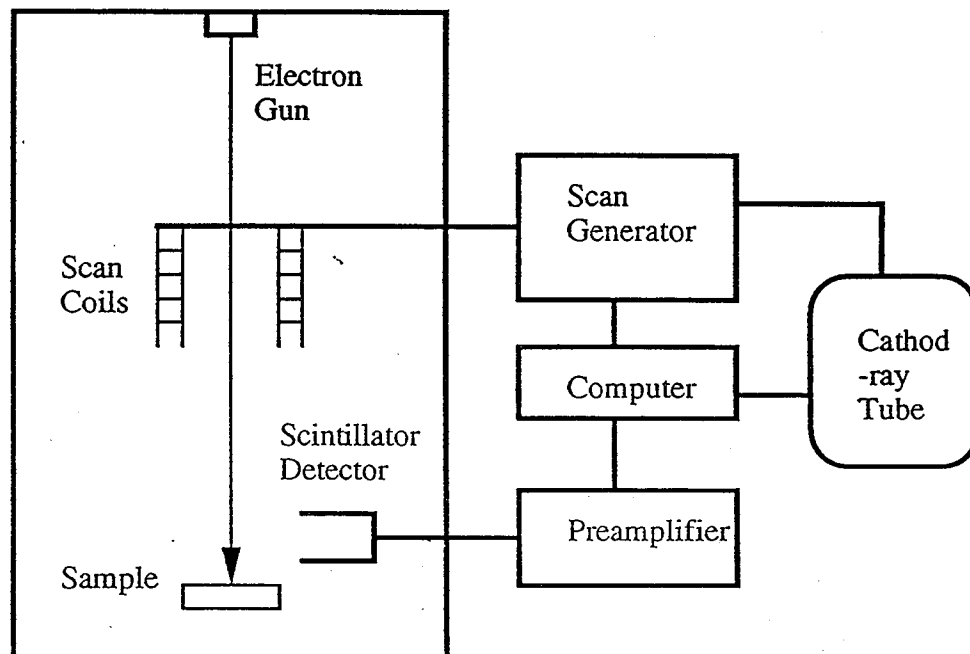
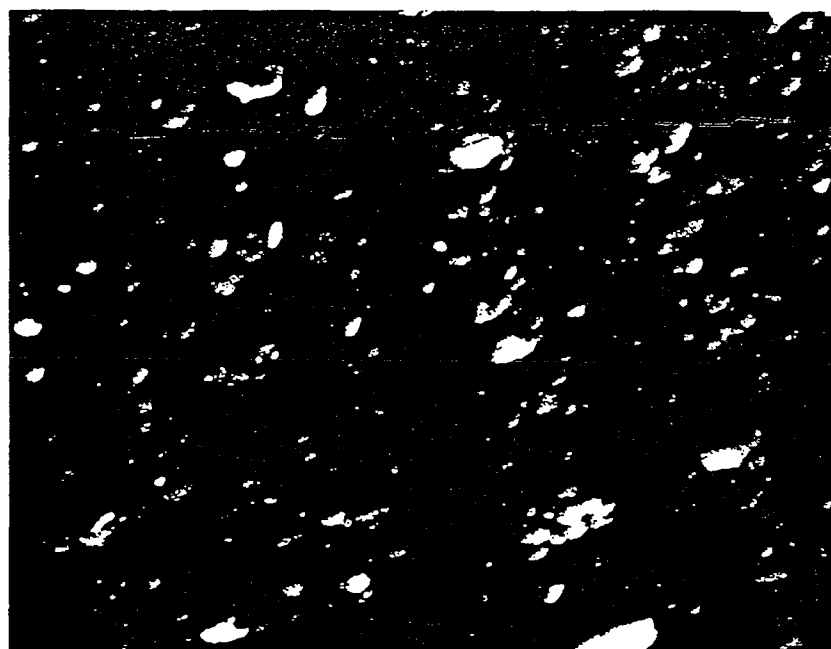


FIG. 11. Schematic diagram of a scanning electron microscope. After ref. 44.



(a)



(b)

FIG.12. Surface morphology of g-C thin films. (a) ACF g-C on glass. 1.8×10^4 x magnification. The image size is $3.78 \times 3.06 \mu\text{m}^2$. (b) ACF g-C on mica. 1.8×10^4 x magnification. The image size is $3.78 \times 3.06 \mu\text{m}^2$.

c. Optical interferometry: The optical interferometer instrument used is an interferometer that has an internal reference surface.⁴⁵⁻⁴⁶ The reflected light from the sample interferes with the reflected light from the internal reference surface. The resultant interference pattern can be observed through the eyepieces of a microscope. This pattern is also recorded and analyzed by a computer. Fig. 13 shows a schematic diagram of an optical interferometer.³⁰ Measurements were made using a Wyco optical interferometer by Chao Gao at Hitachi Corp. The “ultra-low noise 2D configuration” was chosen as the experimental method. In this configuration, the vertical and horizontal resolution limits of this instrument are 0.1 nm and 50 nm, respectively.⁴⁷

Using this optical interferometry, the gross features of the g-C surface and its rms roughness have been studied. Fig. 14(a) shows the surface features of g-C with $245 \times 239 \mu\text{m}^2$ lateral dimensions, and with ~ 1 nm rms roughness. Unlike the basal plane of graphite, the g-C surface has significant height variation over these lateral dimensions. As we reduced the lateral dimensions of the optical interferometry image, the surface roughness was also reduced, as seen in Fig. 14 (b). For $140 \times 185 \mu\text{m}^2$ lateral dimensions, we observed 0.7 nm rms roughness. The rms roughness was decreased by 70% for a 50% reduction in lateral dimensions. These lateral dimensions are still very large considering the ranges of the Kr - C-atom and the Kr - Kr interaction potential, which will be discussed in chapter 3. Therefore, it is not meaningful to directly compare the rms roughness from these experiments with the rms roughness of the structural models of g-C, which will be treated in Section E. It should be noted that, in this experiment the average roughness level of the g-C films are flat in these lateral dimensions. This supports the assumption that the average g-C surface is flat and the flat surface approximation of the RDM and CMM, discussed in Section 2-5, is reasonable.

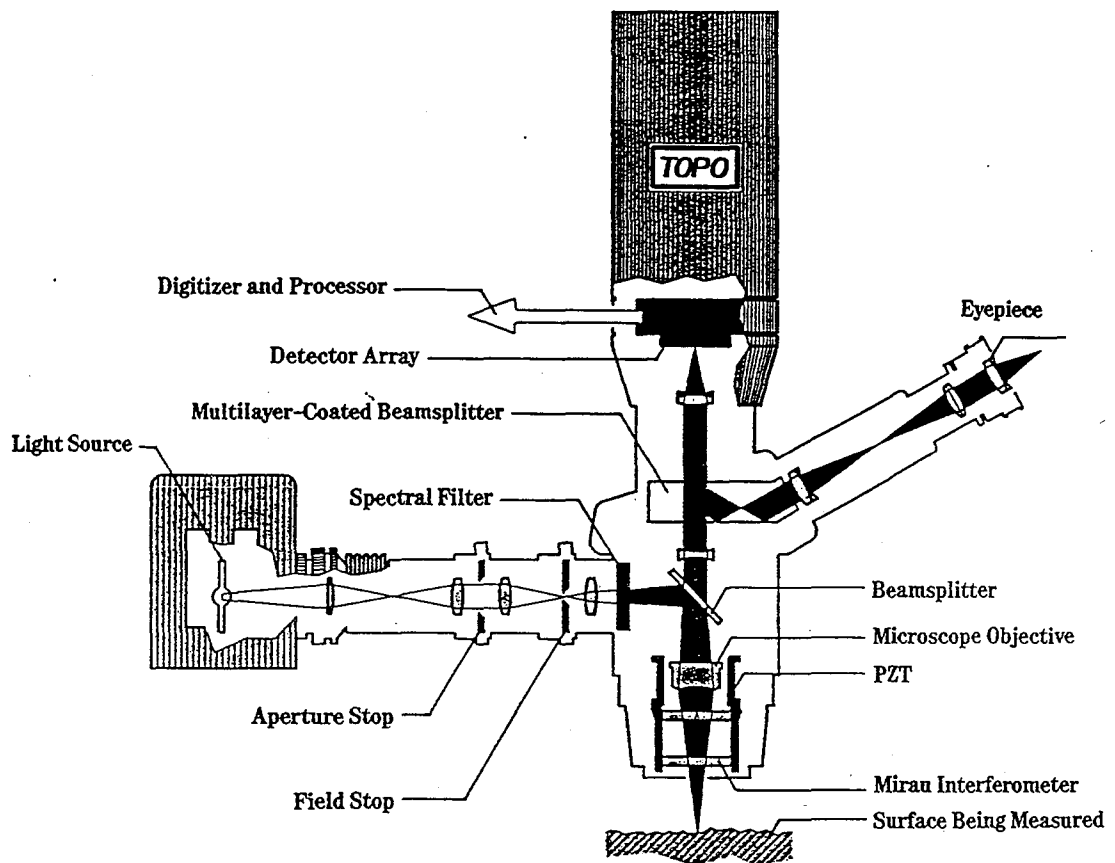


FIG. 13. A schematic diagram of an optical interferometer. After ref. 47.

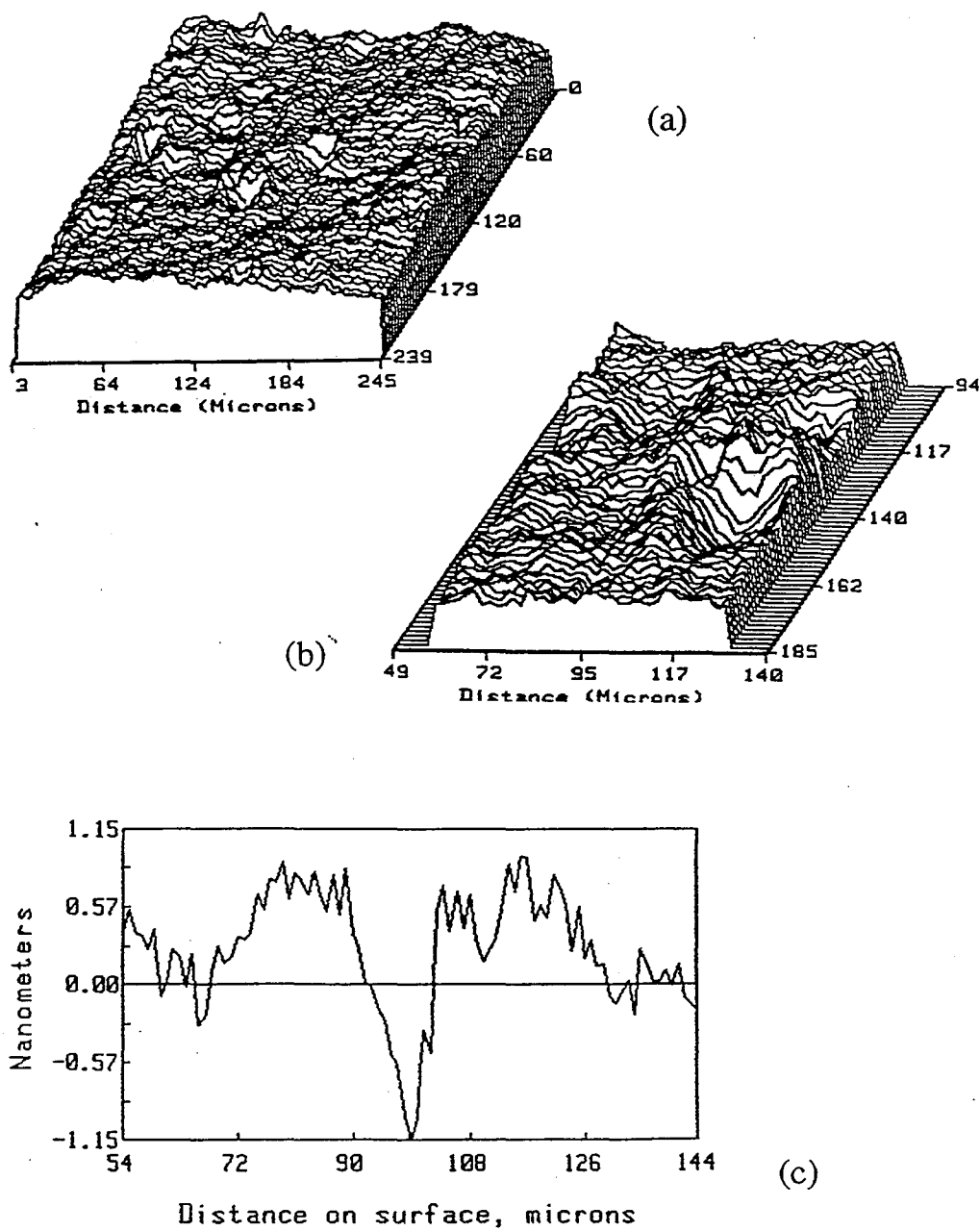


FIG. 14. (a - b) 3D diagram of the surface morphology of g-C obtained by optical interferometry. (c) 2D profile of the surface morphology of g-C.

d. Scanning tunneling microscopy: The g-C films were mounted on flat metal disks for STM analysis following the instruction of ACF⁴² and were then dried in air.

Atomic resolution of STM comes from piezoelectric control of a metallic tip within the angstrom range of height from the surface of a sample. In this height range, there is a tunneling current between the tip and the surface of the sample caused by applying a bias voltage between them.⁴⁸ Basically, there are two STM image modes. One is a “constant height” mode. In this mode, the tunneling current is imaged for a constant probe height above the surface. The other mode is a “constant current” mode, where the tip height is adjusted to maintain constant current and the height is imaged.⁴⁹ Typical vertical and horizontal resolution limits of STM are less than 0.1 nm and 0.2 nm, respectively.⁵⁰

STM investigations were performed in air with a Nano Scope II from Digital Instruments in Dr. Greg Swain’s laboratory in the Department of Chemistry and Biochemistry at Utah State University. Tungsten tips were used as the tunneling tips. Tunneling biases were set to 20.1 mV for the image in Fig. 15(a) and 25.0 mV for the image in Fig. 15(b). The constant current mode (set to 2.0 nA) was used for both images. For the first image, data were collected with 200 pixels/scan. For the second image, there were 400 pixels/scan. These operating parameters are similar to those used by Marchon *et al.*³⁸

To date our STM experiments have not been able to observe raft sizes or the structures of rings. However, we did determine the surface roughness of g-C clearly. Fig. 15(a) shows the surface features of g-C with $500 \times 500 \text{ nm}^2$ lateral dimensions. As we can see from this image, the surface of g-C is quiet smooth. The degree of smoothness of g-C surface can be seen more clearly in Fig. 15(b). With $9 \times 9 \text{ nm}^2$ lateral dimensions, this experiment shows about 0.8 Å rms roughness. Even this small roughness may be a result of instrumental resolution limitations rather than intrinsic

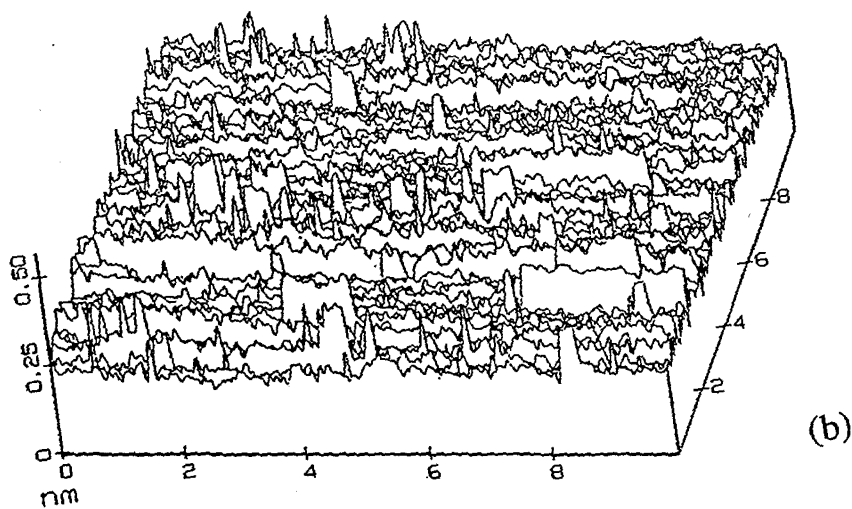
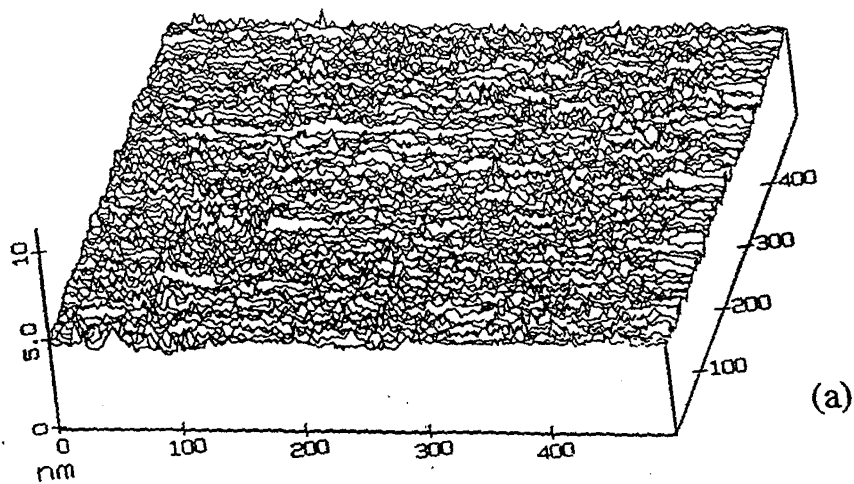


FIG. 15. Surface morphology of g-C thin film with scanning tunneling microscope.

surface roughness since the rms roughness is less than the typical vertical resolution limit of STM. Higher resolution experiments are in progress.

E. Structural model for interaction energy calculations

To investigate the physisorption of Kr on g-C, a structural model of g-C is necessary. In Section C, the use of the C1120 model of g-C was proposed for two reasons. First, C1120 is a reasonable model for the structure of g-C materials, which is in close agreement with a variety of experiments and adequately predicts most of the basic physical properties of g-C. Secondly, the physical properties and structure of C1120 are similar to those of graphite. As will be discussed in detail in Chapter 3, the interaction potentials between a Kr atom and a C-atom of graphite and between two Kr atoms on graphite will be used for those between a Kr atom and a C-atom of g-C and between two Kr atoms on g-C. This approximation is valid, if g-C has similar physical characteristics to graphite. Especially for the approximation for the Kr - Kr interaction potential on g-C, we need high ratio of sp^2 bonding (refer to Chapter 3).

1. Hierarchy of the structural model

Although the C1120 model is sufficient to describe many aspects of g-C, it is insufficient to use the C1120 model alone to perform the Kr - g-C interaction energy calculations since (i) the exact positions of all the C-atoms in the C1120 model are not known (though we know its physical properties and ring statistics), and (ii) the dimensions of the C1120 model are not big enough to be considered as a semi-infinite substrate. Thus, it is necessary to extend the C1120 structural model for g-C to complete the Kr - g-C interaction energy calculation. We employ a hierarchy of three structural models, with increasing levels of positional detail, for decreasing radial distances of the C-atoms from the central Kr atom, as indicated in Fig. 16. The three levels of approximation are described in detail below.

a. Continuous medium model: The continuous medium model (CMM) consists of an effective continuous medium, which has an average density ρ_o of carbon atoms matching that of the C1120 model (2.11 g/cm³ or 0.113 carbon atoms per Å³). The CMM is a homogeneous and isotropic model.

This model has several limitations. First, it contains no information about wrinkling on the surface. One of the most distinctive characteristics of g-C substrates, in contrast to the basal planes of graphite, is that g-C substrates have wrinkling on their surfaces. Especially for carbon atoms close to the central Kr atom, where the Kr - C-atom interaction potential, ϕ_{Kr-C} , does not vary linearly (see Chapter 3), the CMM alone provides an insufficient model for the structure of g-C.

For carbon atoms far from the origin, the CMM gives reasonably good interaction energy calculation results. We base this on two assertions. First, as the distance between a given carbon atom and the central Kr atom is increased, ϕ_{Kr-C} varies rapidly and approaches to zero and then varies slowly with very small gradients. If the distance is large enough, then small variations in the exact positions of the carbon atoms do not make any significant differences in the interaction energy calculations. Second, in amorphous solids, information about the local structure of one part of a solid is not sufficient to uniquely determine the structure of other distant parts. In other words, the positions of C-atoms of one part of g-C are not correlated with those of others far apart from it. In this region, it is possible to treat g-C statistically as a continuous medium using its average density and the CMM model. In summary, the CMM is a good approximate model for describing the part of g-C far from the central Kr atom, but is not appropriate for modeling carbon atoms close to the central Kr atom.

b. Radial distribution model: The radial distribution model (RDM) is also a continuous medium model like the CMM. The RDM is isotropic, but not homogeneous, unlike the CMM. The density function (sometimes referred to as the

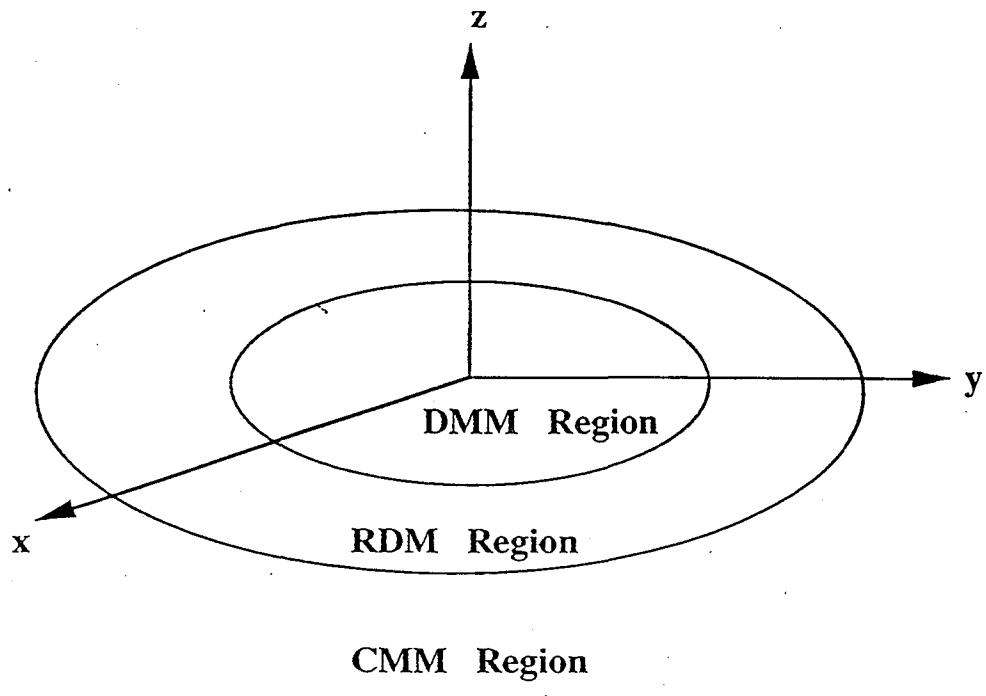


FIG. 16. A schematic diagram of the hierarchy of the structural model of g-C.

atomic pair correlation function), $\rho(r)$, used in the RDM, is a function of the radial distance r from the origin (located at the C-atom from which the RDF was calculated; refer to Section C-c above) and is given by

$$\rho(r) = \frac{J(r)}{4\pi r^2} \quad (2.E.1)$$

where $J(r)$ is the RDF. $J(r)$ of the C1120 model is shown in Fig. 6; it provides information about the angular averaged distribution of C-atoms about a C-atom at the origin. Thus, the statistical distribution of distances of C-atoms from the central Kr atom can be determined using $J(r)$. Since $\phi_{\text{Kr-C}}$ is a central potential, $\phi_{\text{Kr-C}}$ is only a function of distances between the central Kr atom and C-atoms. As a consequence, the RDM provides a statistically averaged interaction energy.

In the intermediate range (about 4 Å to 6 Å), the interaction potential between a Kr atom and a C-atom of g-C, $\phi_{\text{Kr-C}}$, does not vary linearly with respect to r (refer to equation 3.C.1). In this range, the interaction energy calculation is affected by position variations of the C-atoms even though their positions vary randomly. As a consequence, the CMM has insufficient positional detail for accurate interaction energy calculations in this range.

Because the RDM is also a continuous medium model, it is again not possible to represent the wrinkling of g-C substrates. As a result, it is impossible to investigate the effect of the wrinkling of g-C substrates on physisorption of Kr on g-C with the RDM and CMM alone.

c. Discrete medium model: The RDF's calculated for the C1120 model and those measured by Mildner for g-C extend down to nearest neighbors, so in principle the RDM could be used to calculate the interaction energies for all C-atoms up to the upper limit of the RDF's (~ 6 Å). However, we know a good deal more about the SRO and MRO of g-C than is contained in the RDF.

The discrete medium model (DMM) improves the interaction energy calculation

by using a statistical ensemble of MRO structures (three ring clusters) for which the exact positions of the C-atoms can be specified (in some approximation) for each member of the ensemble. The DMM uses an ensemble of three ring clusters composed of 5-, 6-, and 7-membered rings as shown in Fig. 7. Each three ring cluster of the ensemble occurs with a probability calculated using Beeman's ring statistics for the C1120 structural model²⁹ (see Appendix 2 and Table IV). In this section we must determine the positions of the C-atoms for each three ring cluster, and the probability distribution of the three ring clusters. In Chapter 4, the interaction energies for each three ring cluster are determined.

In constructing three ring clusters, we begin by using regular pentagons, hexagons, and heptagons for 5-, 6-, and 7-membered rings, respectively. Ideally, these regular structures should be relaxed to a minimum energy configuration, by allowing for variations in the bond lengths and bond angles and for the structure to be nonplanar. For graphite, the bond-stretching force constant f_r is larger than in-plane or out-of-plane bond-angle-bending force constant, f_θ or f_ϕ , even though there are discrepancies in these values from literature to literature (refer to Table VI). Therefore, it is reasonable to assume that the intraplanar sp^2 bonding length is kept nearly constant and close to the graphite bond length. The remaining parameters determining the geometrical structures of three ring clusters, are the in-plane and out-of-plane bond angle variations. The preferred method would be to search the bond angle (both in-plane and out-of-plane) parameter space to determine the bond angles for the minimum energy configuration based on bond angle bending force constants for carbon bonds like those developed by Tersoff.⁵¹ However, there is considerable disagreement in the values of these force constants.^{29, 52-59} In addition, the finite size of the ring clusters considered and boundary effects have a major impact on the minimum energy configuration unless one minimizes the structure of rafts much larger than three ring clusters. Preliminary

attempts to find the minimum energy configurations for six to eight ring clusters by Ali Sabbah, using the standard energy minimization package for chemical structures called PC Model,⁶⁰ were not successful; minimum energy structures varied significantly depends on initial configuration of the structures, which indicated that the energies were local minima. Finally, it is difficult to take into account the effects of adjacent rafts, sp^3 bonding, or other structures not in the plane of the quasi-2D ring clusters, even if ring clusters are constructed.

Given these difficulties in determining minimum energy configurations for the three ring clusters, we can found it necessary to resort to greatly simplified structural models. Two limiting cases were considered. The first case is that f_ϕ is much larger than f_θ . Then, the distortions of bond angles of rings will be in-plane. As a result, the structures of the three ring clusters will be flat. The other case is that f_θ is much larger than f_ϕ . For this case, the structure of the three clusters will be out-of-plane in contrast to the above case, and will be convex or concave. The practical structures of g-C surface will be within these two limiting cases. In this thesis, the first limiting structures were adapted for $\theta_1 + \theta_2 + \theta_3 > 2\pi$ case and the second limiting case was used for $\theta_1 + \theta_2 + \theta_3 \leq 2\pi$ case, where the angles θ_1 , θ_2 , and θ_3 are defined in Fig. 17. Refer to Appendix 3 for the determination of C-atom coordinates of DMM.

To complete the DMM, we need the probability distribution of the three ring clusters. These are calculated from the ring statistics of the C1120 model in Appendix 2 and are listed in Table IV.

2. Joining the models

a. Crossover from CMM to RDM: The valid region for the CMM is the range of r where the interaction potential between a Kr atom and a C-atom, ϕ_{Kr-C} , varies very slowly with a nearly zero gradient. By considering the graph of the parameterized Lennard-Jones 6-12 potential in Fig. 20 (shown later) and the specific potential $\phi_{Kr-C}(r)$

TABLE VI. Force constants of graphite in dyne/cm.

	f_r	f_θ	f_ϕ
Beeman <i>et al.</i> ²⁹	3.63×10^5	0.360×10^5	1.34×10^5
Nicklow <i>et al.</i> ⁵³	3.62×10^5	0.322×10^5	2.99×10^5
Al-Jishi <i>et al.</i> ⁵⁴	3.13×10^5	2.670×10^5	0.875×10^5
Tuinstra <i>et al.</i> ⁵⁷	4.32×10^5	0.250×10^5	--
Spence <i>et al.</i> ⁵⁸	7.10×10^5	0.670×10^5	--
Yoshimori <i>et al.</i> ⁵⁹	6.71×10^5	0.480×10^5	--
Young <i>et al.</i> ⁵⁵	4.36×10^5	0.380×10^5	--

for the Kr - g-C interactions in Fig. 25 (shown later), the upper limit of the valid region is about 1.5σ to 2σ or 5.2 \AA to 7.0 \AA . On the basal plane of graphite, the most stable physisorption height of Kr above the basal plane is 3.43 \AA .³ If we use this height as the approximate physisorption height of Kr on g-C, the radial distance from the origin (not from the central Kr atom) above which the CMM becomes valid is from 3.9 \AA to 6.1 \AA . The RDF of the C1120 model was calculated by Beeman for distances up to 6 \AA .²⁹ Besides this facts, the variation of the density $\rho(r)$ calculated with the radial distribution function $J(r)$ of C1120 is vary small for $r > 5 \text{ \AA}$ (see Fig. 18). Therefore, it is reasonable to choose the crossover from CMM to RDM at $r > 5 \text{ \AA}$. The crossover take place at 5.881 \AA in our interaction energy calculations.

b. First layer g-C and bulk g-C: If we model the near region of the g-C substrate as made up of a quasi-planar DMM portion and a bulk RDM portion [as shown in Fig. 19(a)], the model predicts a hemispherical void below the DMM portion which results from the transition from the DMM to RDM structural models. This dented part of the RDM causes the interaction energies above this region to be lowered anomalously. To

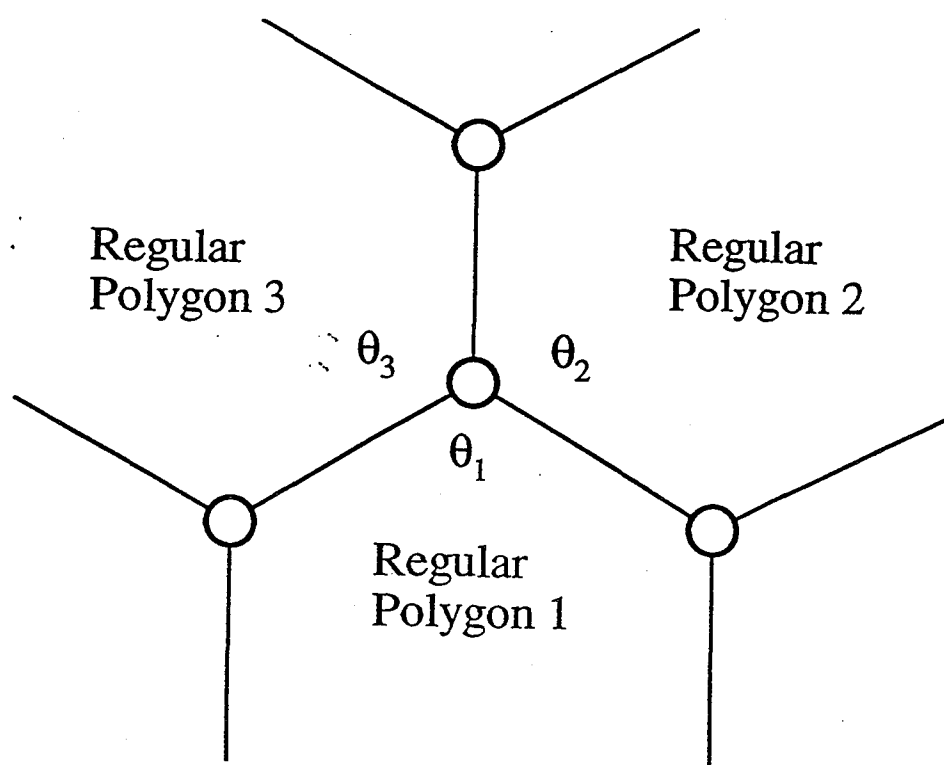


FIG. 17. A schematic diagram indicating the three angles defined by the intraplanar sp^2 bonds.

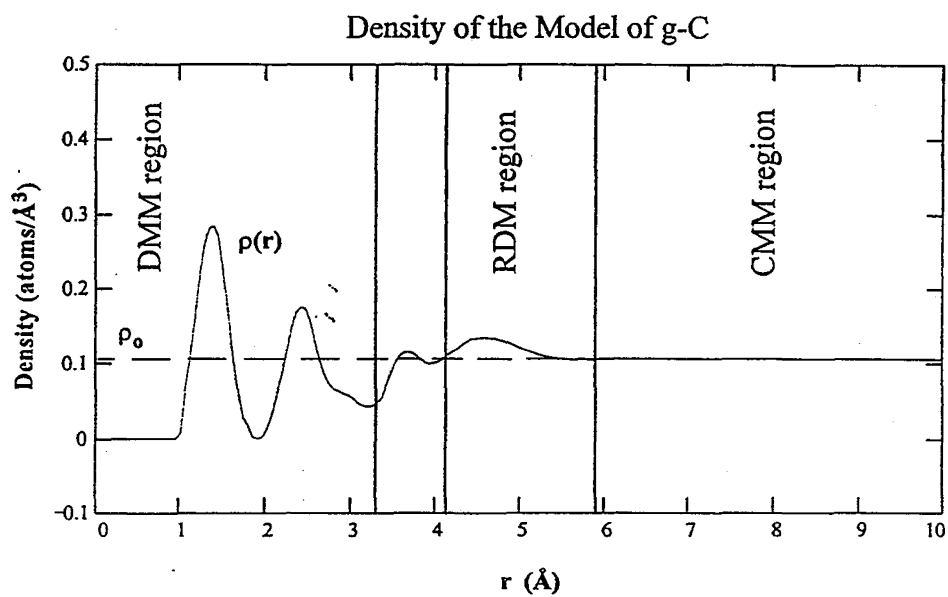


FIG. 18. The variation of the density $\rho(r)$ calculated with $J(r)$ of C1120.

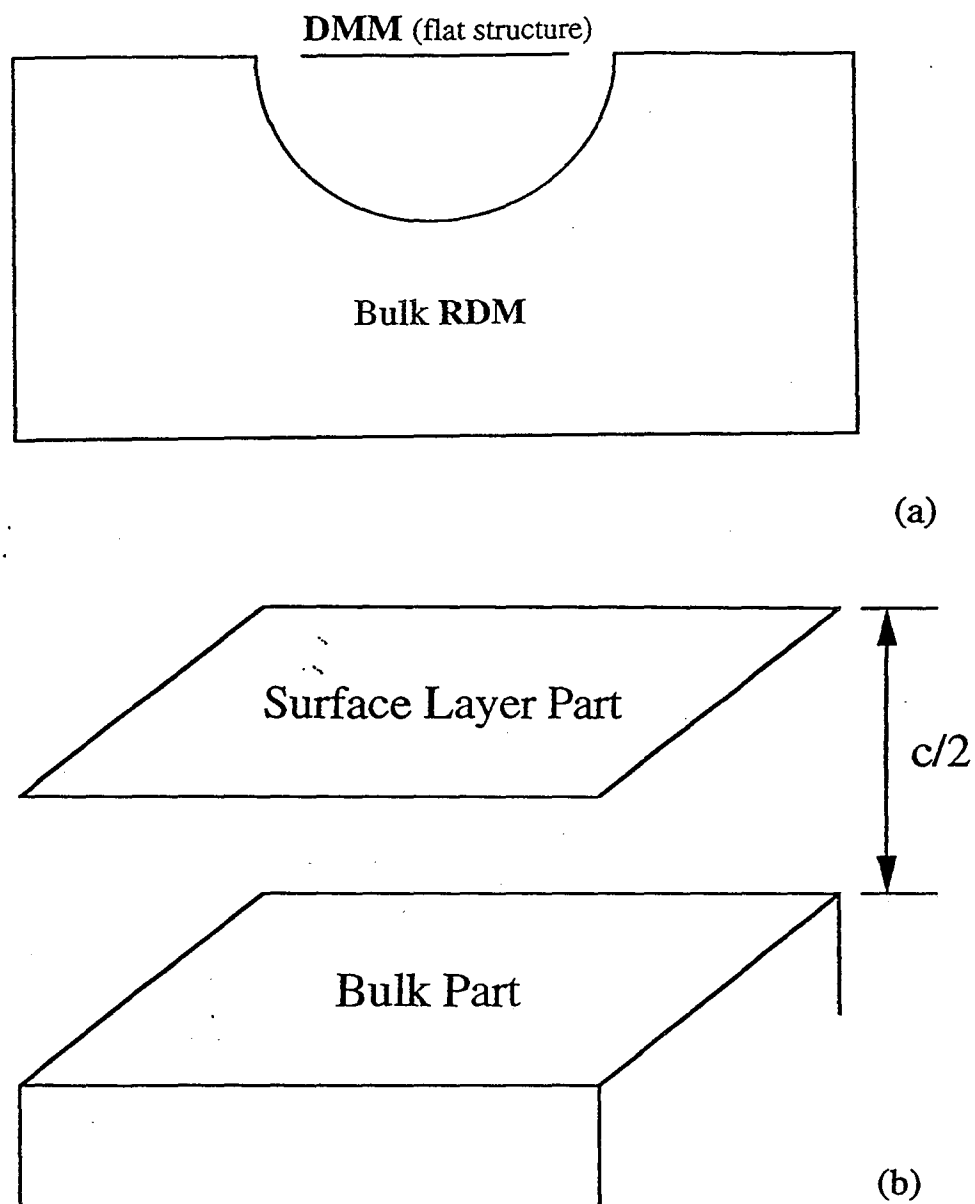


FIG. 19. (a) An appropriate model of the near region of g-C with only a quasi-planar DMM region and a bulk RDM region. (b) Preferred division of g-C into a surface layer component and a bulk component.

avoid this anomaly, the region modeled by the RDM was separated into first layer and the bulk g-C components, as shown in Fig. 19(b).

The first layer portion of our g-C consists of CMM, RDM, and DMM regions. The CMM of the first layer g-C has a surface density $\frac{c}{2} \cdot \rho_0$, where ρ_0 is the average density of the C1120 model and $\frac{c}{2}$ is the interplanar distance of graphite. The factor of $\frac{c}{2}$ is used to convert the volume density of the C1120 model to a surface density. Similarly, the surface density function used with the first layer RDM region of g-C is $\frac{c}{2} \cdot \frac{J(r)}{4\pi r^2}$. As discussed above, the DMM region consists of the quasi-planar three ring clusters. The bulk portion of g-C is composed of CMM and RDM regions only, to avoid creating the dented part of the RDM for the bulk g-C.

c. Crossover from RDF to DMM: The RDF and DMM crossover occurs at a radius R in the first layer region defined by

$$\begin{aligned} &\text{the number of C-atoms} \\ &\text{in a three ring cluster} \end{aligned} = \int_0^R dr 2\pi r \frac{c}{2} \frac{J(r)}{4\pi r^2}. \quad (2.E.12)$$

This equation comes from the conservation requirement that the total number of C-atoms of this model of g-C should be equal to that of real g-C. As an example, for the 555 three ring cluster, the corresponding R is determined by

$$10 = \int_0^R dr 2\pi r \frac{c}{2} \frac{J(r)}{4\pi r^2}, \quad (2.5.13)$$

since the 555 three ring cluster has 10 C-atoms. Table VII shows the number of C-atoms within a circle of radius R defined by $\int_0^R dr 2\pi r \frac{c}{2} \frac{J(r)}{4\pi r^2}$. Based on these

calculation results, Table VIII shows the crossover radius R of each three ring cluster.

TABLE VII. Number of C-atoms in the circle with radius R. (refer to Fig. 16).

R (Å)	Number of carbon atoms	R (Å)	Number of carbon atoms	R (Å)	Number of carbon atoms	R (Å)	Number of carbon atoms
3.01	8.926	3.31	9.846	3.61	11.614	3.91	14.225
3.02	8.961	3.32	9.879	3.62	11.699	3.92	14.308
3.03	8.996	3.33	9.912	3.63	11.788	3.93	14.389
3.04	9.030	3.34	9.945	3.64	11.873	3.94	14.471
3.05	9.063	3.35	9.982	3.65	11.963	3.95	14.554
3.06	9.098	3.36	10.023	3.66	12.048	3.96	14.637
3.07	9.128	3.37	10.062	3.67	12.138	3.97	14.719
3.08	9.158	3.38	10.102	3.68	12.229	3.98	14.803
3.09	9.189	3.39	10.145	3.69	12.317	3.99	14.887
3.10	9.220	3.40	10.190	3.70	12.408	4.00	14.971
3.11	9.249	3.41	10.237	3.71	12.498	4.01	15.058
3.12	9.279	3.42	10.285	3.72	12.585	4.02	15.143
3.13	9.309	3.43	10.334	3.73	12.677	4.03	15.229
3.14	9.338	3.44	10.393	3.74	12.767	4.04	15.315
3.15	9.367	3.45	10.449	3.75	12.856	4.05	15.402
3.16	9.396	3.46	10.505	3.76	12.945	4.06	15.485
3.17	9.425	3.47	10.567	3.77	13.036	4.07	15.575
3.18	9.453	3.48	10.632	3.78	13.123	4.08	15.665
3.19	9.482	3.49	10.696	3.79	13.211	4.09	15.757
3.20	9.509	3.50	10.760	3.80	13.298	4.10	15.850
3.21	9.535	3.51	10.833	3.81	13.385	4.11	15.943
3.22	9.564	3.52	10.905	3.82	13.471	4.12	16.037
3.23	9.598	3.53	10.974	3.83	13.556	4.13	16.132
3.24	9.631	3.54	11.049	3.84	13.642	4.14	16.226
3.25	9.663	3.55	11.125	3.85	13.726	4.15	16.319
3.26	9.691	3.56	11.202	3.86	13.810	4.16	16.414
3.27	9.717	3.57	11.284	3.87	13.895	4.17	16.513
3.28	9.749	3.58	11.365	3.88	13.978	4.18	16.608
3.29	9.781	3.59	11.447	3.89	14.061	4.19	16.716
3.30	9.814	3.60	11.531	3.90	14.144	4.20	16.819

TABLE VIII. Crossover radius R of three ring clusters.

Three Ring Cluster	R (Å)	Three Ring Cluster	R (Å)
555	3.30	577	4.00
556	3.53	666	3.77
557	3.65	667	3.80
566	3.65	677	4.00
567	3.77	777	4.12

CHAPTER 3

INTERACTION ENERGY CALCULATION

A. Introduction

The basic purpose of this thesis research is to study the physisorption of Kr on g-C. Naturally, this raises three questions: (i) will Kr atoms be physisorbed on g-C; (ii) if Kr physisorbed on g-C, then what would its adlayer structure be; and (iii) how would this structure differ from that on graphite? To answer these questions we need three things: (i) the lateral adsorbate-adsorbate interaction energy between two Kr atoms on g-C, (ii) the average binding energy of a Kr atom on g-C, and (iii) the corrugation of Kr-g-C interaction energy on the g-C surface. These three things can be determined through two interaction energy calculations, the Kr-g-C interaction energy and the Kr-Kr interaction energy on g-C.

To investigate these two interactions, we have to consider (i) what is the interaction potential between a Kr adatom and the g-C substrate, $\phi_{\text{Kr-C}}$, (ii) what is the interaction potential between two Kr atoms on g-C, $\phi_{\text{Kr-Kr}}$, (iii) how do we calculate the interaction energies using $\phi_{\text{Kr-C}}$ and $\phi_{\text{Kr-Kr}}$, and (iv) how reliable are these calculation methods? As will be discussed in Sections C and D, $\phi_{\text{Kr-C}}$ and $\phi_{\text{Kr-Kr}}$ are Lennard-Jones 6-12 potentials. There will be a brief overview of the Lennard-Jones 6-12 potential in Section B. In Section C, $\phi_{\text{Kr-C}}$ will be discussed in detail. Section D will deal with $\phi_{\text{Kr-Kr}}$ on g-C. The interaction energy calculation methods will be considered in Section E. In Section F, the reliability of these calculation methods will be estimated by comparison of interaction energies of Kr on graphite calculated using the methods in Section E to previous calculations of these interaction energies. The interaction energy calculation results for Kr on g-C will be presented in Section G.

B. The Lennard-Jones 6-12 potential

The typical form of Lennard-Jones 6-12 potential shown in Fig. 20(a) is given by

$$\phi(r) = 4\varepsilon \left[\left(\frac{\sigma}{r} \right)^{12} - \left(\frac{\sigma}{r} \right)^6 \right] \quad (3.B.1)$$

where ε and σ are constants.⁶ The potential and its derivatives with respect to r are shown in Fig. 20(b). The potential, $\phi(r)$, is zero at a radius σ . The minimum in $\phi(r)$, found by setting $\left. \frac{d\phi}{dr} \right|_{r=r_{\min}} = 0$, is at

$$r_{\min} = 2^{1/6} \sigma \cong 1.122 \sigma. \quad (3.B.2)$$

Let us also define the radial distance r_c where $\left. \frac{d^2\phi}{dr^2} \right|_{r=r_c} = 0$. Then, r_c is given by

$$r_c = \left(\frac{26}{7} \right)^{1/6} \sigma \cong 1.244 \sigma. \quad (3.B.3)$$

C. Kr-C-atom interaction potential on g-C

There is not enough experimental data presently available to determine the Kr-C-atom interaction potential, $\phi_{\text{Kr-C}}$, on g-C. In this thesis, a modified form of the Kr-C-atom interaction potential on graphite will be used for the $\phi_{\text{Kr-C}}$ potential on g-C. This approximation is based on the structural similarity of the C1120 model with graphite as discussed in Section E.

There have been many investigations of Kr physisorbed on graphite and there are several different expressions for the interaction potential between a Kr adatom and a C-atom of graphite.^{11,61} Calculations in this thesis will use the computationally simple Lennard-Jones 6-12 pair-wise potential given by Crowell and Steele:¹¹

$$\begin{aligned} \phi_{\text{Kr-C}}(r) &= -67.6 \times 10^{-12} \left[\frac{1}{r^6} - \frac{(3.92)^6}{2} \frac{1}{r^{12}} \right] \text{erg/Kr-C pair} \\ &= 4\varepsilon \left[\left(\frac{\sigma}{r} \right)^{12} - \left(\frac{\sigma}{r} \right)^6 \right] \text{erg/Kr-C pair} \end{aligned} \quad (3.C.1)$$

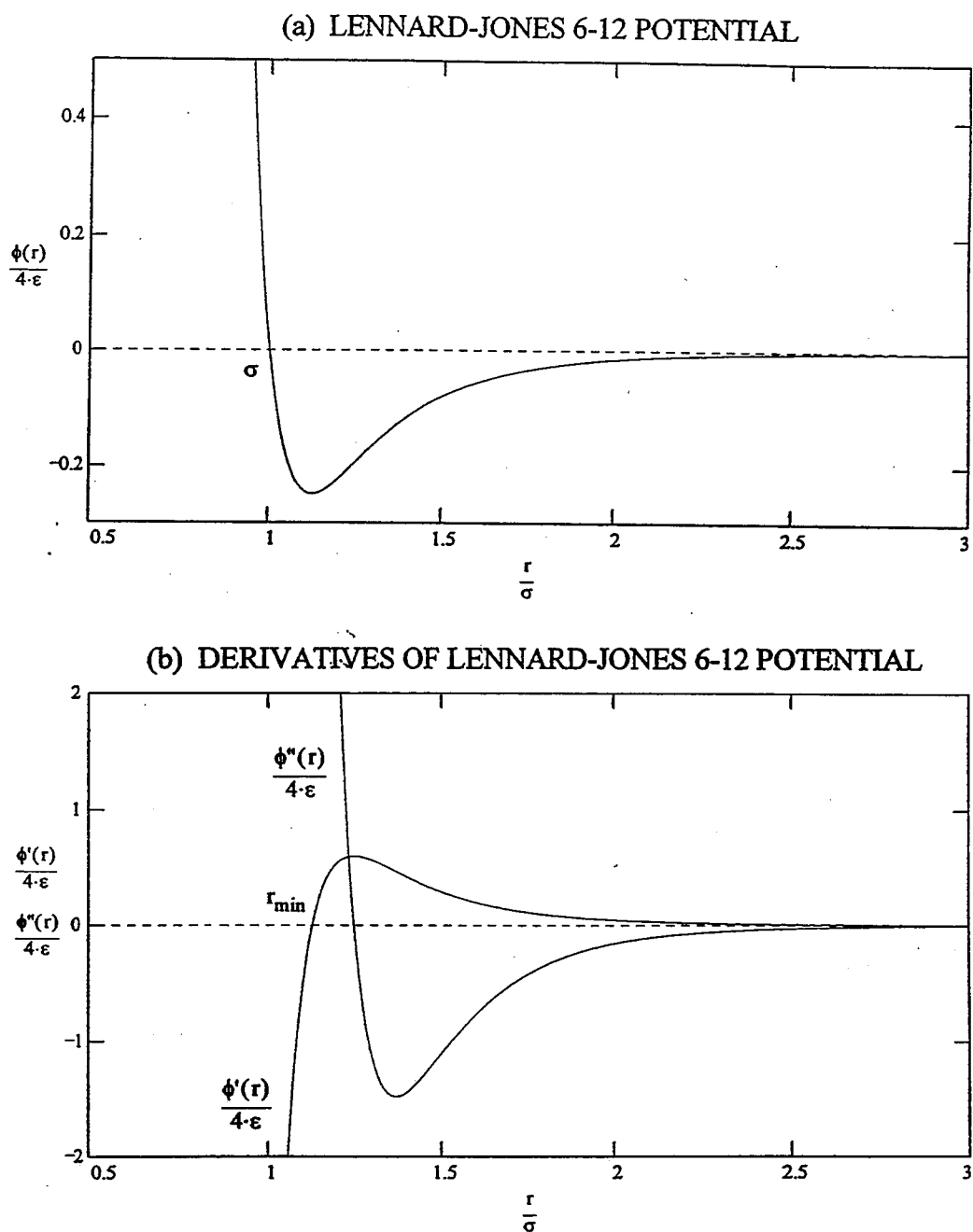


FIG. 20. (a) Typical form of the Lennard-Jones 6-12 potential and (b) its derivatives.

with $\sigma \approx 3.492 \text{ \AA}$ and $\epsilon \approx 9.32 \times 10^{-15} \text{ erg} = 5.82 \text{ meV}$.

To verify the accuracy of this simplified expression for $\phi_{\text{Kr-C}}(\mathbf{r})$, the interaction energy between a Kr atom and graphite was calculated with a full pair-wise summation using equation 3.c.1. (Details of the calculation are given in Section F.) Results of the calculation for Kr on graphite are compared in Table VIII to much more sophisticated extended calculations by Steele³ which included additional terms in the potential for $\phi_{\text{Kr-C}}(\mathbf{r})$. Agreement between these two calculations is acceptable, in light of the many additional approximation made in determining $\phi_{\text{Kr-C}}(\mathbf{r})$ for Kr on g-C.

D. Interaction potential between two Kr atoms on g-C

The exact interaction potential between two Kr atoms on g-C is not known, since the substrate modifies the interactions between Kr atoms. Fig. 21 shows schematically how the substrate affects the interaction between two atoms on the surface.⁶² McLachlan showed that the modified interaction energy is a function of the polarizability of the adsorbate atoms and the imaginary part of dielectric constant of the substrate.⁶² The author showed that at an imaginary frequency $\omega = i\xi$, the interaction energy between two atoms on a substrate is given by

$$\begin{aligned} W = & -\frac{\hbar}{(2\pi)^2} \int_0^{\infty} \text{Tr} \left\{ \alpha(i\xi) \cdot \mathbf{E}(\bar{\mathbf{a}}, \bar{\mathbf{b}}; i\xi) \cdot \beta(i\xi) \cdot \mathbf{E}(\bar{\mathbf{b}}, \bar{\mathbf{a}}; i\xi) \right\} d\xi \\ & -\frac{\hbar}{(2\pi)^2} \int_0^{\infty} \left\{ \text{Tr} \left[\alpha \cdot \mathbf{E}(\bar{\mathbf{a}}, \bar{\mathbf{b}}) \cdot \beta \cdot \hat{\mathbf{E}}(\bar{\mathbf{b}}, \bar{\mathbf{a}}) \right] + \text{Tr} \left[\alpha \cdot \hat{\mathbf{E}}(\bar{\mathbf{a}}, \bar{\mathbf{b}}) \cdot \beta \cdot \mathbf{E}(\bar{\mathbf{b}}, \bar{\mathbf{a}}) \right] \right\} d\xi \\ & -\frac{\hbar}{(2\pi)^2} \int_0^{\infty} \text{Tr} \left[\alpha \cdot \hat{\mathbf{E}}(\bar{\mathbf{a}}, \bar{\mathbf{b}}) \cdot \beta \cdot \hat{\mathbf{E}}(\bar{\mathbf{b}}, \bar{\mathbf{a}}) \right] d\xi \end{aligned} \quad (3.D.1)$$

where \mathbf{a} , \mathbf{b} are polarizability tensors of the two atoms and $\mathbf{E}(\bar{\mathbf{r}}, \bar{\mathbf{r}}'; i\xi)$ is the susceptibility tensor of free space between $\bar{\mathbf{r}}$ and $\bar{\mathbf{r}}'$. $\hat{\mathbf{E}}$ is defined by

$$\hat{\mathbf{E}}(\bar{\mathbf{r}}, \bar{\mathbf{r}}'; i\xi) = \pm \left(\frac{\epsilon(i\xi) - 1}{\epsilon(i\xi) + 1} \right) \mathbf{E}(\bar{\mathbf{r}}, \bar{\mathbf{r}}'; i\xi), \quad (3.D.2)$$

where ϵ is the dielectric constant of the substrate. The first term expresses the

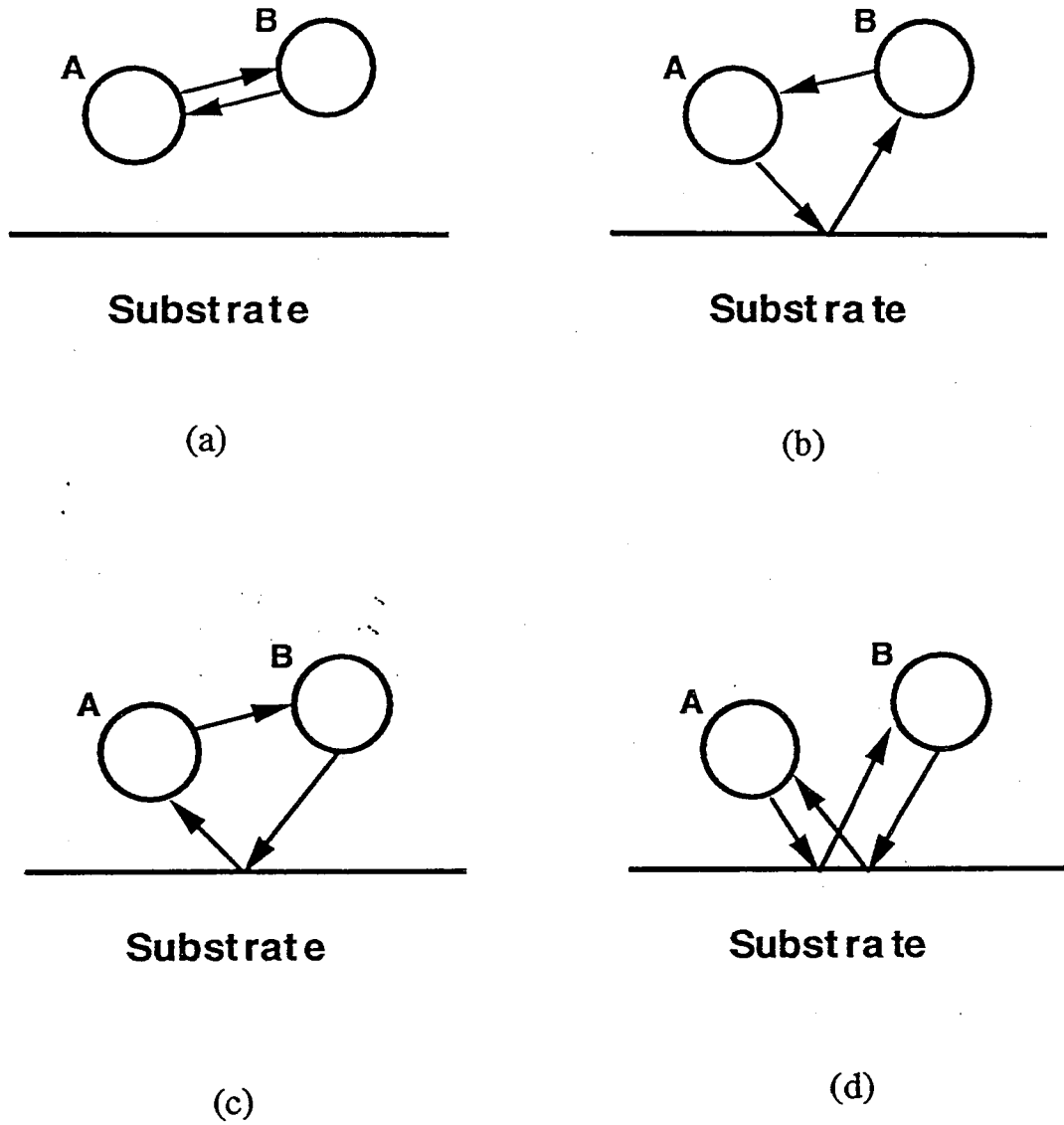


FIG. 21. The effect of the substrate on the interactions between adatoms. After ref. 62.

interaction of Fig. 21(a), the second term describes the interactions of Figs. 21(a) and (b), and the third corresponds the interaction of Fig. 21(d). The only difference between the Kr - graphite physisorption system and the Kr - g-C system is in the substrate. If the imaginary part of dielectric constant of g-C is approximately equal to that of graphite, then it is reasonable to use the interaction energy of Kr atoms on graphite for that of Kr on g-C.

Before discussing the experimental evidence which shows that the imaginary part of dielectric constant of g-C is quiet close to that of graphite, let us consider the basic reason why the dielectric constant of g-C should be close to that of g-C. The dielectric constant, ϵ , is defined by

$$\epsilon = 1 + 4\pi\chi_e \quad (3.D.3)$$

where χ_e is the electric susceptibility given by $\bar{P} = \chi_e \bar{E}$.⁶³ Here \bar{E} is an external electric field and \bar{P} is the induced polarization of the medium due to \bar{E} . Generally, ϵ and χ_e are second-rank tensors. For a given arrangement of specific constituent molecules, χ_e will be determined by (i) the polarizability of an individual constituent molecule, (ii) the density of the medium, (iii) the type of bonding between the constituent molecules, and (iv) the local structure of the medium. g-C and graphite have the same kind of constituent atoms (carbon atoms), and as a result they have same polarizability of a C-atom. Furthermore, they have (i) similar densities, (ii) same type of bonding (sp^2 bonding), and (iii) similar local structures. As a consequence, it is reasonable to expect that the dielectric constant of g-C will be approximately the same as that of graphite. Therefore, the interactions of Kr atoms on g-C must be similar to those of Kr on graphite.

Taft and Philipp⁶⁴ performed measurements of optical properties of several a-C's, which have different sp^2 and sp^3 bond ratios. In the measurements, they showed that n_{eff} , the effective number of valence electrons per atom taking part in optical

transitions, of these a-C samples approaches n_{eff} of graphite as the sp^2 bond ratio increases. n_{eff} is defined by

$$n_{\text{eff}} = \text{const} \cdot \int_0^{\omega_m} \omega \epsilon_2(\omega) d\omega, \quad (3.D.4)$$

where ω , ω_m , and ϵ_2 are the frequency of photons, a parametric cut-off frequency, and the imaginary part of dielectric constant, respectively. Fig. 22 shows the result of their measurements, where the ratios of sp^2 bonds of a-C₁, a-C₂, a-C₃, a-C₄, and a-C₅ are 56%, 44%, 30%, 25%, and 24%, respectively. Savvides⁶⁵ obtained an equivalent results. The author performed the same measurements for the same a-C's as Taft's. The results of the measurements were same as Taft's. Based on the above two measurement results, it is evident that n_{eff} (and therefore ϵ_2) of a-C approaches to that of graphite as the sp^2 bond ratio is increased. Since the sp^2 bond ratio of our model of g-C is 100%, the value of ϵ_2 for our model should be close to that of graphite. As a result, $\phi_{\text{Kr-Kr}}$ for our model should be similar to that of graphite.

Gordon and Villain⁵ have determined the pair-wise adsorbate - adsorbate potential between Kr atoms on graphite. Their potential is a Lennard-Jones 6-12 potential given by

$$\phi_{\text{Kr-Kr}}(r) = 9.4437 \times 10^{-14} \left[\left(\frac{3.60}{r} \right)^{12} - \left(\frac{3.60}{r} \right)^6 \right] \text{ erg/Kr - Kr pair} \quad (3.D.5)$$

where $\sigma = 3.60 \text{ \AA}$ and $\epsilon = 2.361 \times 10^{-14} \text{ erg} = 14.74 \text{ meV}$. This expression for $\phi_{\text{Kr-Kr}}$ will also be used for the Kr on g-C. The σ and ϵ of free Kr atoms are 3.65 \AA and $2.25 \times 10^{-14} \text{ erg}$, respectively.⁶ The differences between σ and ϵ of Kr atoms on graphite and those of free Kr atoms are less than 5%. This reflects that the modification of Kr - Kr interaction potentials that the approximation to use $\phi_{\text{Kr-Kr}}$ on graphite for $\phi_{\text{Kr-Kr}}$ on g-C is reasonable.

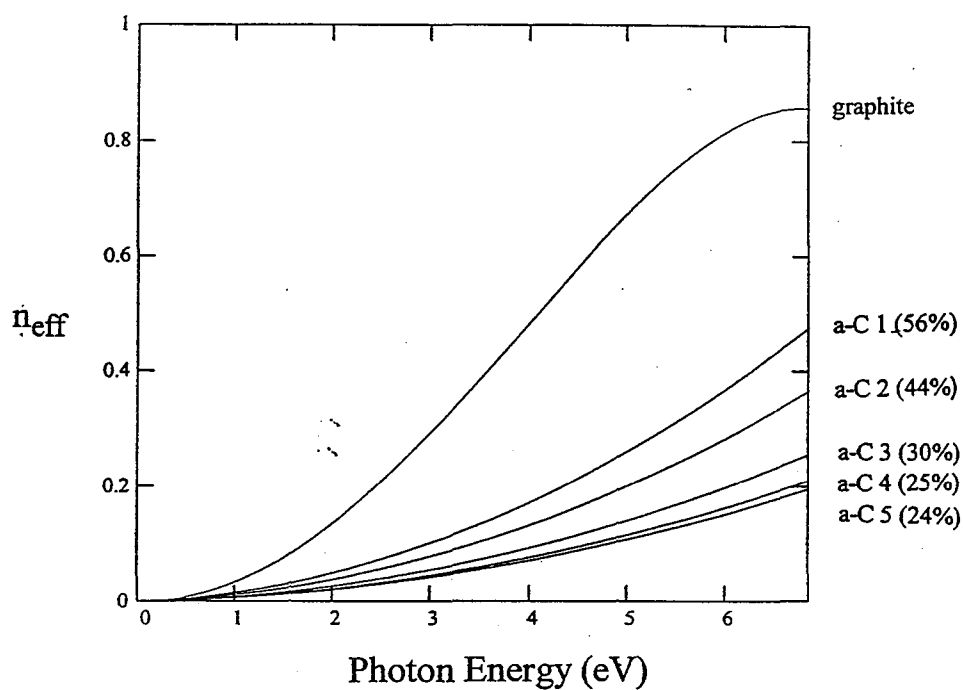


FIG. 22. The effective number of valence electrons per atom, n_{eff} , versus photon energy for several a-C's. The ratios of sp² bonds of a-C₁, a-C₂, a-C₃, a-C₄, and a-C₅ are 56%, 44%, 30%, 25%, and 24%, respectively. After ref. 64.

E. Methods of interaction energy calculations on graphitic amorphous carbon

1. Kr - Kr interaction energy calculation method

The Kr - Kr interaction potential for Kr on graphite given by equation 3.D.5 is used in this thesis for Kr - Kr interaction potential for Kr on g-C. As a result, there is no difference between the calculated Kr - Kr interaction energy for Kr on g-C and that for Kr on graphite.

2. Kr - g-C interaction energy calculation method

The potential for the interaction between a Kr atom and a C-atom of both graphite and g-C is given by equation 3.C.1. For the DMM, the interaction energy between the central Kr atom and the DMM region will be obtained from a pair-wise summation of the Kr - C-atom interactions using the discrete position information of the C-atoms from our structural model. The interaction energy calculations for the central Kr atom and particle density $\rho(r)$ of the RDM and ρ_0 of the CMM will involve integration instead of pair-wise summation. Section E in chapter 2 detailed our determination of the positions of the carbon atoms. The remaining information necessary for this calculation is the positions of the central Kr atom (physisorption sites) relative to the carbon substrate.

The DMM is an ensemble of three ring clusters. Thus, studying Kr physisorption at all sites for each three ring cluster would lead a complete investigation of Kr physisorption on g-C. However, it is impractical to calculate the interaction energy between the central Kr atom and g-C for all sites for each three ring cluster. We limit our calculations to physisorption sites along the symmetric lines and intraplanar sp^2 bond branches of each three ring cluster as shown schematically in Fig. 23 for a 567 cluster. A *three ring cluster* is generally not exactly symmetric about either the symmetric line of a ring or the intraplanar sp^2 bond branches. As a result, the minimum

or maximum interaction energy for the ring may not be located exactly on either the symmetric line of the ring or the intraplanar sp^2 bond branches. However, *each ring* is exactly symmetric about its symmetric line and the configuration of other C-atoms belonging to other two rings are approximately symmetric about the symmetric line. Therefore, the minimum or maximum interaction energy physisorption sites should be located close to the symmetric lines.

The parametric variation of the central Kr atom position can be divided in two parts: (i) horizontal variation that is parallel to the plane of the rings in a three ring cluster and (ii) vertical variation perpendicular to this plane. For a given three ring cluster, we consider horizontal variation along three symmetric lines and three intraplanar sp^2 bond branches (refer to Fig. 23). The horizontal variation along the symmetric lines of a ring is $\frac{r_i}{12}$, where r_i is the radius of the circle circumscribing i^{th} polygon, where $i=5, 6, \text{ or } 7$. The horizontal variation along the intraplanar sp^2 bond branches is $\frac{a}{12}$, where a is the intraplanar sp^2 bond length. Therefore, we consider 13 physisorption sites on each symmetric line and 7 on each intraplanar sp^2 bond branch, respectively. The physisorption site just above the central C-atom is common for all cases. As a result, $1 + 3 \times 12 + 3 \times 6$ or 45 physisorption sites will be considered for each three ring cluster for a given height. For many three ring clusters, many of these sites are equivalent. For example, only sites along one symmetry line and one intraplanar sp^2 bond branch need be considered for a 555 three ring cluster.

The vertical increment of the central Kr atom is 0.1\AA . The interaction energy is calculated at each of the 45 physisorption sites as a function of height. The height is incremented until the minimum interaction energy at each of the 45 physisorption sites is found.

Once the minimum Kr - g-C interaction energies for all physisorption sites of a ring are found, the minimum and maximum Kr - g-C interaction energies over the ring

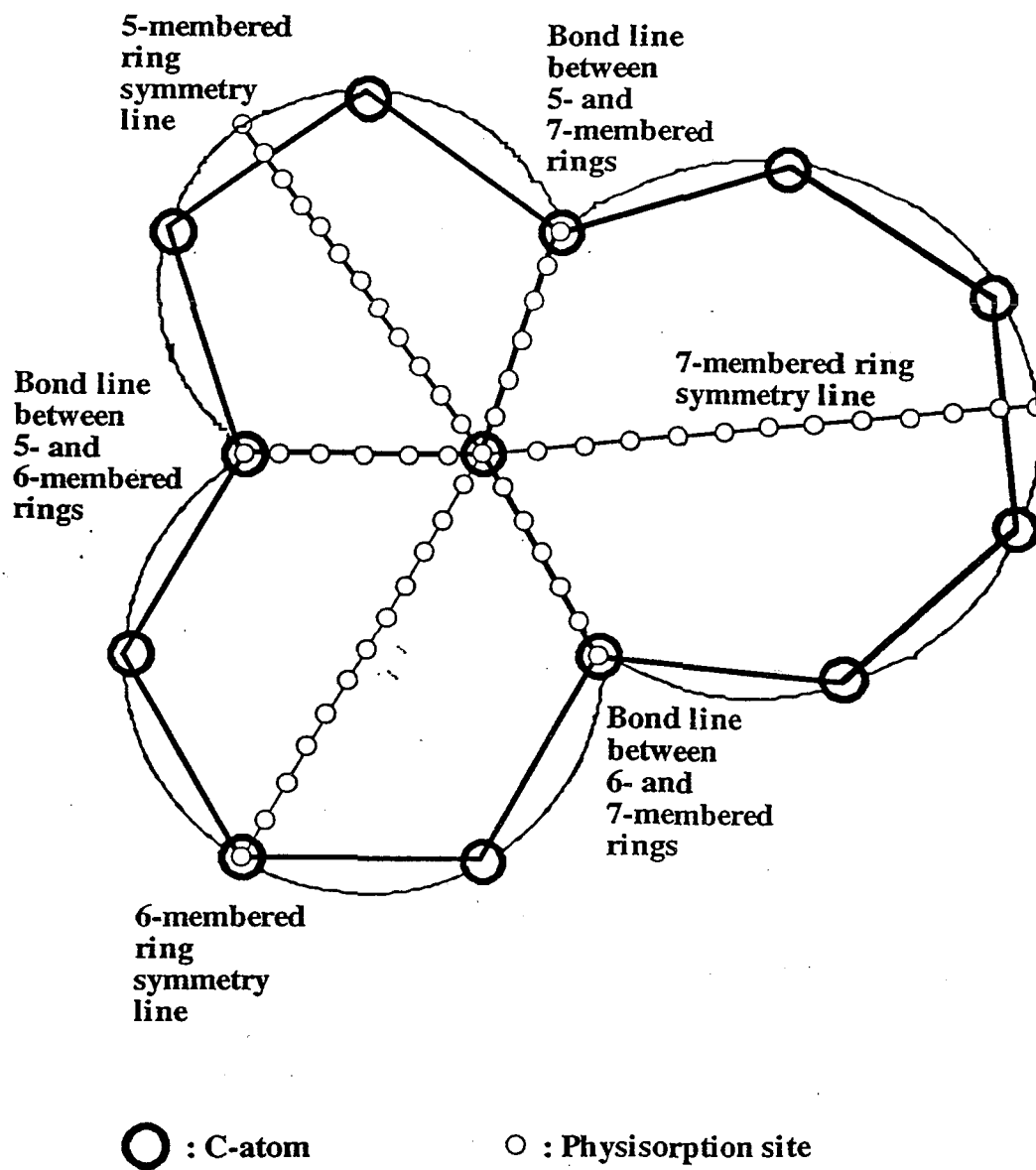


FIG. 23. Physisorption sites on a 567 three ring cluster.

surface are determined. The difference of these minimum and maximum Kr - g-C interaction energies is the corrugation of the ring. Using the ring statistics and the probability distribution of the three-ring cluster ensemble, the weighted average minimum and maximum Kr - g-C interaction energies of Kr on g-C, and the corrugation of g-C substrate are calculated.

F. Kr-graphite interaction energy calculation

To determine the accuracy of the Kr - g-C interaction energy calculations, Kr - graphite interaction energies were calculated using $\phi_{\text{Kr-C}}$ given by the equation 3.C.1 using three different methods: (i) a full summation of pair-wise interactions using the exact coordinates of C-atoms in a full graphite lattice, (ii) calculations using the DMM, RDM, and CMM for graphite, and (iii) calculations using the CMM of graphite alone. A summary of the result is given in Table IX.

1. Summation of pair-wise interaction energy calculations (see Appendix 1)

The basis vectors of the 3D hexagonal lattice of graphite are (refer to Figs. 3 and 24)

$$\bar{a}_1 = b\hat{x}, \quad \bar{a}_2 = b \left[\cos\left(\frac{\pi}{3}\right)\hat{x} + \sin\left(\frac{\pi}{3}\right)\hat{y} \right], \quad \text{and} \quad \bar{a}_3 = -c\hat{z}. \quad (3.F.1)$$

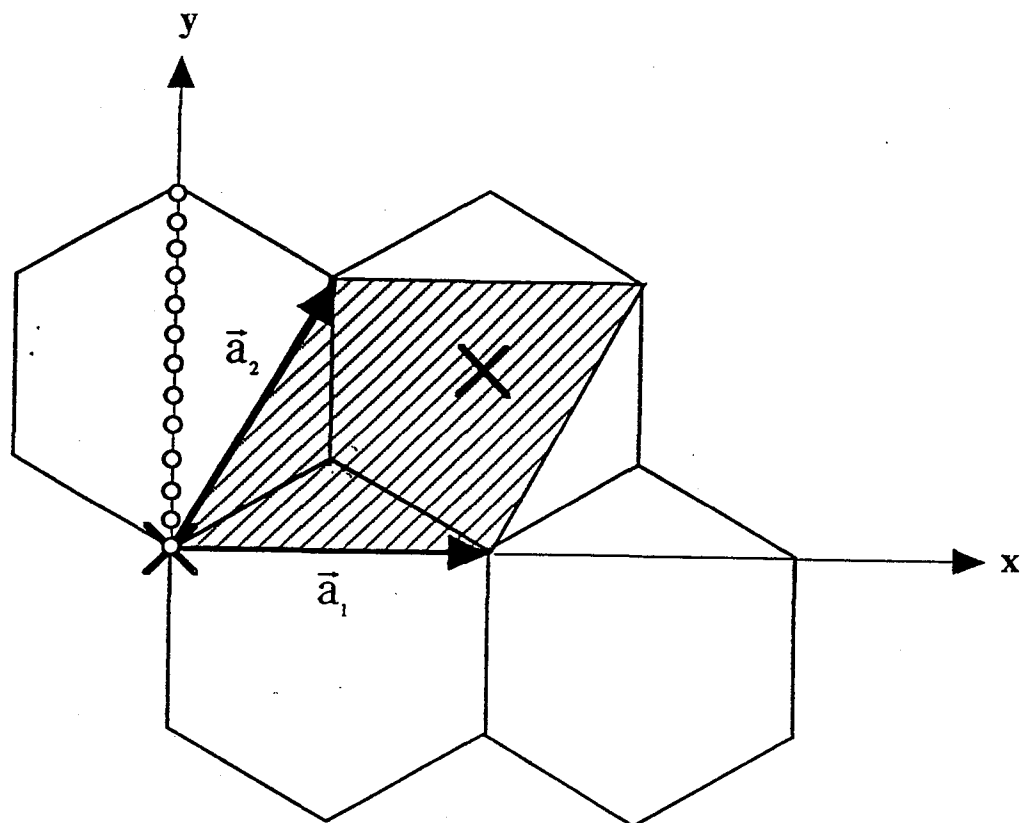
The coordinates of the four C-atoms in the graphite unit cell are

$$\bar{e}_1 = \bar{0}, \quad \bar{e}_2 = \frac{1}{3}(\bar{a}_1 + \bar{a}_2), \quad \bar{e}_3 = \frac{1}{2}\bar{a}_3, \quad \text{and} \quad \bar{e}_4 = \frac{2}{3}\bar{a}_1 + \frac{2}{3}\bar{a}_2 + \frac{1}{2}\bar{a}_3. \quad (3.F.2)$$

A summation of the exact pair-wise potentials for 33620 nearest C-atoms was performed for 78 positions, including z- variation of the central Kr atom (see Appendix 1 and Fig. 24) using the Lennard-Jones 6-12 potential given in the equation 3.F.1 for the Kr - graphite interaction energy. This number of C-atoms is large enough to obtain an accurate Kr-graphite interaction energy. The minimum Kr-graphite interaction energy for 74420 nearest C-atoms is different less than 0.001% from that for 33620

TABLE IX. Kr-graphite interaction energies determined by various methods.

Calculation Method	Extended calculation by Steele ³	Full pair-wise Lennard-Jones calculation	DMM, RDM, and CMM	CMM
Minimum Binding Energy (erg) x 10 ¹⁵	-203.82	-191.018	-180.747	-98.867
Ratio to Extended Calculation Result	--	0.937	0.887	0.461
Ratio to Full Pair-wise Calculation Result	1.067	--	0.944	0.518
Maximum Binding Energy (erg) x 10 ¹⁵	-191.38	-185.416	-173.009	--
Ratio to Extended Calculation Result	--	0.969	0.904	--
Ratio to Full Pair-wise Calculation Result	1.032	--	0.933	--
Corrugation (erg) x 10 ¹⁵	7.14	5.602	7.738	--
Ratio to Extended Calculation Result	--	0.784	1.084	--
Ratio to Full Pair-wise Calculation Result	1.276	--	1.381	--



○ : Position of the central Kr atom

FIG. 24. Coordinates of Kr-graphite interaction energy calculations. The graphite in-plane basis vectors \vec{a}_1 and \vec{a}_2 are shown. The unit cell is shaded. The dots indicate the positions of the central Kr atom for the calculations of Section 3.F.1. The X's indicate the positions of the central Kr atom for the calculations of Section 3.F.2.

nearest C-atoms. The horizontal variation of the central Kr atom were made along the y-axis from the origin. The spacing between two successive horizontal physisorption sites was $\frac{a}{12}$. The vertical increment for each particular horizontal physisorption site was 0.1Å upward from 3.1Å.

The minimum interaction energy was -192.018×10^{-15} erg/Kr atom and the maximum was -185.416×10^{-15} erg/Kr atom. The corrugation (the difference between minimum and maximum energies) was 5.602×10^{-15} erg/Kr atom. These calculated values are about 94%, 97%, and 78% of values obtained with Steele's extended interaction potential.³ The most favorable and the most unfavorable physisorption sites were the center of the hexagon and just above a C-atom, as expected.

2. Calculation of interaction energies using the DMM, RDM, and CMM

For these calculation, graphite was divided into the first layer (the basal plane of graphite) and bulk graphite in a manner similar to Fig. 19. Their separation was adjusted to $\frac{c}{2}$. The first layer was a combination of the DMM/RDM, and the CMM. The bulk graphite used only the CMM. The surface density of the first layer CMM was $\frac{c}{2}\rho_0$ and the density of the bulk CMM was ρ_0 , where ρ_0 is the average particle density of graphite (0.113 atoms/Å³). Calculations were done at only two sites (above the central carbon atom at the origin and above the center of the hexagon) as indicated in Fig. 24. For these two sites, there is no difference between the DMM and the RDM in the interaction energy calculation (recall the RDF for crystal is comprised of a series of peaks).

For calculation with the Kr atom above the central C-atom, up to sixth neighbors (31 C-atoms) were included in DMM/RDM. The crossover from the DMM/RDM to the CMM took place at $R = 5.1\text{Å}$, which was determined using equation 2.E.2 with $N = 31$. The calculated interaction energy, above the central carbon atom at the most

unfavorable physisorption site, was -173.043×10^{-15} erg/Kr atom, which is about 93% of the interaction energy calculated in Section 3.F.1 using the same Lennard-Jones 6-12 potential and summation of pair-wise interaction potentials.

Now, consider the interaction energy when the central Kr atom is above the center of a hexagon, the most favorable physisorption site on the basal plane of graphite. The calculation method is exactly same as before, but the DMM/RDM of the first layer included C-atoms up to only the third nearest neighbors from the center of the hexagon ($N = 24$). The crossover from the DMM/RDM to the CMM took place at $R = 4.488 \text{ \AA}$. The calculated Kr - graphite interaction energy above the center of the hexagon was -180.747×10^{-15} erg/Kr atom, which is about 94% of the interaction energy calculated in Section 3.F.1 at the most favorable physisorption site.

3. Calculation of interaction energy with CMM (refer to Appendix 4 in detail)

In this calculation, graphite was treated as a homogeneous and isotropic medium with a constant particle density ρ_0 , the average particle density of graphite. The calculation was independent of the lateral position of the Kr adatom. The Kr - graphite interaction energy using the CMM alone was -98.867×10^{-15} erg/Kr atom. This corresponds 52% of the minimum interaction energy of the calculation in Section 3.F.1. Therefore, the interaction energy calculation using the CMM alone is not sufficient. Besides, this method cannot determine the corrugation of graphite.

4. Summary

The results of the Kr-graphite calculation are summarized in Table IX. Based on these calculation, we conclude that (i) $\phi_{\text{Kr-C}}$ given in the equation is sufficiently reliable for our purpose, (ii) the interaction energy calculation using the DMM, RDM, and CMM provides reasonably good results, and (iii) the interaction energy calculation using the CMM alone is not adequate.

G. Interaction energy calculation results on g-C

1. Kr - Kr interaction energy on g-C (refer to Appendix 5 in detail)

In this section we consider the structure of Kr atoms adsorbed on a flat uniform density substrate, that is a substrate with no corrugation. (Discussion of the effects of corrugation on the Kr adlayer structure are deferred to Chapter 4.) For such a substrate, the most stable structure of the Kr adlayer is a 2D triangular lattice with a lattice constant of 4 Å, similar to the incommensurate structure depicted in Fig. 1. Here, the nearest neighbor distance 4 Å is very close to the radial distance where the pair-wise Kr - Kr interaction potential given by equation 3.D.3 has its minimum value at $r_{\min}=4.04$ Å. The attractive position of the interaction energy is maximized by an adlayer structure with a maximum number of nearest neighbors at a distance close to r_{\min} . For a 2D structure, the maximum number of such nearest neighbors is six in a triangular lattice.

We can calculate the interaction energy for one Kr adatom with the other Kr atoms in the 2D adlayer using a simple pair-wise summation, as was done in Section F.1 for the Kr - graphite lattice interaction energy. The summation included pair-wise interactions for nearest neighbors, which is quite sufficient for a potential falling off as r^{-6} . The basis vectors of the 2D triangular lattice are

$$\bar{a}_1 = b\hat{x}, \quad \bar{a}_2 = b\left[\cos\left(\frac{\pi}{3}\right)\hat{x} + \sin\left(\frac{\pi}{3}\right)\hat{y}\right] \quad (3.G.1)$$

with only one atom per primitive unit cell, and where b is the nearest neighbor distance. The results of these calculations, as a function of nearest neighbor distance b are listed in Table X and plotted in Fig. 25.

2. Kr-g-C interaction energy calculation result

Using the Kr - g-C calculation methods described in Section E, interaction energy calculations were performed for every element (three ring cluster) of the DMM ensemble. As an example, Appendix 4 shows the calculation along the symmetric line

of the 5-membered ring of the 567-5 three ring cluster (refer to Fig. 23).

Mesh plots of the interaction energy projected on the x-y plane for each of the fifteen types of the three ring clusters are shown in Fig. 26(a - o). The height variations of C-atoms of the three clusters along the z-axis are scaled appropriately.

Tables XI (a) and (b) show the maximum and minimum binding energies, and the corrugation for both non-flat and flat three ring clusters. The values for the non-flat three ring clusters are the average values of the convex and concave three ring clusters. Note that the corrugations of the non-flat structures are as much as a factor of 6 larger than the corrugations of the flat structures. Table XII shows the contribution of each type of ring found in the elements of the DMM ensemble to the total weighted average minimum and maximum interaction energies and corrugation of Kr on g-C. For non-flat three ring structures, the contributions are average values of the convex and concave structures. The method used to calculate these weighting factors (based on ring statistics and areas of the rings) is detailed in Appendix 2 and are tabulated in Tables XVII and XVIII. The total weighted average values of the minimum and maximum interaction energies and corrugation for Kr on g-C are also listed at the bottom of Table XII. Table XIII shows the coordinates of the central Kr atom at the physisorption sites corresponding to the minimum and maximum interaction energies. In this table, the direction of x-axis for each cases is listed. By using the coordinates of C-atoms in Table IV and appropriate rotation about z-axis, the position of the central Kr atom relative to the C-atoms of the three clusters can be determined [also, refer to Fig. 26(a - o)]. Table XIV shows the weighted average binding energy of Kr on each DMM ensemble element and the weighted average binding energy of Kr on g-C. In Table XIV, the average of the binding energy surface of each mesh plot in Fig. 26(a - o) was used as the weighted average binding energy of each three ring cluster. Then, by using the probability distribution of the three ring clusters, the weighted average binding

Table X. Interaction energy of a single Kr atom with a 2D triangular lattice of Kr atoms as a function of the nearest neighbor distance b .

b (Å)	Interaction Energy (erg) $\times 10^{14}$	b (Å)	Interaction Energy (erg) $\times 10^{14}$	b (Å)	Interaction Energy (erg) $\times 10^{14}$
3.1	193.745	5.1	-6.580	7.1	-1.007
3.2	111.193	5.2	-5.941	7.2	-0.927
3.3	59.752	5.3	-5.366	7.3	-0.854
3.4	27.848	5.4	-4.849	7.4	-0.788
3.5	8.284	5.5	-4.384	7.5	-0.728
3.6	-3.455	5.6	-3.967	7.6	-0.673
3.7	-10.231	5.7	-3.593	7.7	-0.623
3.8	-13.866	5.8	-3.257	7.8	-0.577
3.9	-15.528	5.9	-2.956	7.9	-0.535
4.0	-15.969	6.0	-2.686	8.0	-0.496
4.1	-15.673	6.1	-2.443	8.1	-0.461
4.2	-14.952	6.2	-2.224	8.2	-0.428
4.3	-14.004	6.3	-2.027	8.3	-0.398
4.4	-12.955	6.4	-1.850	8.4	-0.371
4.5	-11.884	6.5	-1.691	8.5	-0.346
4.6	-10.838	6.6	-1.546	8.6	-0.322
4.7	-9.845	6.7	-1.416	8.7	-0.301
4.8	-8.918	6.8	-1.298	8.8	-0.281
4.9	-8.065	6.9	-1.191	8.9	-0.263
5.0	-7.287	7.0	-1.095	9.0	-0.246

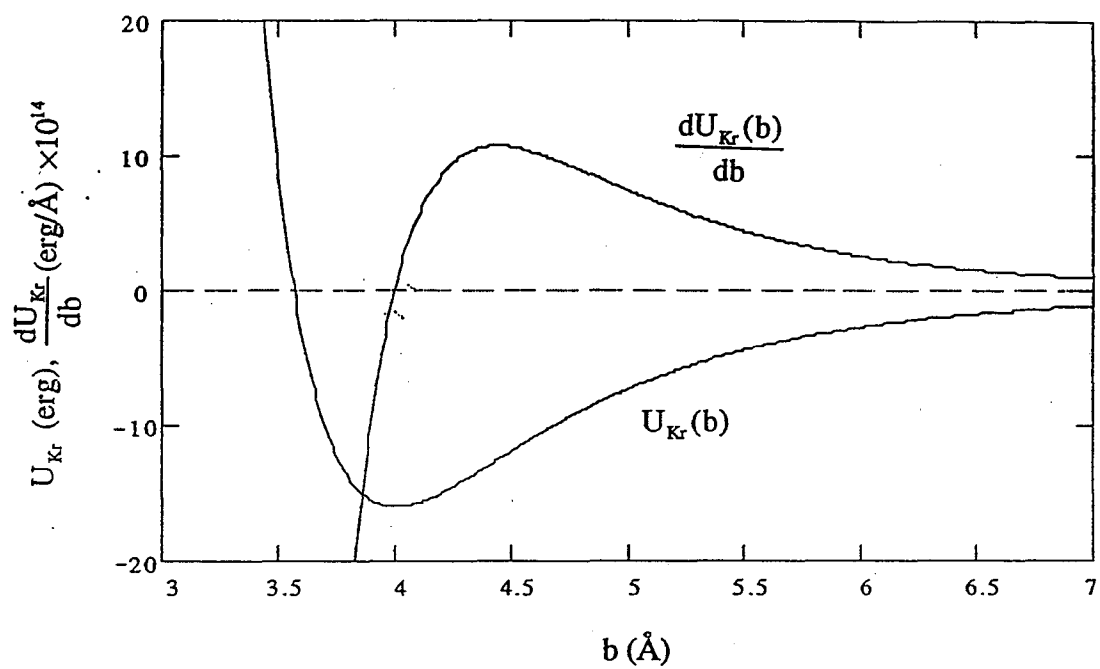


FIG. 25. Graph of the interaction energy of a single Kr atom with a 2D triangular lattice of Kr atoms as a function of the nearest neighbor distance b .

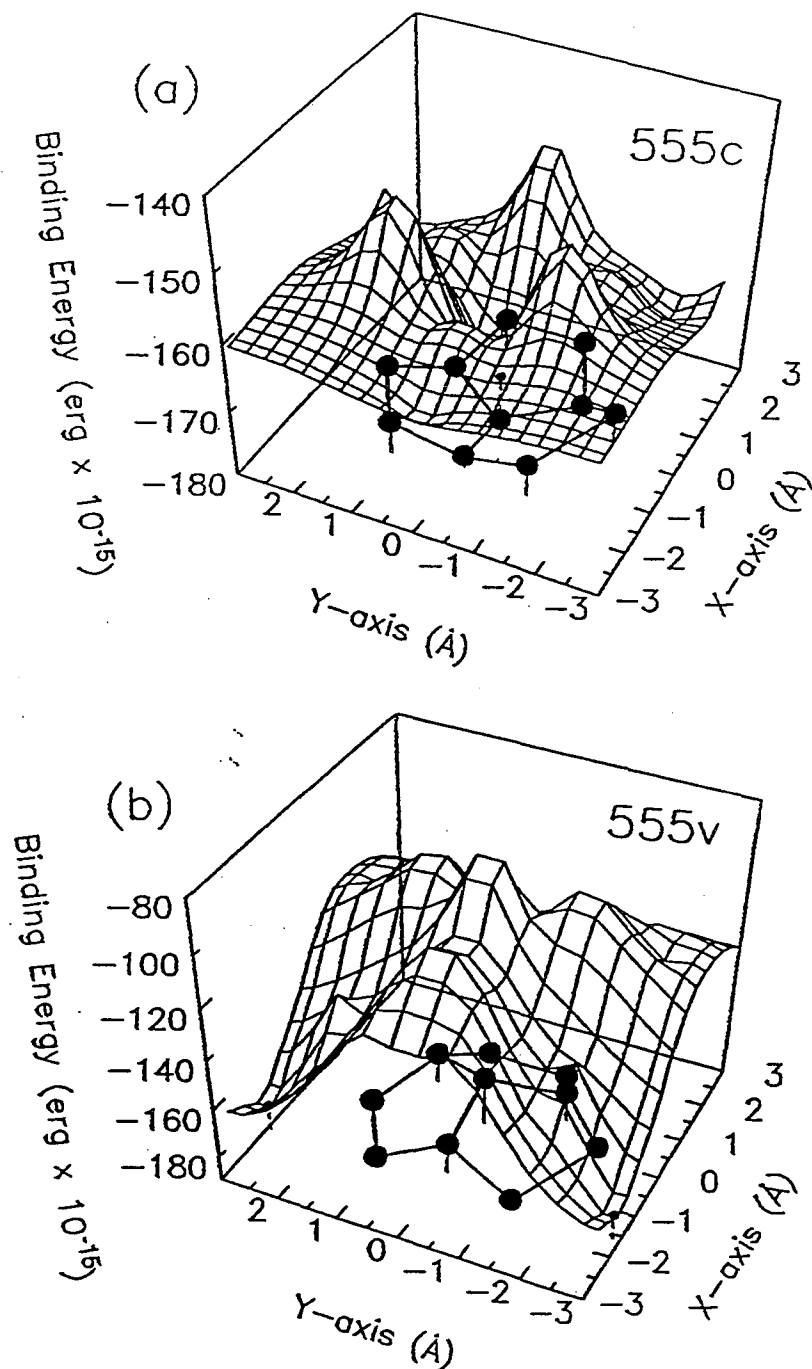


Fig. 26. Mesh plots of the interaction energies of three ring clusters. The notation following the three ring cluster notation indicates convex and concave structure for non-flat three ring clusters; "c" indicates concave and "v" denotes convex.

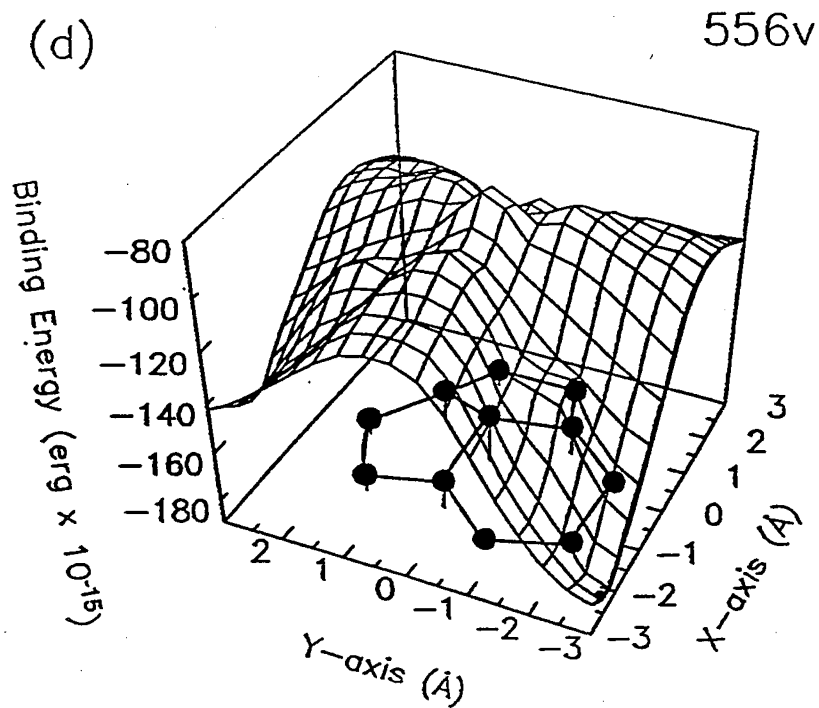
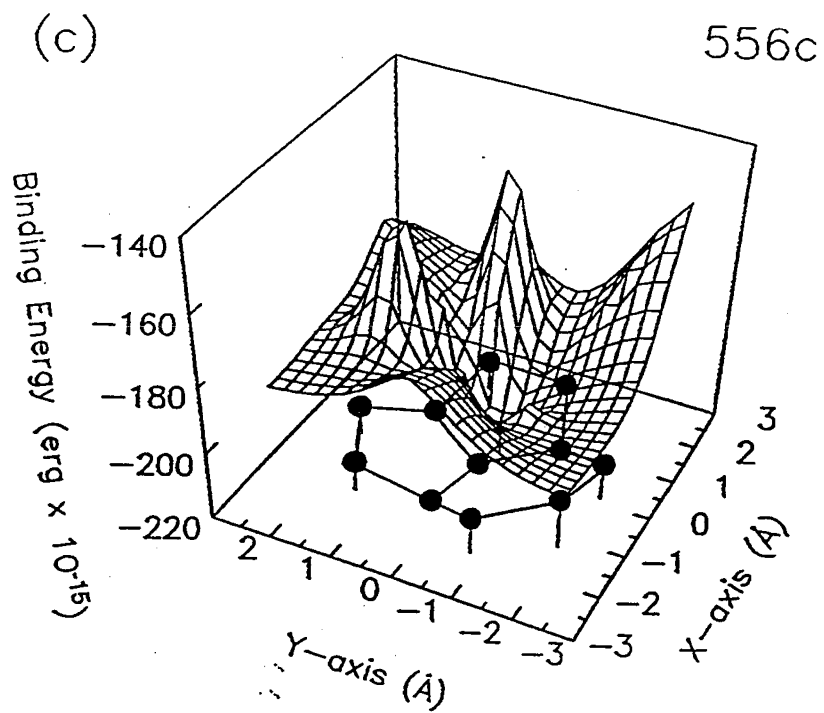


Fig.26. Continued.

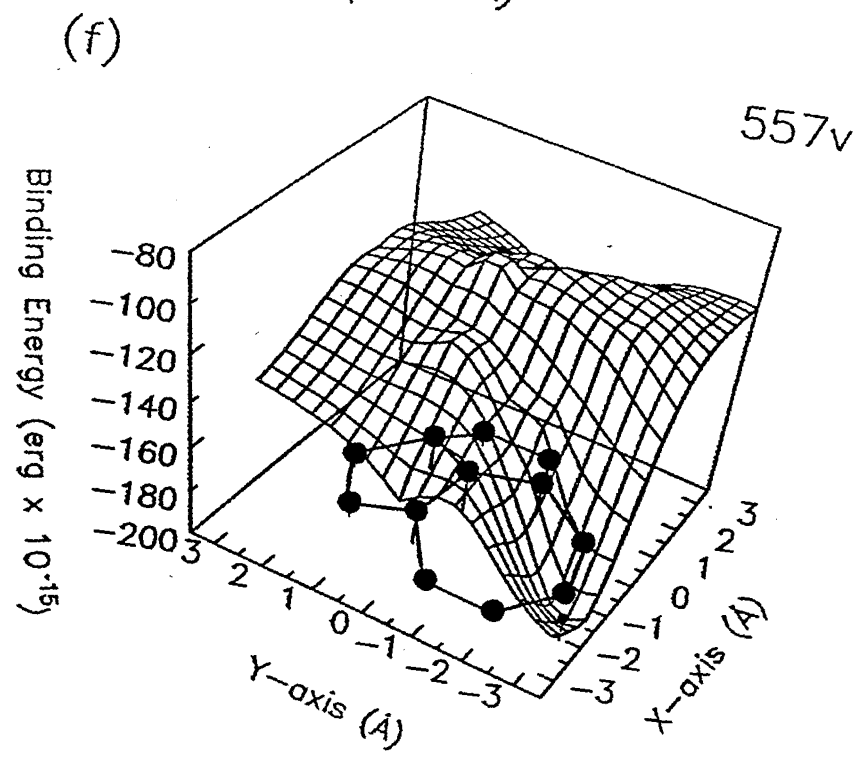
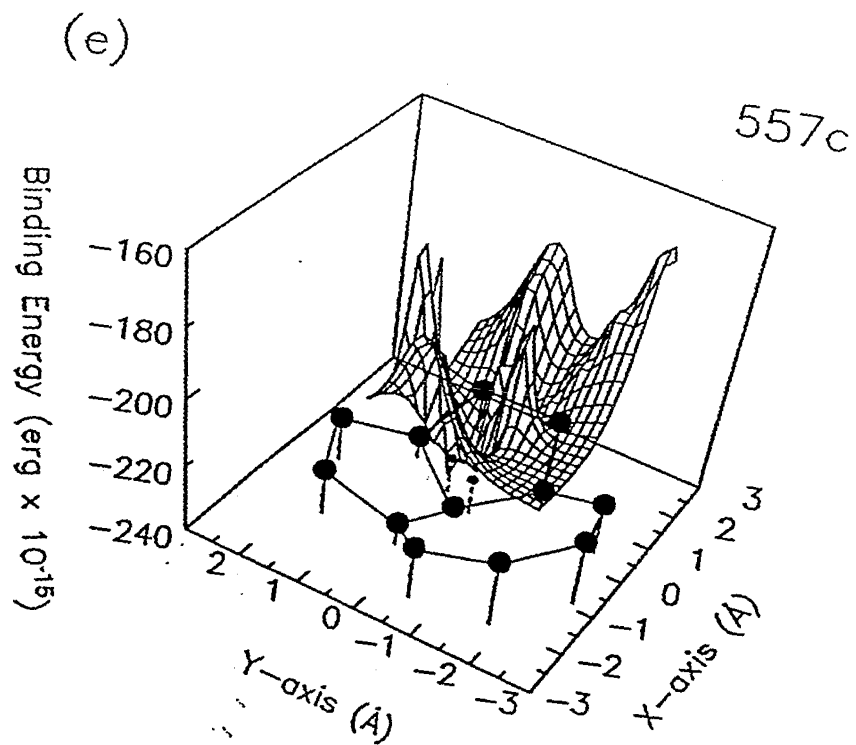


Fig.26. Continued.

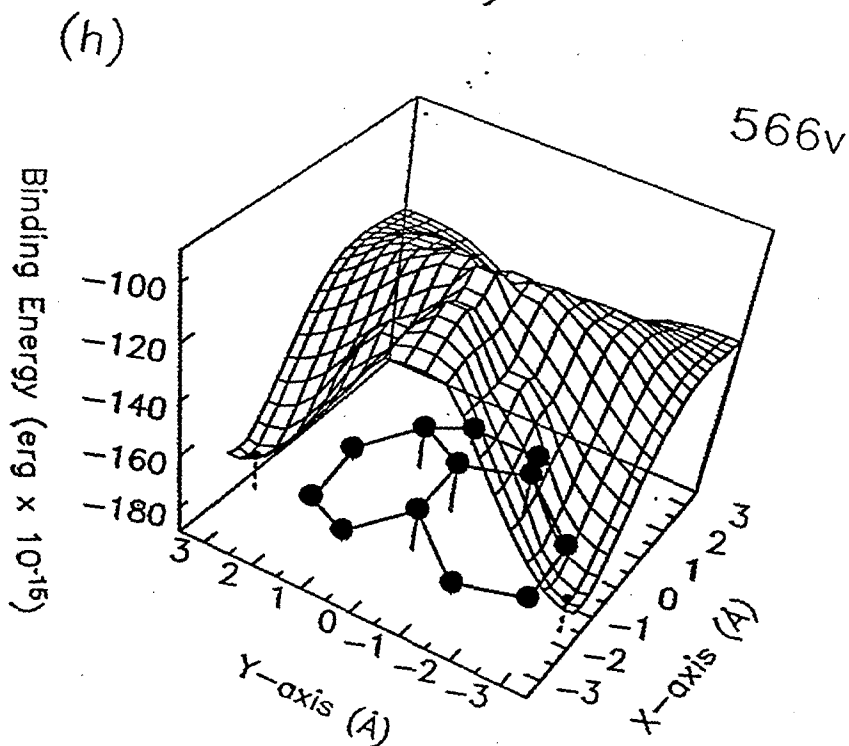
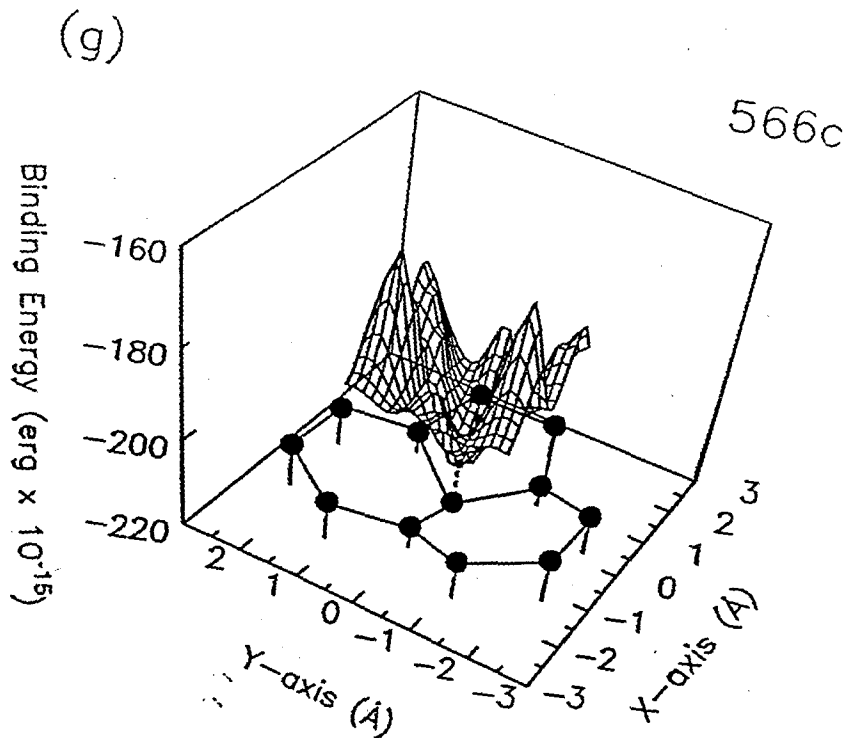


Fig.26. Continued.

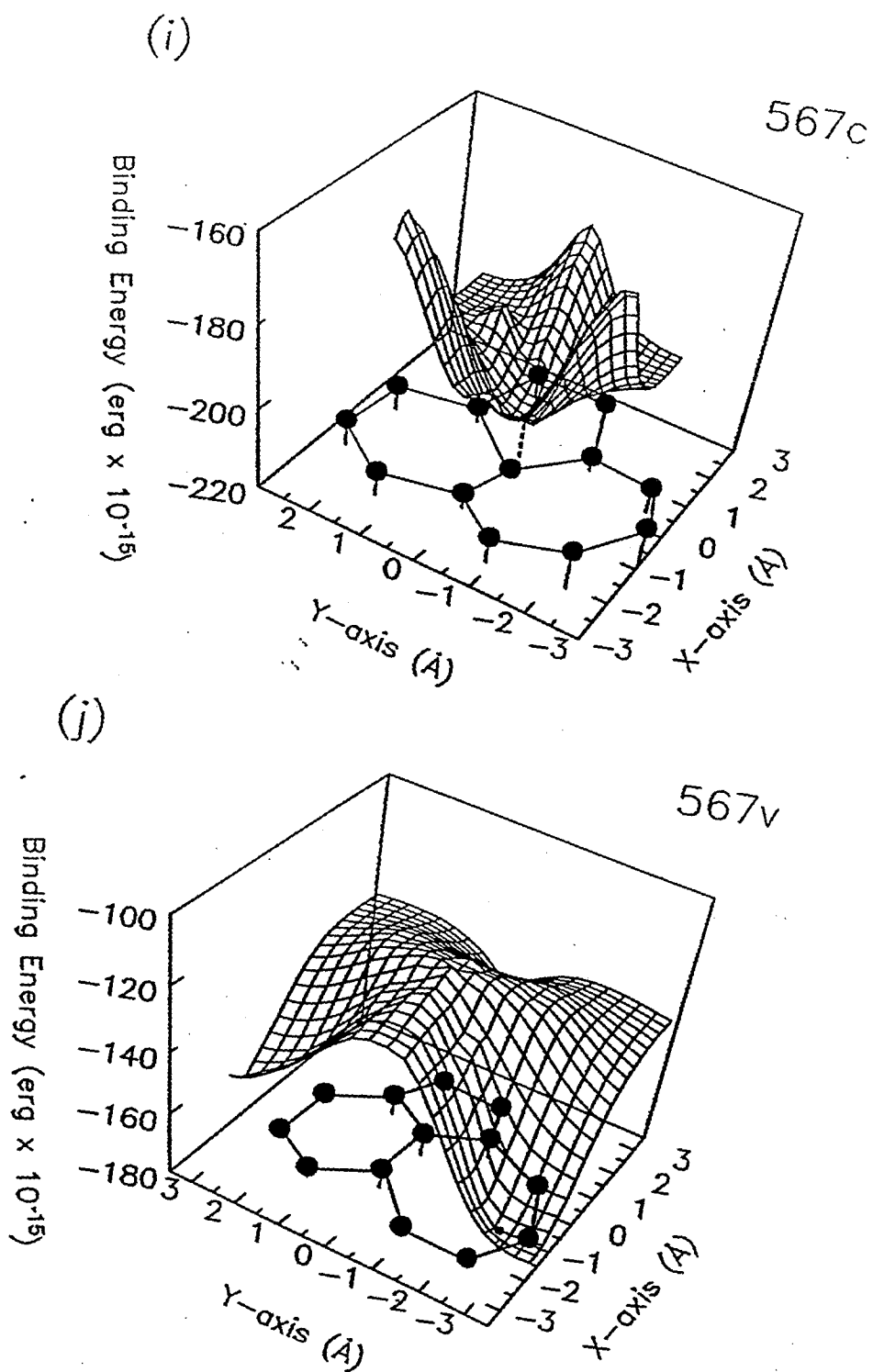


Fig.26. Continued.

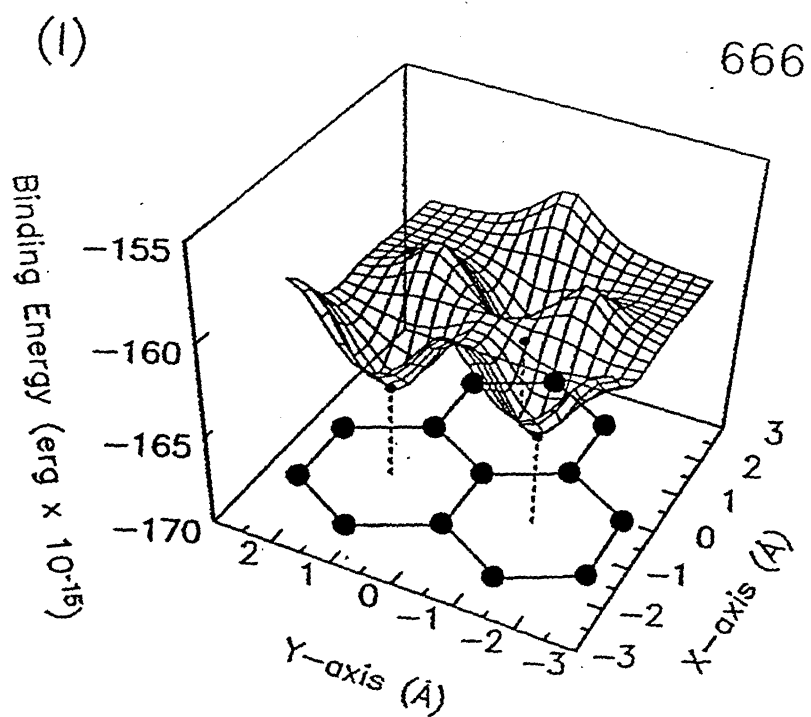
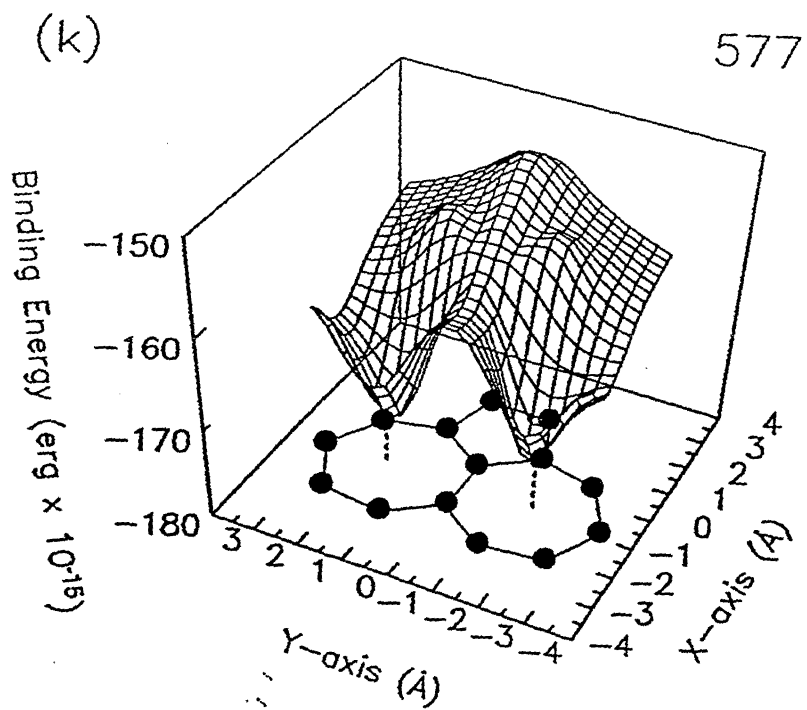


Fig.26. Continued.

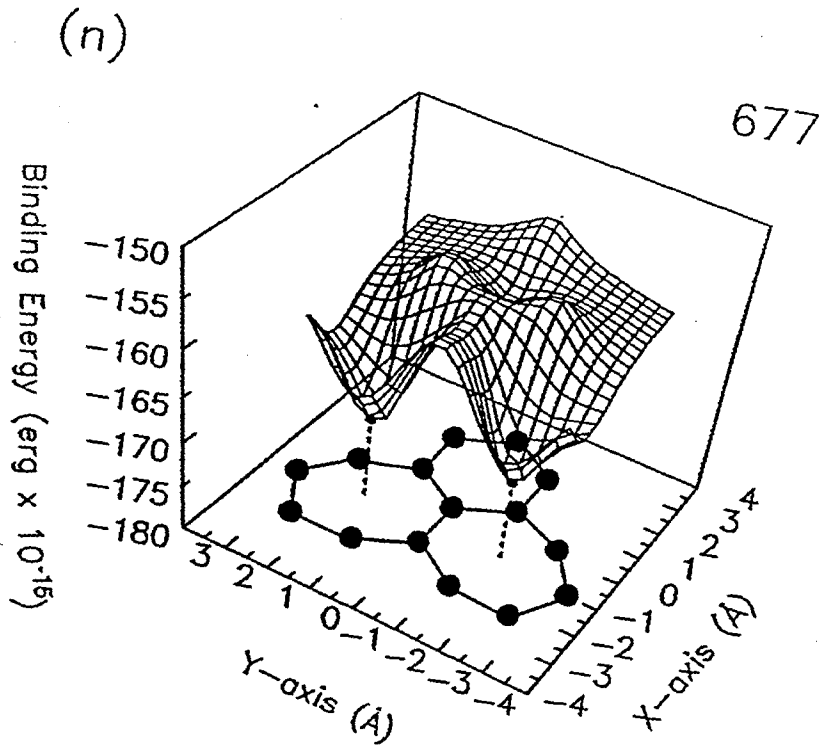
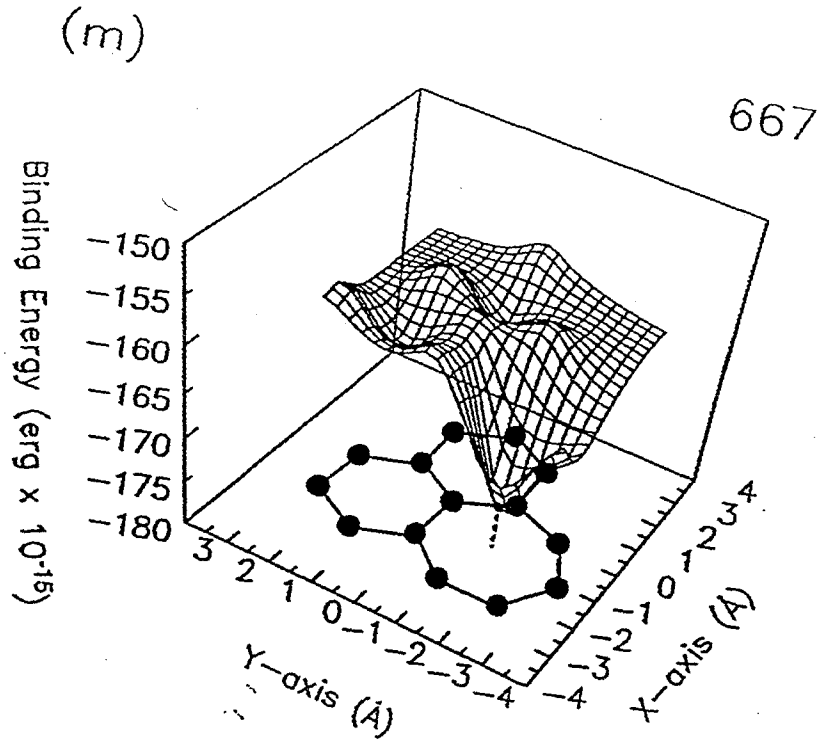


Fig.26. Continued.

777

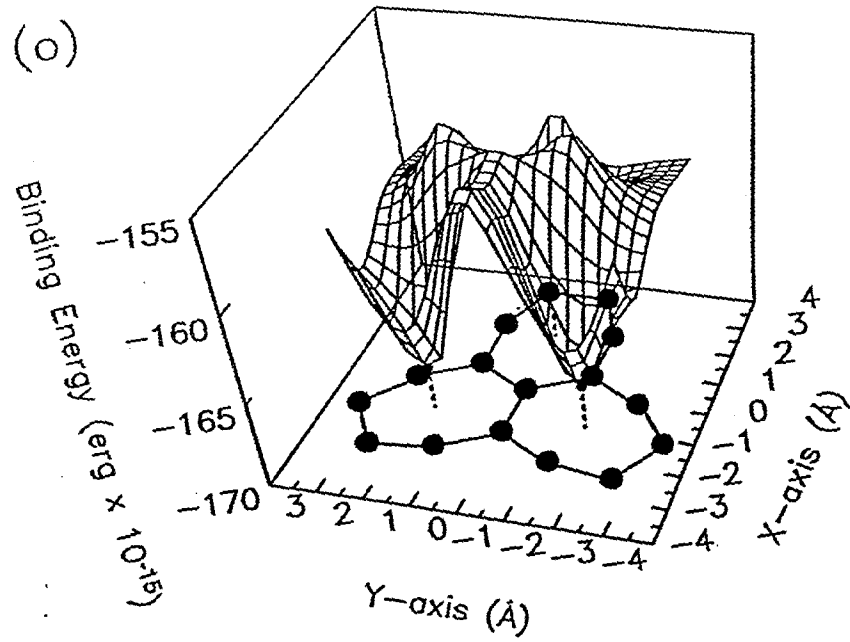


Fig.26. Continued.

TABLE XI. Minimum and maximum binding energies and corrugations for three ring clusters. U_{\min} and U_{\max} indicate minimum and maximum binding energy per Kr atom, respectively.

(a) Non-flat three ring clusters. The values are the average values of the convex and concave three ring clusters.

Combination of ring clusters	U_{\min} (erg) x 10^{15}	U_{\max} (erg) x 10^{15}	Corrugation (erg) x 10^{15}
555-5	-175.541	-114.876	60.666
556-5	-190.254	-115.271	74.984
556-6	-197.290	-115.880	81.410
557-5	-185.959	-121.810	57.184
557-7	-208.445	-122.973	85.473
566-5	-185.180	-140.205	44.975
566-6	-193.555	-131.684	61.872
567-5	-174.197	-144.324	29.873
567-6	-182.854	-140.036	42.818
567-7	-189.349	-136.427	52.922
Weighted Average	-188.960	-133.758	55.202

(b) Flat three ring clusters.

Combination of ring clusters	U_{\min} (erg) $\times 10^{15}$	U_{\max} (erg) $\times 10^{15}$	Corrugation (erg) $\times 10^{15}$
577-5	-157.450	-150.671	6.779
577-7	-174.133	-154.865	19.268
666-6	-164.876	-158.915	5.961
667-6	-162.728	-157.172	5.556
667-7	-175.059	-158.878	16.181
677-6	-159.474	-153.945	5.529
677-7	-170.540	-155.561	14.979
777-7	-167.503	-156.240	11.263
Weighted Average	-166.502	-157.617	8.887

energy of Kr on g-C was calculated.

The contribution of the DMM to the total binding energy of Kr on g-C is broadly 30% ~ 50% and that of the RDM and CMM combination is 50% ~ 70%. In the DMM, the contribution of the C-atom at the center of the DMM to the total binding energy of Kr on g-C is about 3% to 7%. The Kr - g-C calculation in Appendix 6 shows that the contributions of the central C-atom, the DMM and the RDM and CMM combination are 5.4%, 35.8%, and 64.2%, respectively.

Table XII. The contribution of each three ring cluster to the total weighted average minimum and maximum interaction energies and corrugations.

Combination of ring clusters	Contribution to U_{\min}	Contribution to U_{\max}	Contribution to Corrugation
555-5	0.9	0.8	1.8
556-5	5.2	3.9	11.3
555-6	3.4	2.4	7.7
557-5	1.6	1.4	2.7
557-7	1.4	1.0	3.1
566-5	6.5	6.0	8.7
566-6	17.2	14.3	30.3
567-5	3.9	3.9	3.7
567-6	5.2	4.8	6.6
567-7	6.4	5.6	9.9
577-5	0.6	0.7	0.1
577-7	1.9	2.0	1.1
666-6	18.9	22.3	3.8
667-6	11.9	14	2.2
667-7	7.7	8.5	3.9
677-6	1.9	2.2	0.4
677-7	4.8	5.3	2.3
777-7	0.8	0.9	0.3
Total Weighted Average	U_{\min} (erg) x 10^{15}	U_{\max} (erg) x 10^{15}	Corrugation (erg) x 10^{15}
	-177.385	-145.199	32.186

TABLE XIII. Coordinates of the central Kr atom at the physisorption sites corresponding to the minimum and maximum interaction energies. The notation following the coordinates of the Kr atom indicates the direction of x-axis; “- s” indicates the direction of the symmetry line of the corresponding ring lying in xz- plane and “- i&j” means the intraplanar sp^2 bond branch between i- and j-membered rings lying in the xz-plane.

(a) Convex three ring clusters.

Combination of three ring clusters	Coordinates of Kr atom	Coordinates of Kr atom
	for minimum binding energies	for maximum binding energies
555-5	(3.352, 0, 3.4) - s	(0, 0, 4.8) - s
556-5	(3.873, 0, 3.6) - s	(0, 0, 5.2) - s
556-6	((3.624, 0, 3.5) - s	(0, 0, 5.2) - s
557-5	(3.571, 0, 3.9) - s	(0, 0, 5.2) - s
557-7	(3.708, 0, 3.5) - s	(0, 0, 5.2) - s
566-5	(3.469, 0, 3.6) - s	(0, 0, 4.7) - s
566-6	(3.624, 0, 3.5) - s	(0, 0, 4.7) - s
567-5	(3.018, 0, 3.8) - s	(0, 0, 4.3) - s
567-6	(3.527, 0, 3.6) - s	(0, 0, 4.3) - s
567-7	(2.97, 0, 3.6) - s	(0, 0, 4.3) - s

(b) Concave three ring clusters.

Combination of three ring clusters	Coordinates of Kr atom for minimum binding energies	Coordinates of Kr atom for maximum binding energies
555-5	(0, 0, 3.2) - s	(1.586, 0, 3.5) - 5 & 5
556-5	(0.215, 0, 2.6) - 5 & 5	(-1.172, 0, 3.2) - 5 & 5
556-6	(-0.361, 0, 2.6) - s	(-3.026, 0, 3.1) - s
557-5	(0.279, 0, 2.4) - 5 & 5	(-0.81, 0, 2.9) - 5 & 5
557-7	(-0.222, 0, 2.4) - s	(3, 0, -2.51) - s
566-5	(0.066, 0, 2.8) - s	(-1.295, 0, 3) - s
566-6	(-0.085, 0, 2.8) - 6&6	(1.198, 0, 3.2) - s
567-5	(-0.153, 0, 2.9) - 5&6	(1.75, 0, 3.1) - s
567-6	(0.323, 0, 2.9) - 6&7	(2.027, 0, 3.3) - s
567-7	(0.202, 0, 2.9) - s	(2.33, 0, 3.4) - s

(c) Flat three ring clusters.

Combination of three ring clusters	Coordinates of Kr atom for minimum binding energies	Coordinates of Kr atom for maximum binding energies
577-5	(0, 0, 3.5) - s	(2.016, 0, 3.5) - s
577-7	(1.192, 0, 3.4) - s	(0, 0, 3.5) - s
666-6	(1.421, 0, 3.5) - s	(2.842, 0, 3.5) - s
667-6	(1.421, 0, 3.5) - s	(1.421, 0, 3.5) - 6&6
667-7	(1.639, 0, 3.4) - s	(0, 0, 3.5) - 6&7
677-6	(1.421, 0, 3.5) - s	(2.842, 0, 3.5) - s
677-7	(1.192, 0, 3.4) - s	(0, 0, 3.5) - 6&7
777-7	(1.192, 0, 3.5) - s	(1.421, 0, 3.5) - 7&7

TABLE XIV. The weighted average binding energy of Kr on each DMM ensemble element and the weighted average binding energy of Kr on g-C. The notations following the three ring cluster notations. ("c" and "-v") indicate concave and convex three ring clusters, respectively.

Three Ring Cluster	Weighted Average Binding Energy erg x 10 ¹⁵	Three Ring Cluster	Weighted Average Binding Energy erg x 10 ¹⁵
555-c	-159 ± 3.69	567-c	-189 ± 9.27
555-v	-139 ± 20.4	567-v	-137 ± 13.2
556-c	-181 ± 10.5	577	-161 ± 5.58
556-v	-122 ± 22	666	-162 ± 1.12
557-c	-199 ± 12.9	667	-162 ± 3.4
557-v	-119 ± 23.1	677	-160 ± 3.58
566-c	-191 ± 9.16	777	-161 ± 2.49
566-v	-130 ± 17.9		
Weighted Average Binding Energy of Kr on g-C erg x 10 ¹⁵		-160.605 ± 7.900	

CHAPTER 4

DISCUSSION: Kr ON GRAPHITIC AMORPHOUS CARBON

Let us consider separately (i) the results of the Kr - g-C interaction energy calculation using our structural model of g-C, (ii) the prediction of the structures of Kr adlayers on g-C, and (iii) the limitations of our model of g-C.

A. Discussion about Kr-g-C interaction energy calculation

The total weighted average minimum binding energy of Kr on a g-C substrate is -177.39×10^{-15} erg/Kr atom. This is 93% of the minimum binding energy of Kr on the basal plane of graphite, -191.38×10^{-15} erg/Kr atom using the same Lennard-Jones 6-12 interaction potentials. The total weighted average maximum binding energy of Kr on g-C, -145.20×10^{-15} erg/Kr atom, is 78% of the maximum binding energy of Kr on the basal plane of graphite. Refer to Tables IX and XI for a comparison of these values. Therefore, we can expect that Kr atoms will physisorb on g-C, since binding energies of Kr on g-C are comparable (though perhaps somewhat less than) on average than the binding energies of Kr on graphite. Also, there are many dented parts (favorable physisorption sites) on a g-C substrate. These suggest physisorption of Kr on g-C will occur over a similar temperature range as for Kr on graphite (refer to the phase diagram in Fig. 2).

The corrugation of Kr on g-C is significantly larger than that of Kr on graphite. Based on the values in Table XI, its corrugation is about 6 times greater than that of Kr on the basal plane of graphite. We conclude that the wrinkling of g-C surface is primarily responsible for this great increase in corrugation. Three facts point to this conclusion: (i) the large contribution of non-flat (convex and concave) three ring clusters to the total weighted average corrugation, (ii) the relation between corrugations of rings in convex three ring clusters and their ring angles [defined in Fig. 27(a)], and (iii) the

relation between corrugations of rings in concave three ring clusters and their depths [defined in Fig. 27(b)].

First, consider the overwhelming contribution to the weighted average corrugation from the non-flat three ring clusters. About 86% of the total weighted average corrugation of the g-C substrate comes from non-flat three ring clusters. In fact, only 6 of the 18 types of rings considered in three ring clusters (556-5, 556-6, 566-5, 566-6, 567-6 and 567-7) contribute 75% of the weight to the weighted average corrugation. However, all of the non-flat three ring clusters account for only 49% of the three ring cluster probability distribution; the six non-flat three ring clusters with the largest contribution account for only 41% of the probability distribution. By contrast, the contributions of non-flat three ring clusters to the total weighted average minimum and maximum binding energies (52% and 44%, respectively) are reasonably consistent with their probability distributions. Large corrugation is a specific characteristic of the non-flat three ring clusters. Based on this, we can assert that the wrinkling of substrate plays a dominating role in its corrugation.

The ring angle, defined for convex three ring clusters in Fig. 27(a), is a measure of how much the substrate is wrinkled. Table XV(a) lists the ring angle for each convex three ring cluster. Fig. 28(a) shows the relation between the ring angles and the corrugations for 5-, 6-, and 7-membered rings in convex three ring clusters separately. From Fig. 28(a), we can conclude that the corrugation is approximately linearly proportional to the convex three ring cluster ring angle. Table XVI(a) lists their correlations.⁴⁵

Note that the slopes of these three curves increase with increasing number of C-atoms in the ring. We can obtain a universal curve [Fig. 29(a)] by plotting ring angle versus corrugation energy per ring atom. The correlation coefficient for Fig. 29(a) (0.985) is significantly greater than the correlation coefficient for corrugation versus

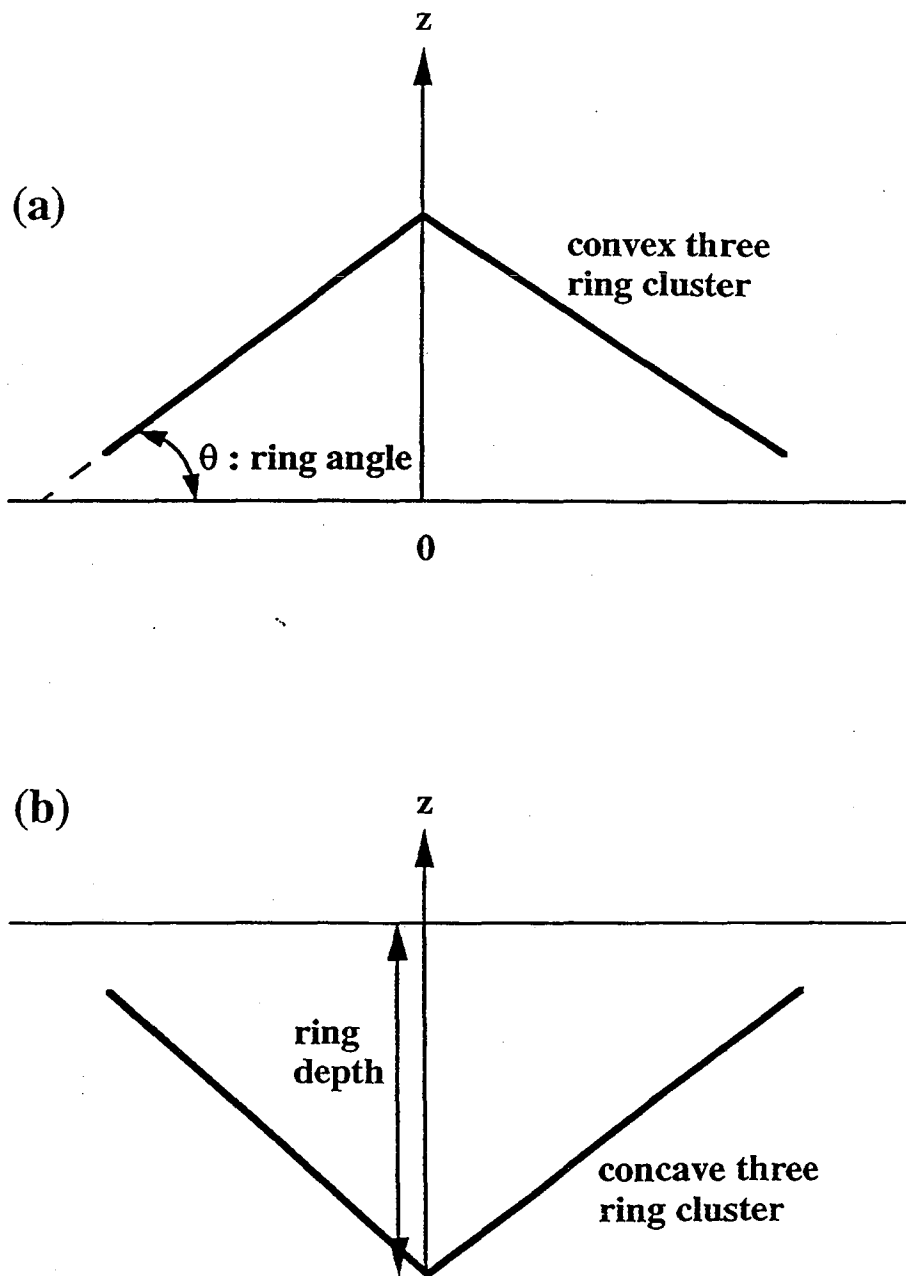


FIG. 27. (a) Definition of ring angle in a convex three ring cluster and (b) definition of ring depth in a concave three ring cluster.

TABLE XV. (a) Ring angle of each convex ring cluster.

Convex Ring Cluster	Ring Angle (°)	Convex Ring Cluster	Ring Angle (°)
555-5	20.848	566-5	11.604
556-5	16.676	566-6	11.605
556-6	16.677	567-5	6.096
557-5	13.089	567-6	6.097
557-7	13.09	567-7	6.097

(b) Ring depth of each concave ring cluster.

Concave Ring Cluster	Ring depth (Å)	Concave Ring Cluster	Ring depth (Å)
555-5	0.378	566-5	0.471
556-5	0.761	566-6	0.471
556-6	0.761	567-5	0.358
557-5	0.819	567-6	0.358
557-7	0.819	567-7	0.358

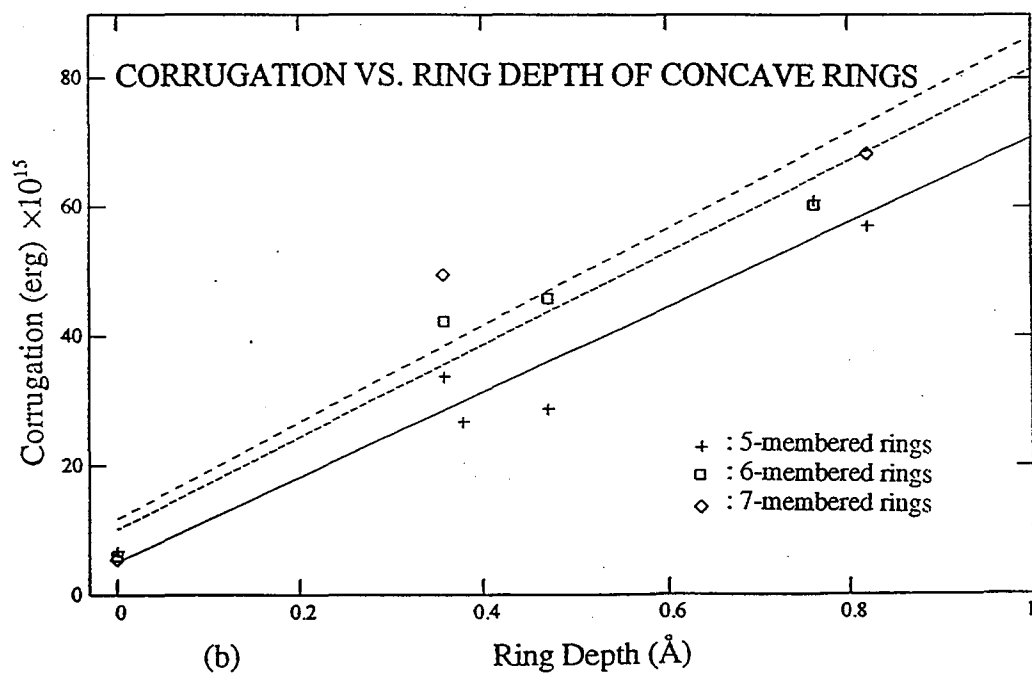
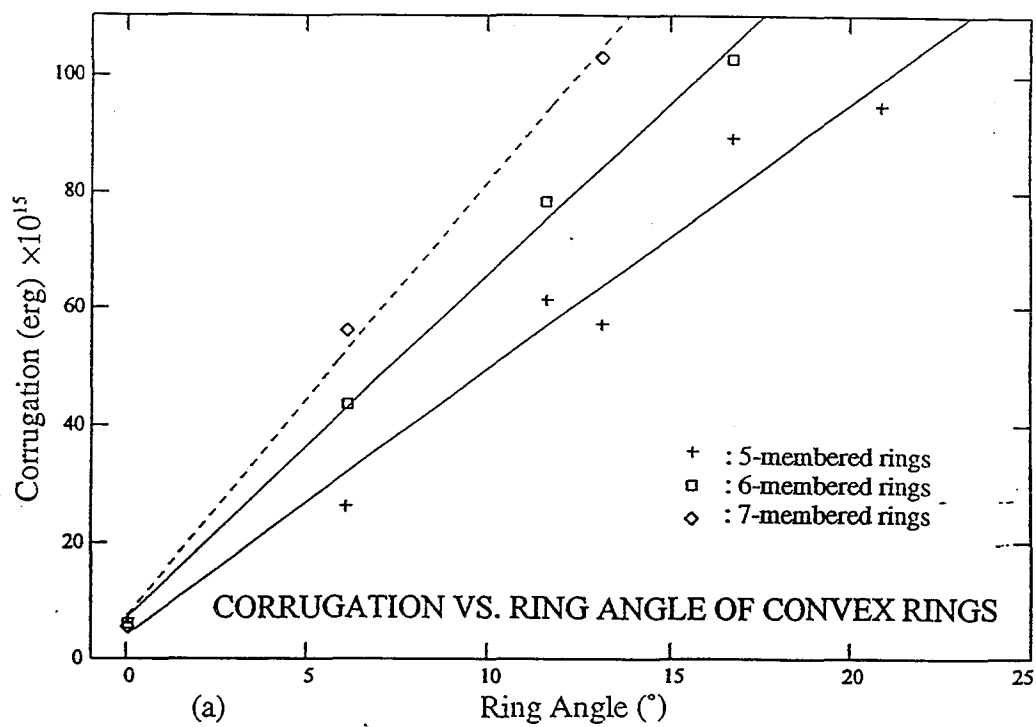


FIG. 28. (a) The corrugation of Kr on g-C versus the convex ring cluster angle, and (b) the corrugation of Kr on g-C versus concave ring cluster depth.

TABLE XVI. (a) The relation between corrugation and ring angle for convex three ring clusters.

	5-membered Rings	6-membered Rings	7-membered Rings
Slope of the Graph of Corrugation vs. Ring Angles (erg/degree $\times 10^{15}$)	4.542	5.86	7.409
Correlation Coefficient ⁶⁶	0.983	0.999	0.998

(b) The relation between corrugation and ring depth for concave three ring clusters.

	5-membered Rings	6-membered Rings	7-membered Rings
Slope of the Graph of Corrugation vs. Ring Depth (erg/Å $\times 10^{15}$)	65.651	71.276	74.733
Correlation Coefficient ⁶⁶	0.968	0.974	0.954

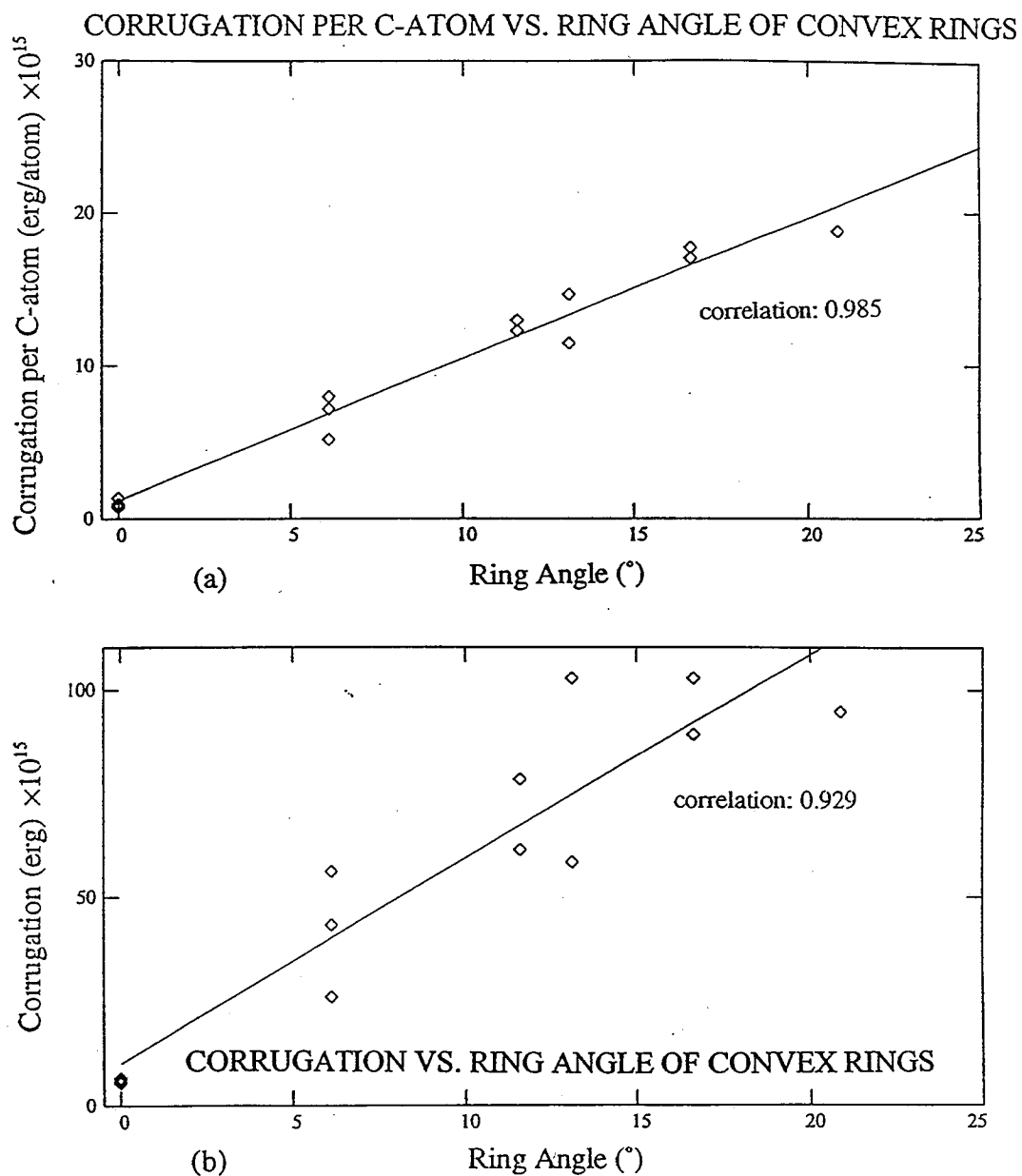


FIG. 29. (a) The universal relation between corrugation per C-atom of Kr on g-C and the convex ring cluster angle, (b) the universal relation between corrugation of Kr on g-C and the convex ring cluster angle, (c) the universal relation between corrugation of Kr on g-C and concave ring cluster depth, and (d) the universal relation between corrugation per C-atom of Kr on g-C and concave ring cluster depth.

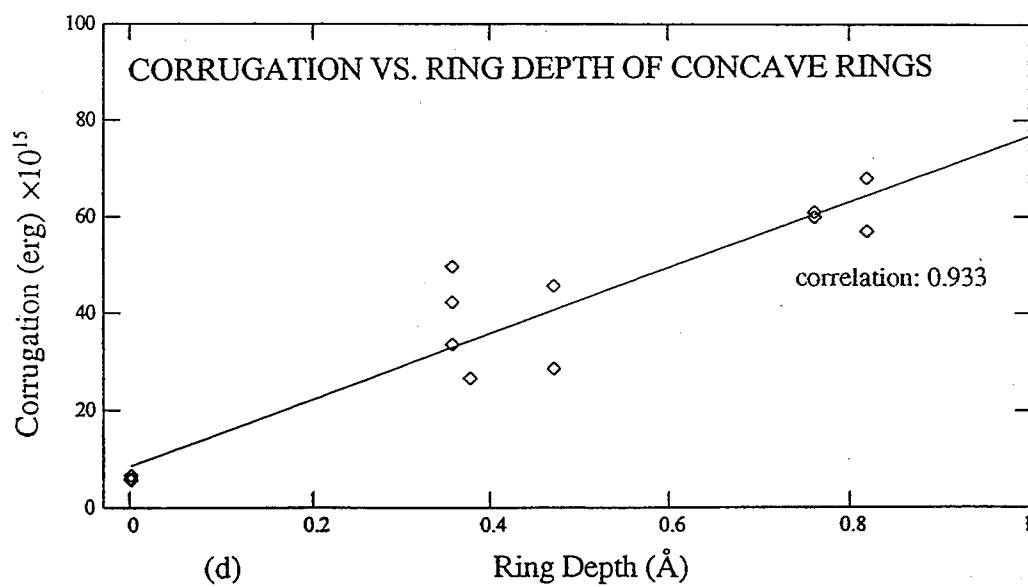
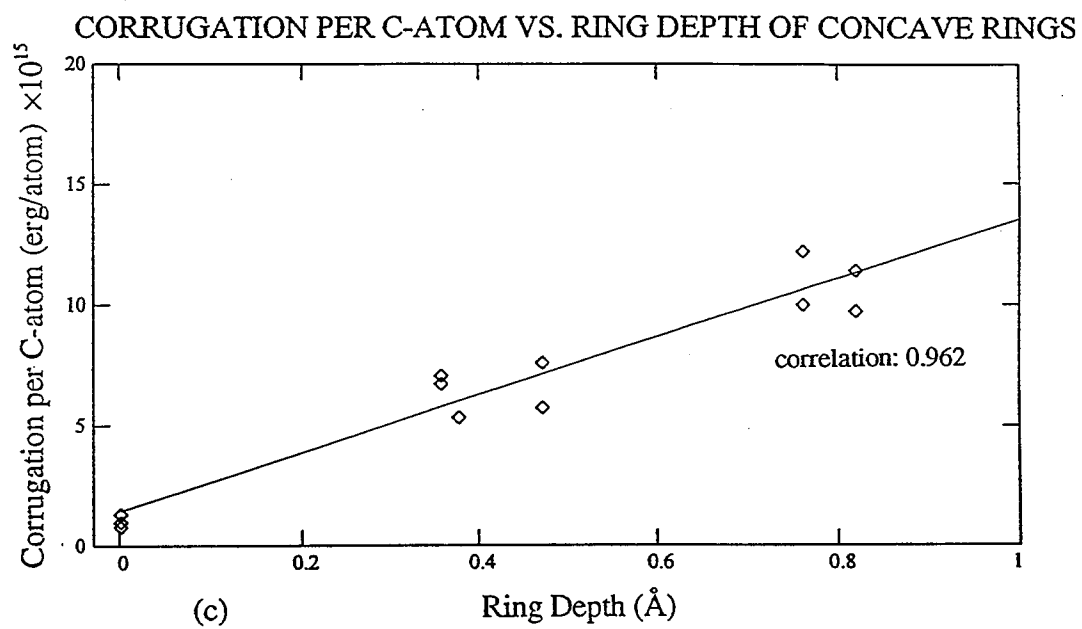


FIG. 29. Continued

ring angle for all sized rings together (0.929) shown in Fig. 29(b) and is comparable with those for the separate curves in Fig. 28(a). Thus, this analysis confirms that the corrugation of convex three ring clusters is proportional to the number of C-atoms in the ring. This means that the magnitude of corrugation on a ring of a convex three ring cluster is also linearly proportional to the number of C-atoms of the ring. Put another way, the corrugation per ring angle per C-atom is constant for convex three ring clusters. From this relation between the corrugation and the convex three ring cluster ring angles, we can again conclude that the wrinkling of substrates is an important factor in determining the corrugations of the substrates. (Note that this conclusion has been verified only over ring angles from 0° to 20° and for 5-, 6-, and 7-membered rings.)

For concave three ring clusters, the corrugations is better correlated with ring depth, which is defined in Fig. 27(b), than ring angle. The ring depth is also a measure of the degree of wrinkling of the substrates. Fig. 28(b) shows this relation between the ring depth and corrugation for 5-, 6-, and 7-membered rings in concave three ring clusters separately. Like the convex three ring clusters, concave three ring clusters also have an approximately linear relationship between corrugation and the number of C-atoms in the ring. Fig. 29(c) shows the universal curve obtained by plotting ring depth versus corrugation per ring atom. The correlation coefficient for Fig. 29(c) (0.962) is significantly greater than the correlation coefficient for corrugation versus ring depth for all sized rings together (0.933) shown in Fig. 29(d) and is comparable with those for the separate curves in Fig. 28(b). Thus, this analysis confirms that the corrugation of concave three ring clusters is proportional to the number of C-atoms in the ring. As a consequence, we can say that corrugation per ring depth per C-atom is constant in concave three ring clusters, similarly to our finding for convex ring clusters.

Next, consider the most favorable physisorption sites. For convex or concave ring clusters, the most favorable physisorption sites occurred just above dented parts of

the g-C surface. We can understand this characteristic as follows. Consider a Kr atom and several free C-atoms. If the interaction potential between the Kr atom and a C-atom is given by $\phi_{\text{Kr-C}}$ and if there is no interaction between C-atoms, then the C-atoms will be located on the surface of a sphere with radius 3.92\AA , the radial distance where $\phi_{\text{Kr-C}}$ is a minimum (see equations 3.B.2 and 3.C.1). Because g-C is a solid substrate, the interactions between C-atoms minimally affect the structure of a given g-C. To determine the position of the position of a Kr adatom on g-C, we can neglect the interactions between C-atoms of g-C in comparison with $\phi_{\text{Kr-C}}$. Thus, the above assumption is reasonable when we consider the interactions for a Kr atom and the g-C system. A dented substrate structure is more similar to this sphere than a flat or a convex substrate structure (effectively has more nearest neighbors); hence physisorption sites on such dented, concave regions are more favorable.

The weighted average most stable physisorption height for Kr on convex ring clusters, which is the weighted average using the probability distribution of the convex three ring clusters, is 3.56\AA . This is about 0.13\AA higher than for physisorption at the most favorable sites on the basal plane of graphite. The weighted average most stable physisorption height on concave ring clusters is 3.8\AA , significantly larger than on convex ring clusters. For certain physisorption sites on a dented part of g-C, the closest C-atom from the Kr atom may not be the C-atom (A in Fig. 30) at the center of the dented substrate. For example, the distance between the Kr atom and B in Fig. 30 can be shorter or comparable to that between the Kr atom and A. Since σ of $\phi_{\text{Kr-C}}$ is 3.49\AA , if the physisorption height is about 3.43\AA (which is the most stable physisorption height for Kr at the most favorable sites on the basal plane of graphite) on a dented part of g-C, then there can be large repulsive forces between not only the Kr adatom and the C-atom at A but also between the Kr adatom and the C-atoms at B, B', and other similar positions. As a result, the number of C-atoms that contribute to the repulsive forces on

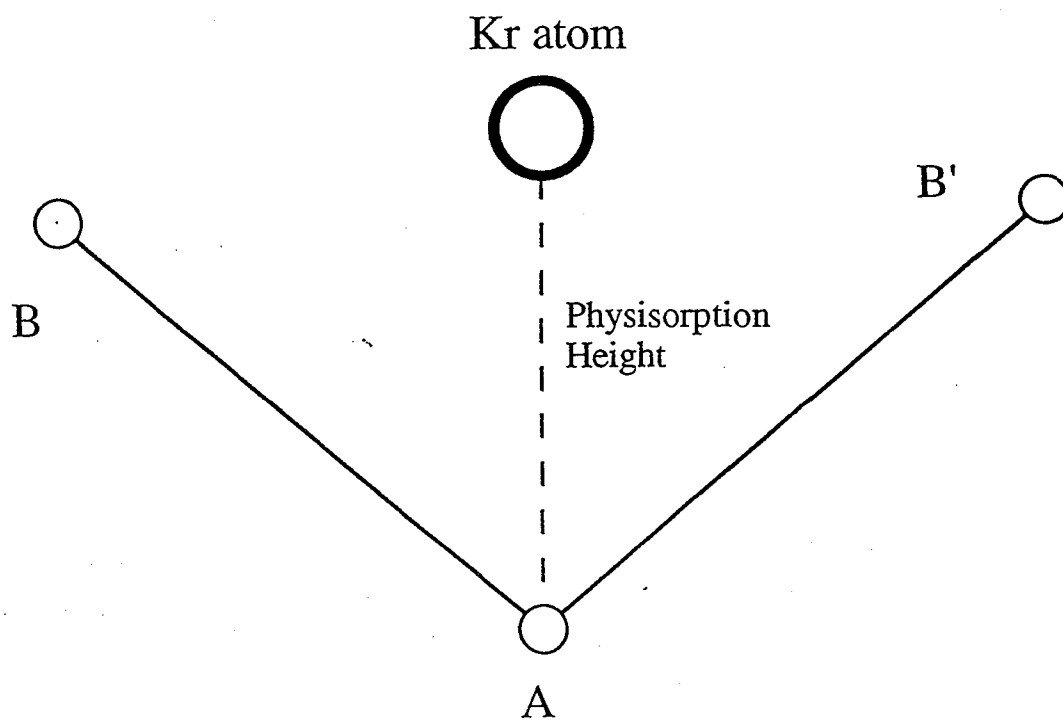


FIG. 30. Definition of physisorption height on a typical dented region of g-C.

the Kr atom can be more than contribute in a flat or a convex part of g-C. To reduce this repulsive forces, the physisorption height must be increased.

For flat ring clusters, the most favorable physisorption sites are located nearly above the center of the rings, except for 5-membered rings. In recalling that the most favorable physisorption sites for the basal plane of graphite are located above the centers of the hexagonal rings, this seems quite reasonable.

On a 5-membered ring, the most favorable physisorption site is located almost above the central C-atom. This can be understood by considering the geometry of the three ring clusters. (Because the RDM and CMM of the first layer and bulk g-C are symmetric about the center of the DMM, we need only consider the DMM.) Because 5-membered rings have fewer C-atoms than 6-, or 7-membered rings, the attractive forces are less than for 6- or 7-membered rings when the 5-membered rings are located at the 6- or 7-membered ring positions. As a consequence, the most favorable physisorption sites on 5-membered rings shifts from the ring center to the center of the DMM. An alternate explanation is based on the size of a 5-membered ring. The radius of the circle circumscribing a regular pentagon with side 1.42 Å is only 1.208 Å. The r_{\min} (i.e., the effective size of the Kr atom) of $\phi_{\text{Kr}-\text{C}}$ is 3.92 Å. If a Kr atom is just above the center of a 5-membered ring, then the physisorption height should be larger than 3.72 Å for the C-atoms of the 5-membered ring not to repulse the Kr atom, based on simple ball-and-stick geometry and the effective radii of the atoms. Practically, we find from our interaction energy calculations that favorable physisorption heights are greater than 3.721 Å. As a result, there are repulsive forces between the Kr atom and the C-atoms of the 5-membered ring and attractive forces between the Kr atom and the rest of the C-atoms of a three ring cluster. Therefore, the most stable physisorption site on a 5-membered ring shifts from the 5-membered ring center to the center of the three ring cluster. This arguments also explain why the most favorable physisorption sites on 7-

membered rings are shifted outward a little from the ring center.

B. Prediction of the structures of Kr adlayers

First, let us discuss the structure of a Kr adlayer for two extreme cases: (i) when the number of Kr adatoms is much less than the number needed to complete a full adlayer and (ii) when the number of Kr adatoms is sufficient to complete a full adlayer.

When the number of Kr adatoms is small, the huge corrugation of g-C will dominate the interactions between Kr adatoms. The magnitude of the minimum in $\phi_{\text{Kr-Kr}}$ (2.36×10^{-14} erg/Kr-Kr pair) is less than the weighted average corrugation of g-C (3.22×10^{-14} erg) and is much less than the largest corrugations for the 556-6 (8.1×10^{-14} erg) and 557-7 (8.5×10^{-14} erg) combinations. Therefore, the positions of the Kr atoms are determined by the corrugation of g-C in the low density limit. The Kr adatoms will physisorb preferentially on the most favorable physisorption sites (dented parts of the g-C surface), until all these sites are filled or until the density of Kr atoms increases to such a point that several Kr - Kr pairs are contributing significantly to the attractive Kr -Kr potential.

By contrast, when the Kr coverage reaches full adlayer coverage, the structure is determined by the interactions between Kr adatoms. In a 2D triangular lattice, many atoms (including six nearest neighbors, six next nearest neighbors, etc.) contribute to the attractive part of the Kr -Kr interaction potential. From Table X and Fig. 25, we can see that the net attraction of the triangular lattice exceeds the corrugation of even the most favorable sites for the nearest-neighbor spacings from 4.8 Å (corresponding to a coverage of $\theta = 0.7$ full monolayers) to 3.7 Å ($\theta = 1.2$ full monolayers). (Recall, full monolayer coverage occurs at a nearest-neighbor spacing of 4 Å.) This suggests that the interactions between Kr adatoms dominate the corrugation of g-C and govern the structure of the Kr adlayer from about $\theta = 0.7$ full monolayers to above full monolayer coverage.

At first, this appears to contradict the observation that Kr on graphite is commensurate at full adlayer coverage, despite the fact that the corrugation is less on graphite than on g-C. However, an important distinction between adsorption on g-C and the basal plane of graphite is that the most favorable physisorption sites of g-C are randomly distributed on the surface of g-C. If the number of Kr adatoms is large so that Kr adatoms are located not only on the most favorable physisorption sites but also on many less favorable sites, then shifting the Kr adatoms in a 2D triangular lattice as a whole across the g-C surface will not make an appreciable change in the binding energy of the entire Kr adlayer. That is, if the number of Kr adatoms is large enough, then corrugation does not appreciably affect the binding energy of adlayer.

It is important to recognize that the corrugation may still have an effect on the local structure of the 2D triangular lattice of the completed adlayer. The most favorable sites may act to pin the lattice locally. Frustration, due to competing pinning of the lattice by nearby most favorable sites, may also cause local distortions or defects in the lattice. The relatively shallow minimum, 15.0×10^{-14} erg, in Fig. 25, in comparison with the corrugation of the most favorable sites (i.e., 10.3×10^{-14} erg for the 556-6 convex ring or the 557-7 convex ring), allows significant distortion in nearest neighbor bond lengths with for relatively small costs in energy. Since perhaps one in five or ten sites may have large corrugation, the density of these distortion, should be quite high, having a major impact on of the structure of the "lattice."

Now, let us consider a case when a few Kr adatoms are removed from the completed adlayer. We know from the discussion in Section G in chapter 3, that for a substrate *with no corrugation* the removal of Kr adatoms will result in a similar 2D triangular lattice adlayer structure with decreased density and increased nearest-neighbor distance. Based on the discussion in the paragraphs above, it is reasonable to expect similar behavior when the g-C corrugation is considered, at least for removal of modest

numbers of Kr adatoms such that the resulting Kr adatom - Kr adlayer interactions are still larger than the g-C corrugation. We can predict quantitatively how long the 2D triangular lattice will be maintained, as we successively remove Kr adatoms from the full adlayer. Let us suppose that there are N Kr adatoms in the full monolayer with nearest-neighbor distance $b = 4 \text{ \AA}$, the radial distance for the minimum in Fig. 25. By removing ΔN Kr adatoms from the full monolayer, the average area per Kr adatom in the adlayer is increased by $\frac{N}{N - \Delta N}$, which corresponds the coverage decrease by $\theta = \frac{N - \Delta N}{N}$, and the nearest-neighbor distance is increased by $\sqrt{\frac{N}{N - \Delta N}}$. From our results in Section G in chapter 3 (see Table X), we can calculate how much the interaction energy of a Kr adatom with the rest of the Kr adlayer is decreased by this process. If the decreased Kr adatom - Kr adlayer interaction energy is still greater than the corrugation, then the structure of the 2D triangular lattice will be more or less maintained. However, if the corrugation is greater, then the Kr adlayer will no longer resemble a 2D triangular lattice. Based on this admittedly simplified analysis, we would expect a cross-over from one adlayer behavior to the other to occur at a nearest-neighbor spacing of about 4.8 \AA , which corresponds to coverage of $\theta = 0.7$ full monolayers.

C. Limitation of the model of g-C

The primary source of uncertainty in the Kr - g-C interaction energy calculations in this thesis is the inadequacy of the structural model of g-C. We outline below the shortcomings of the model and suggest ways in which portions of these problems with the model might be corrected.

First, we expect we have overestimated the wrinkling of the g-C surface. The variation in height for the convex or concave three ring clusters ranges from 0.762 \AA to 1.325 \AA . Although the weighted height variation of all three ring clusters (0.552 \AA) is in the range of $<1 \text{ \AA}$ estimated from surface structure measurements (refer to Section

D.3 in chapter 2), the height variation of our model is still too high over the lateral dimensions ($\leq 8.4 \text{ \AA}^2$). We identify several factors, which have not been fully considered in our structural model of g-C, which argue for a substantial reduction of the wrinkling in our model.

The interaction between π -orbitals reduces the wrinkling of the surface of g-C.¹⁶ This repulsion between π -bonds comes from the exchange interaction resulting from the overlapping of the orbitals. Minimum overlap occurs when the π -bonds are parallel, and is proportional to $-\cos\phi$, where ϕ is the dihedral angle along the π -bond. Therefore, the π -bond energy is minimized when all the π -orbitals are aligned with $\phi=0$. As a result, π -bondings provide a strong constraint to a surface of g-C to reduce its wrinkling.

A wide variation of the intraplanar bond angle also reduces the wrinkling of the surface of g-C. The C1120 structural model has a continuous bond angle distribution with a width of $\pm 5^\circ$.²⁹ However, the non-flat three ring clusters models consider in this thesis, which caused the vast majority of the wrinkling in our model, employ only three different angles for regular pentagons, hexagons, and heptagons.

As mentioned, in some structural model the sp^3 bonded C-atoms cement the quasi-planar rafts of g-C.^{19,21} Because an sp^3 bond has non-directional four-fold bonding, the sp^3 bonded C-atoms, even though their number is small (the portion of sp^3 sites in g-C is less than 15%), effectively protect for the quasi-planar rafts from having dangling or truncated bonds. In this work we have not considered dangling bonds or raft edges, both of which could produce preferred physisorption sites with large binding energies. Further, the presence of an additional bond can act to reduce stress in the carbon network and lead to smoother surface for g-C.

As long as the wrinkling of g-C is an important factor in determining the corrugation of the substrate, it is essential to model this aspect to more accurately reflect

the true structure of g-C. To improve the structural model, it should contain some sp^3 bonded C-atoms and should allow an appropriate distribution of bond angles as well as bond lengths based on the force constants of graphite (refer to Table V). However, these improvements will drastically increase the number of elements to consider in the DMM ensemble. Furthermore, a wide bond angle distribution will make the calculation of the three ring probability distribution for each element of the DMM ensemble substantially more difficult and cumbersome.

Another serious limitation of the structural model is that the size of the DMM is too small to produce accurate results for the Kr - g-C interaction energy calculations. When the central Kr atom is near the center of the DMM, there is little problem in the calculation, as discussed in Section E of Chapter 2. However, as the central Kr atom approaches to the edge of the DMM, the distance between the central Kr atom and the front part of the DMM of the first layer is too short to satisfy the conditions in Section E of chapter 2. Furthermore, since the RDM does not incorporate wrinkling of the surface, the calculations of the corrugation at physisorption sites near the crossover between the RDM and the DMM cannot be as accurate as those near the center of the DMM. For example, in the 666 three ring cluster, the center of the three ring cluster is practically equivalent to the physisorption site at the edge of the cluster. In the binding energy calculation, the minimum binding energy of Kr at the center of the 666 three ring cluster is -160.986×10^{-15} erg and that at the edge of the 666 three ring cluster is -158.915×10^{-15} erg. Thus, the discrepancy between them is 2.053×10^{-15} erg, and this corresponds to 1.3% of the minimum binding energy at the center of the 666 three ring cluster. However, this discrepancy is 34% of the corrugation of the 666 three ring cluster, and is not negligible to the corrugation.

To remedy this limitation, the DMM portion of the g-C model should contain larger ring clusters. However, this will also drastically increase the number of elements

in the DMM ensemble. To add one additional set of rings around the perimeter of the three ring clusters, which would require from 6 to 12 rings, increases the number of elements in the DMM ensemble from 35 to 110 if we consider flat ring clusters only. If we consider the wrinkling of the ring clusters, the number of DMM elements will be increased drastically. This is a daunting computational challenge.

When we made the model for g-C, the fundamental assumption was that the Kr - Kr and Kr - C-atom interactions on g-C were the same as those on the basal plane of graphite. To obtain more accurate calculation results, the effects of the g-C substrate to the Kr-Kr interaction should be studied on various kinds of g-C's experimentally. Kr-C interactions also be investigated experimentally. This thesis calculation can be used for other inert gas adsorbates, if we use appropriate adsorbate-adsorbate and the adsorbate-substrate interaction potential parameter σ and ϵ . If we can obtain more realistic values for Kr-Kr interactions and Kr - C-atom interactions on g-C, then based on the relations between these interactions and the corresponding interactions on the basal plane of graphite, we can better estimate the adsorbate-adsorbate and the adsorbate-substrate interaction potentials of any inert gas adsorbate on g-C.

CHAPTER 5

CONCLUSIONS

The primary objectives of this thesis research were to address the following three questions: (i) Will Kr adlayers form on g-C; (ii) What will their structures be; and (iii) How will the structures of the adlayers of Kr on g-C differ from structure of corresponding adlayers on graphite? We conclude this thesis by considering the answers for these three questions.

Let us consider the first question. The average minimum and maximum binding energies of Kr on g-C were determined to be 93% and 78% of those on graphite, respectively. In addition, a significant density of sites with much larger binding energies was identified on g-C. So, Kr adlayers will definitely form on g-C.

As we looked into the predicted structure of Kr adlayers on g-C in Section B of chapter 4, we found that the wrinkling of the g-C surface governs the structure of a Kr adlayer on g-C when the number of Kr atoms in the Kr adlayer is small. In this limiting case, Kr atoms will preferentially physisorb on the large binding energy sites of the dented parts of g-C only. As the number of Kr atoms in the Kr adlayer is increased, Kr atoms physisorbed on the dented parts of g-C will shift because the effect of the Kr-Kr interactions increases as the density of Kr adatoms increases. If the criteria, discussed in Section B of chapter 4, are satisfied, then Kr at higher coverage adlayers will develop into a 2D triangular lattice structure.

Finally, let us consider the last question. On g-C substrate, the topology of g-C (e.g., its wrinkling) is a more important factor in determining the structure of the Kr adlayer than the position of C-atoms within a ring. On the basal plane of graphite, corrugation is determined by the relative position of the C-atoms of a ring to the central Kr atom. On a g-C substrate, wrinkling dominates the relative position difference of C-atoms. Therefore, we can say that there is no direct relation between Kr adlayers on the

basal plane of graphite and those on a g-C substrate because the wrinkling of substrates is a property specific to g-C. In addition, the corrugation of g-C is much larger than that of the basal plane of graphite.

In conclusion, the study of the physisorption of inert gas adsorbates on g-C is not simply an extension of the physisorption of the inert gases on the basal plane of graphite, but can be expected (based on this research) to exhibit novel and intriguing properties driven by the structural properties of the amorphous carbon substrate.

REFERENCES

1. P.W. Atkins, *Physical Chemistry*, 3rd ed. (W.H. Freeman Company, New York, 1986) pp. 762-782.
2. A. Zangwill, *Physics at Surfaces* (Cambridge University Press, New York, 1988) pp. 185-291.
3. W. Steele, *Chem. Rev.*, **93**, 2355 (1993).
4. R.J. Birgeneau and P.M. Horn, *Science*, **232**, 329 (1986).
5. M.B. Gordon and J. Villain, *J. Phys. C*, **18**, 3919 (1985).
6. N.W. Ashcroft and N.D. Mermin, *Solid State Physics* (W.B. Saunders Company, New York, 1976), pp. 398-402.
7. J.G. Dash, *Physics Reports* **38**, 177 (1978).
8. J. Villain and M.B. Gordon, *Surf. Sci.*, **125**, 1 (1983).
9. S.K. Sinha, *Ordering in Two Dimensions* (Elsevier North Holland, Inc. New York, 1980), pp. 29-38.
10. S.R. Elliott, *Physics of Amorphous Materials*, 2nd ed. (Longman Scientific & Technical, New York, 1990), pp. 425-450.
11. A.D. Crowell and R.B. Steele, *J. Chem. Phys.*, **34**, 1347 (1961).
12. J.R. Dennison, Ph.D. Thesis, Virginia Polytechnic Institute and State University, 1985.
13. J.O. Stoner, Jr., *J. Appl. Phys.*, **40** (2), 707 (1969)
14. C. Gao, Y.Y. Wang, A.L. Ritter, and J.R. Dennison, *Phys. Rev. Lett.*, **62** (8), 945 (1989).
15. P.R. Wallace, *Phys. Rev.*, **71**, 622 (1947).
16. J. Robertson, *Adv. Phys.*, **35**, 317 (1986).
17. G. Dearnaley, *Rev. Sci. Instrum.*, **31**, 197 (1960).
18. T.E. Doyle and J.R. Dennison, *Phys. Rev. B*, **51** (1), 196 (1995).

19. C. Gao, Ph.D. Thesis, Virginia Polytechnic Institute and State University, 1988.
20. S.R. Elliott, *Physics of Amorphous Materials*, 2nd ed. (Longman Scientific & Technical, New York, 1990), pp. 71-184.
21. R. Zallen, *The Physics of Amorphous Solids* (Wiley, New York, 1983), pp. 33-134.
22. S.R. Elliott, *Nature*, **354**, 445 (1991).
23. W.H. Zachariasen, *J. Am. Chem. Soc.*, **54**, 3841 (1932).
24. S. Egrun, *Acta Crystallogr.*, **29A**, 605 (1976).
25. G. Galli, R.M. Martin, R. Car, and M. Parrinello, *Phys. Rev. Lett.*, **62** (5), 555 (1989).
26. B.J. Stanhous and P.J. Grout, *J. Non-Cryst. Solids*, **27**, 247 (1978).
27. C.Z. Wang and K. M. Ho, *Phys. Rev. B*, **50**, 12429, (1994).
28. C.Z. Wang, K.M. Ho, and C.T. Chan, *Phys. Rev. Lett.*, **70**, 611 (1993).
29. D. Beeman, J. Silveanu, R. Lynds, and M.R. Anderson, *Phys. Rev. B*, **30**, 870 (1984).
30. D.F.R. Mildner and J.M. Carpenter, *J. Non-Cryst. Solids*, **47**, 391 (1982).
31. B.T. Boiko, L.S. Palatnik, and A.S. Derevyanchenko, *Dokl. Akad. Nauk SSSR*, **179**, 316 (1968).
32. J. Kakinoki, K. Katana, T. Hanawa, and T. Ino, *Acta Crystallogr.*, **13**, 171 (1960).
33. T.E. Doyle, M.S. Thesis, Utah State University, 1992.
34. D. Vanderbilt and J. Tersoff, *Phys. Rev. Lett.*, **68**, 511 (1992).
35. T. Lenosky, X. Gunze, M. Teter and V. Elser, *Nature*, **355**, 333 (1992).
36. S.J. Townsend, T.J. Lenosky, D.A. Muller, C.S. Nichols, and V. Elser, *Phys. Rev. Lett.*, **69**, 921 (1992).

37. N. Rivers, *Phil. Mag. A*, **40**, 859 (1979).
38. B. Marchon, M.R. Khan, and D.B. Bogy, *IEEE Trans. Magn.*, **27** (6), 5067 (1991).
39. H.-J Butt, D.N. Wang, P.K. Hansma, and W. Kuhlbrandt, *Ultramicroscopy*, **36**, 307 (1991).
40. A. Stemmer, R. Reichelt, A. Engel, J.P. Rosenbusch, M. Rigger, H.R. Hidber, and H.-J. Güntherodt, *Surf. Sci.*, **181**, 394 (1987).
41. C. Weissmantel, E. Ackermann, K. Bewilogua, G. Hecht, H. Kapfer, and B. Ray, *J. Vac. Sci. Technol. A*, **4**, 2892 (1989).
42. J.O. Stoner, *Floating and Mounting Instructions-Carbon Foils and Some Metal Foils*, (Arizona Carbon Foil Co., Tucson, Arizona 1993) pp. 1-3.
43. S.L. Flegler, J.W. Heckman, Jr., and K.L. Klomparens, *Scanning and Transmission Electron Microscopy: an Introduction* (W.H. Freeman and Company, New York 1993) p. 89.
44. L. Reimer, *Scanning Electron Microscopy* (Springer-Verlag, New York 1985), pp. 243-244.
45. B. Bhushan, J.C. Wyant, and C.L. Koliopoulos, *Appl. Opt.*, **24**, 1489 (1985).
46. K. Creath, *Appl. Opt.*, **26** (14), 2810 (1987).
47. *Non-Contact Microsurface Measurement Systems* (WYCO Co., Tucson, Arizona, 1988), pp. 1-2.
48. S.S. Perry and G.A. Somorjai, *Anal. Chem.*, **66** (7), 403A (1994).
49. *Digital Instruments Nanoscope II-Scanning Probe Microscope*, Instruction Manual V.5 (Digital Instruments Nanoscope, New York, 1990), pp. 3-43.
50. J.M. Walls and R. Smith, *Surface Science Techniques* (Pergamon, New York, 1994) pp. 157-158.
51. J. Tersoff, *Phys. Rev. Lett.*, **61**, 2879 (1988).

52. T.E. Doyle and J.R. Dennison, *J. Non-Cryst. Solids*, to be published.
53. R. Nicklow, W. Wakabayashi, and H.G. Smith, *Phys. Rev. B*, **5**, 4951 (1972).
54. R. Al-Jish and G. Dresselhaus, *Phys. Rev. B*, **26**, 4514 (1982).
55. J.A. Young and J.V. Koppel, *J. Chem. Phys.*, **42**, 357 (1965).
56. K. Kesauasamy and N. Krishnamurthy, *Ind. J. Pure and Appl. Phys.*, **17**, 73 (1979).
57. F. Tuinstra and J.L. Koenig, *J. Chem. Phys.*, **53** (3), 1126 (1970).
58. G.B. Spence and E.J. Seldia, *Physical Properties of Graphite* (Elsevier, London, 1968), p.35.
59. A. Yoshimori and Y. Kitano, *J. Phys. Soc. Japan*, **2**, 352 (1956).
60. *PCMODEL-molecular modeling software for personal workstation* (Serena Software, Bloomington, Indiana) pp. 1-61.
61. S.K. Sinha, *Ordering in Two Dimensions* (Elsevier North Holland, Inc. New York, 1980), p. 231.
62. A.D. McLachlan, *Mol. Phys.*, **7**, 381 (1964).
63. J.D. Jackson, *Classical Electrodynamics*, 2nd ed., (John Wiley & Sons, Inc., New York, 1975), pp. 136-162.
64. E.A. Taft and H.R. Philipp, *Phys. Rev.*, **138A**, 197 (1965).
65. N. Savvides, *J. Appl. Phys.*, **59** (2), 4133 (1986).
66. J.R. Taylor, *An Introduction to Error Analysis*, (University Science Books, Mill Valley CA, 1982), pp. 178-182.

The correlation between two variables p and q is defined by Ref.[66]

$$\text{correlation}(p, q) = \frac{\sum_i (p_i - \bar{p})(q_i - \bar{q})}{\sqrt{\sum_i (p_i - \bar{p})^2 \sum_i (q_i - \bar{q})^2}}$$

In this correlation function, we can get the linearity between p and q. If their relation is perfectly linear, then the absolute value of their correlation will be one. If they do not have

any relation, then their correlation will be zero.

APPENDICES

APPENDIX 1: CALCULATION OF INTERACTION ENERGY BETWEEN Kr AND GRAPHITE ALONG THE SYMMETRIC LINE OF A HEXAGON

ORIGIN=1 $\text{\AA}=10^{-10}\text{m}$

Lattice constants of a unit cell of graphite: $a_o := 2.463 \text{ \AA}$ $c_o := 6.714 \text{ \AA}$

Intraplanar sp^2 bond length: $a := \frac{a_o}{\sqrt{3}} \text{ \AA}$ $a = 1.422 \text{ \AA}$

Basis vectors of representing the positions graphite unit cells:

$$a1 := \begin{pmatrix} a_o \\ 0 \\ 0 \end{pmatrix} \quad a2 := \begin{pmatrix} a_o \cdot \cos\left(\frac{\pi}{3}\right) \\ a_o \cdot \sin\left(\frac{\pi}{3}\right) \\ 0 \end{pmatrix} \quad a3 := \begin{pmatrix} 0 \\ 0 \\ -c_o \end{pmatrix}$$

$$a1 = \begin{pmatrix} 2.463 \\ 0 \\ 0 \end{pmatrix} \text{ \AA} \quad a2 = \begin{pmatrix} 1.232 \\ 2.133 \\ 0 \end{pmatrix} \text{ \AA} \quad a3 = \begin{pmatrix} 0 \\ 0 \\ -6.714 \end{pmatrix} \text{ \AA}$$

Coordinates of the C-atoms in a unit cell of graphite:

$$e1 := \begin{pmatrix} 0 \\ 0 \\ 0 \end{pmatrix} \quad e2 := \frac{1}{3} \cdot a1 + \frac{1}{3} \cdot a2 \quad e3 := \frac{1}{2} \cdot a3 \quad e4 := \frac{2}{3} \cdot a1 + \frac{2}{3} \cdot a2 + \frac{1}{2} \cdot a3$$

$$e1 = \begin{pmatrix} 0 \\ 0 \\ 0 \end{pmatrix} \text{ \AA} \quad e2 = \begin{pmatrix} 1.232 \\ 0.711 \\ 0 \end{pmatrix} \text{ \AA} \quad e3 = \begin{pmatrix} 0 \\ 0 \\ -3.357 \end{pmatrix} \text{ \AA} \quad e4 = \begin{pmatrix} 2.463 \\ 1.422 \\ -3.357 \end{pmatrix} \text{ \AA}$$

Indices indicating range of graphite unit cells which participate in the interaction energy calculation:

$$r := -20..20 \quad s := -20..20 \quad t := 0..4$$

Indices indicating positions of the central Kr atom:

$$p := 1..13 \quad q := 1..6$$

Basis vectors representing the position of Kr atoms:

$$b1 := \begin{pmatrix} 0 \\ \frac{a}{6} \\ 0 \end{pmatrix} \quad b2 := \begin{pmatrix} 0 \\ 0 \\ 0.1 \end{pmatrix} \quad b0 := \begin{pmatrix} 0 \\ 0 \\ 3.0 \end{pmatrix}$$

$$b1 = \begin{pmatrix} 0 \\ 0.237 \\ 0 \end{pmatrix} \text{ \AA} \quad b2 = \begin{pmatrix} 0 \\ 0 \\ 0.1 \end{pmatrix} \text{ \AA} \quad b0 = \begin{pmatrix} 0 \\ 0 \\ 3 \end{pmatrix} \text{ \AA}$$

Coefficients in Lennard-Jones
6-12 potential:

$$A := 67.6 \cdot 10^{-12} \text{ erg} \quad r_0 := 3.92 \text{ \AA}$$

Interaction energy between the central Kr atom and C-atom's equivalent to e1:

$$U1_{q,p} := (-A) \cdot \left[\sum_r \sum_s \sum_t \left[(|(p-1) \cdot b1 + q \cdot b2 + b0 - (r \cdot a1 + s \cdot a2 + t \cdot a3 + e1)|)^{-6} \dots \right. \right. \\ \left. \left. + \left(\frac{r_0^6}{2} \right) \cdot (|(p-1) \cdot b1 + q \cdot b2 + b0 - (r \cdot a1 + s \cdot a2 + t \cdot a3 + e1)|)^{-12} \right] \right]$$

Interaction energy between the central Kr atom and C-atom's equivalent to e2:

$$U2_{q,p} := (-A) \cdot \left[\sum_r \sum_s \sum_t \left[(|(p-1) \cdot b1 + q \cdot b2 + b0 - (r \cdot a1 + s \cdot a2 + t \cdot a3 + e2)|)^{-6} \dots \right. \right. \\ \left. \left. + \left(\frac{r_0^6}{2} \right) \cdot (|(p-1) \cdot b1 + q \cdot b2 + b0 - (r \cdot a1 + s \cdot a2 + t \cdot a3 + e2)|)^{-12} \right] \right]$$

Interaction energy between the central Kr atom and C-atom's equivalent to e3:

$$U3_{q,p} := (-A) \cdot \left[\sum_r \sum_s \sum_t \left[(|(p-1) \cdot b1 + q \cdot b2 + b0 - (r \cdot a1 + s \cdot a2 + t \cdot a3 + e3)|)^{-6} \dots \right. \right. \\ \left. \left. + \left(\frac{r_0^6}{2} \right) \cdot (|(p-1) \cdot b1 + q \cdot b2 + b0 - (r \cdot a1 + s \cdot a2 + t \cdot a3 + e3)|)^{-12} \right] \right]$$

Interaction energy between the central Kr atom and C-atom's equivalent to e4:

$$U4_{q,p} := (-A) \cdot \left[\sum_r \sum_s \sum_t \left[(|(p-1) \cdot b1 + q \cdot b2 + b0 - (r \cdot a1 + s \cdot a2 + t \cdot a3 + e4)|)^{-6} \dots \right. \right. \\ \left. \left. + \left(\frac{r_0^6}{2} \right) \cdot (|(p-1) \cdot b1 + q \cdot b2 + b0 - (r \cdot a1 + s \cdot a2 + t \cdot a3 + e4)|)^{-12} \right] \right]$$

Total interaction energy between the central Kr atom and graphite in erg:

$$U_{q,p} := U1_{q,p} + U2_{q,p} + U3_{q,p} + U4_{q,p}$$

$$\frac{U}{10^{-15}} = \begin{bmatrix} -96.46 & -98.42 & -104.6 & -113.9 & -123.9 & -131.5 & -134.4 & -131.5 & -123.9 & -113.9 & -104.6 & -98.42 & -96.46 \\ -145.4 & -146.6 & -150.2 & -155.7 & -161.7 & -166.2 & -167.9 & -166.2 & -161.7 & -155.7 & -150.2 & -146.6 & -145.4 \\ -171.4 & -172.1 & -174.3 & -177.6 & -181.1 & -183.8 & -184.9 & -183.8 & -181.1 & -177.6 & -174.3 & -172.1 & -171.4 \\ -183 & -183.4 & -184.7 & -186.6 & -188.8 & -190.4 & -191 & -190.4 & -188.8 & -186.6 & -184.7 & -183.4 & -183 \\ -185.4 & -185.7 & -186.4 & -187.6 & -188.9 & -189.9 & -190.3 & -189.9 & -188.9 & -187.6 & -186.4 & -185.7 & -185.4 \\ -182.3 & -182.4 & -182.9 & -183.6 & -184.4 & -185 & -185.2 & -185 & -184.4 & -183.6 & -182.9 & -182.4 & -182.3 \end{bmatrix}$$

$$\text{WRITEPRN}(\text{GRP_U6}) := \frac{U}{10^{-15}}$$

APPENDIX 2: CALCULATION OF RING STATISTICS AND THREE RING CLUSTER PROBABILITY DISTRIBUTION

A-2-1 Probability Distribution of n-membered Rings (Ring Statistics)

Let N_i be the number of i -membered rings in a sample, where $i = 5, 6, \text{ or } 7$.

The definition of probability of each i -membered ring is

$$p_i = \frac{N_i}{\sum_i N_i}. \quad (\text{A.2.1})$$

The definition of rings per C-atom of each i -membered ring, σ_i , is

$$\sigma_i = \frac{N_i}{\eta_a}, \quad (\text{A.2.2})$$

where η_a is the total number of C-atoms in the sample. Then, from the equation (A.2.2),

$$p_i = \frac{\eta_a}{\sum_i N_i} \sigma_i. \quad (\text{A.2.3})$$

Therefore,

$$\sum_{j=5}^7 p_j = \frac{\eta_a}{\sum_i N_i} \sum_{j=5}^7 \sigma_j. \quad (\text{A.2.4})$$

From the definition of p_i , it is evident that $\sum_{j=5}^7 p_j = 1$. Thus,

$$\frac{\eta_a}{\sum_i N_i} \sum_{j=5}^7 \sigma_j = 1. \quad (\text{A.2.5})$$

Generally, it is true that

$$\frac{\eta_a}{\sum_i N_i} = 2 \quad (\text{A.2.6})$$

for any 2D 3-fold bonded CRN, which implies that

$$\sum_{j=5}^7 \sigma_j = 0.5. \quad (\text{A.2.7})$$

The number of rings per C-atom as given by Beeman[29] for C1120 satisfies this requirement. The σ_i 's for C1120 are given by $\sigma_5 = 0.106$, $\sigma_6 = 0.294$, and $\sigma_7 =$

0.100. Then from the equations (A.2.4) and (A.2.6), the probability distribution of i -membered rings (ring statistics) is given by

$$p_5=0.212, p_6=0.588, \text{ and } p_7=0.200. \quad (\text{A.2.8})$$

A-2-2 Calculation of Combined Probabilities of Three Ring Clusters

The combined probability of a three ring cluster is equal to the number of ways to make the three ring cluster with the three component rings (the multiplicity) times the probability (ring statistics) of each of the three component rings. In other words, the combined probability p_{lmn} of the three ring cluster composed of l -, m -, and n -membered rings is given by

$$p_{lmn} = n_{lmn} \times p_l \times p_m \times p_n, \quad (\text{A.2.7})$$

where n_{lmn} is the lmn -three ring cluster multiplicity and p_l is the probability of l -membered ring. The probability of each ring is given in the equation (A.2.8). The three ring cluster multiplicity and the resultant combined probabilities of the three-ring clusters are shown in Table XVI.

A-2-3 The Probability for the Central Kr Atom to be Adsorbed on an n -membered Ring of an lmn -three Ring Cluster

The probability for the central Kr atom to adsorb on an n -membered ring of an lmn -three ring cluster, R_{lmn-n} is given by

$$R_{lmn-n} = \frac{A_n}{\Sigma A} \times p_{lmn}, \quad (\text{A.2.8})$$

where A_n and ΣA are the area of the n -membered ring and the total area of the lmn -three ring cluster, respectively. The resultant probability of the number of physisorption sites on a given ring of a three ring cluster is listed in Table XVII.

This probability of number of physisorption sites on given rings of a three ring cluster will be used as weighting factors for the calculations of the weighted average

minimum and maximum energies and corrugations.

TABLE XVII. Probability distribution of three ring clusters.

Three Ring Cluster	Ring Cluster Multiplicity	Combined Probability of Three Ring Clusters
555	1	0.010
556	3	0.079
557	3	0.027
566	3	0.220
567	6	0.150
577	3	0.025
666	1	0.203
667	3	0.207
677	3	0.071
777	1	0.008
Total	27	1.000

TABLE XVIII. The probability of physisorption on a given ring of a three ring cluster.

Ring	Probability of physisorption on a given ring of a three ring cluster	Ring	Probability of physisorption on a given ring of a three ring cluster
555-5	0.010	567-7	0.060
556-5	0.049	577-5	0.006
556-6	0.031	577-7	0.019
557-5	0.015	666-6	0.203
557-7	0.012	667-6	0.130
566-5	0.063	667-7	0.078
566-6	0.157	677-6	0.021
567-5	0.040	677-7	0.050
567-6	0.050	777	0.008

APPENDIX 3: DETERMINATION OF THE COORDINATES OF CARBON ATOMS OF DISCRETE MEDIUM MODEL

To determine the C-atom coordinates, let us examine the DMM separately for two cases, $\theta_1 + \theta_2 + \theta_3 \leq 2\pi$ and $\theta_1 + \theta_2 + \theta_3 > 2\pi$, where the angles θ_1 , θ_2 , and θ_3 are defined in Fig. 2-15. First, let us consider the case that $\theta_1 + \theta_2 + \theta_3 \leq 2\pi$. For this case, regular polygons will be used as the representative shapes for the corresponding rings. Then the three ring clusters will form either convex clusters or concave clusters. We will subsequently assume that a convex three ring cluster has the same likelihood of occurrence as its corresponding concave three ring cluster. In reality, the convex and concave configurations will mostly likely not be equally probable, but rather will depend on their configuration energies of the clusters. As mentioned, however, we can not calculate the exact configuration energies of three ring clusters and as a result, we can not calculate relative probability of each type of three ring cluster.

Now, let us consider the plane defined by the positions of the three nearest neighbor C-atoms from the central C-atom (C-atom nearest to the origin). Further, consider the triangle in this plane whose vertices consist of the nearest neighbor C-atoms. The z-axis is perpendicular to this plane and passes through the central C-atom, with the x-y plane at the level of the average height of the RDM and the CMM. The x-axis is determined by the position of the central Kr atom without loss of generality. Since we have uniquely determined the origin, z-axis and x-axis, we have specified a complete coordinate system.

Note, the central C-atom is not at the origin. Rather, for convex ring clusters the central C-atom is along the positive z-axis and for concave ring clusters it is along the negative z-axis. This violates the condition that there should be a C-atom at the origin to

use the RDF to determine the density for the RDM. However, the average position of the central C-atom is still at the origin, since we assume that the convex three ring clusters and the concave three ring clusters are equally probable. Since our calculations are for statistically averaged structure of g-C, we can still use $J(r)$ of the C1120 model to determine the density for the RDM.

Let us now consider the case that $\theta_1 + \theta_2 + \theta_3 > 2\pi$. For this case, we distort the angles θ_1 , θ_2 , and θ_3 in such a way as to maintain the three rings in a plane while leaving the bond lengths unchanged. The distorted angles of θ_1 , θ_2 , and θ_3 are θ_1' , θ_2' , and θ_3' , respectively. To determine these distorted angles, we assume that

$$\theta_i' \propto \theta_i \quad (\text{A.3.1})$$

where $i = 1, 2, \text{ or } 3$. This relation means that the amount of distortion $\Delta\theta_i \equiv |\theta_i' - \theta_i|$ is proportional to the magnitude of the initial angle θ_i before distortion. For the $\theta_1 + \theta_2 + \theta_3 > 2\pi$ case, all $\theta_i > \frac{2\pi}{3}$ (except for the angle of the pentagon in the three ring cluster composed of one pentagon and two heptagons), where $\frac{2\pi}{3}$ is the bond angle for a 2D hexagonal lattice. Since we are considering small distortions ($\leq 9^\circ$) compared to θ_i ($\geq 108^\circ$), it is reasonable to assume that $\Delta\theta_i$ is linearly proportional to θ_i , that is $\Delta\theta_i \propto \theta_i$. In other words, we can use a "small angle approximation" or "harmonic approximation". To keep the three rings in a plane, we further require that

$$\theta_1' + \theta_2' + \theta_3' = 2\pi. \quad (\text{A.3.2})$$

The equations (A.3.1) and (A.3.2) uniquely determine the distorted angles.

Let us further assume that the polygons are symmetric about the lines (x-axes) shown in Figs. 31, 32, and 33 and that the central C-atom is at the origin. We now consider how to determine the relative coordinates of the other C-atoms for pentagons, hexagons, and heptagons, respectively.

A-3-1 Pentagon (see Fig. 31)

Let θ_5' be the distorted angle determined by equations (A.3.1) and (A.3.2) for a pentagon. The angles α , β of Fig. 2-16 are determined by

$$\alpha = \cos^{-1} \left\{ \frac{1}{2} \left[2 \cos^2 \frac{\theta_5'}{2} + \sin \frac{\theta_5'}{2} + \sqrt{\left[2 \cos^2 \frac{\theta_5'}{2} + \sin \frac{\theta_5'}{2} \right]^2 - 1} \right]^{1/2} \right\} \quad (\text{A.3.3})$$

and

$$\beta = \frac{\theta_5'}{2} - \alpha. \quad (\text{A.3.4})$$

If we consider only the region with $x \geq 0$ and $y \geq 0$ region, then the relative coordinates of the first nearest neighbor to the central C-atom at $\bar{R}_0^5 = (0, 0, 0)$ are

$$\bar{R}_1^5 = \left(a \cos \frac{\theta_5'}{2}, a \sin \frac{\theta_5'}{2}, 0 \right), \quad (\text{A.3.5})$$

where a is the average intraplanar sp^2 bonding length of C1120, 1.42 Å. The relative coordinates of the second nearest neighbor are given by

$$\bar{R}_2^5 = \left(2a \cos \alpha \cos \beta, \frac{a}{2}, 0 \right). \quad (\text{A.3.6})$$

A-3-2 Hexagon (see Fig. 32)

Let the distorted angle for a hexagon determined by equations (A.3.1) and (A.3.2) be θ_6' . Unlike the pentagon case, knowing θ_6' and the bond length a does not uniquely determine the relative coordinates of all the other C-atoms for a hexagon. One more constraint is needed; we assume that the opposite angles of the hexagon along the symmetry axis are equal, that is that the distortion is symmetric. Again, we consider only $x \geq 0$ and $y \geq 0$. Then, the relative coordinates of the first, second, and third nearest neighbors are given respectively by;

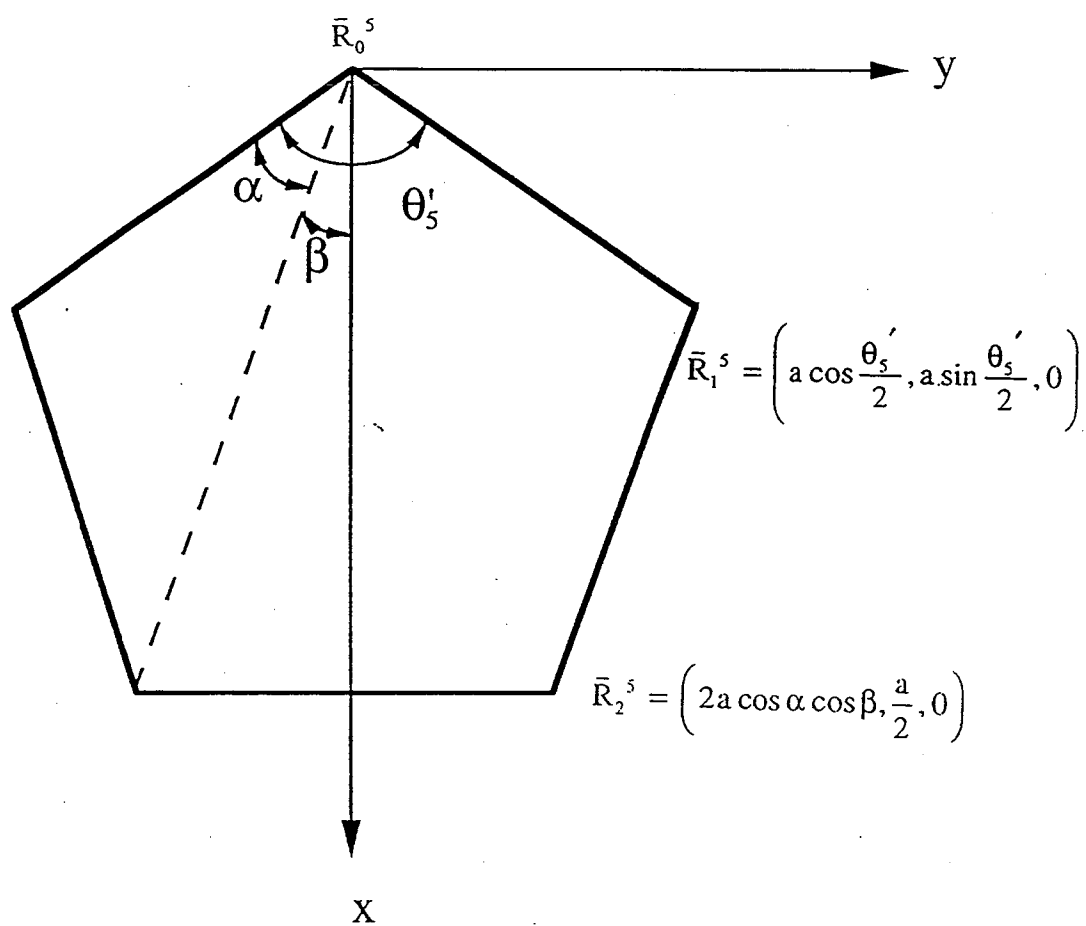


FIG. 31. Coordinates of a 5-membered ring C-atom.

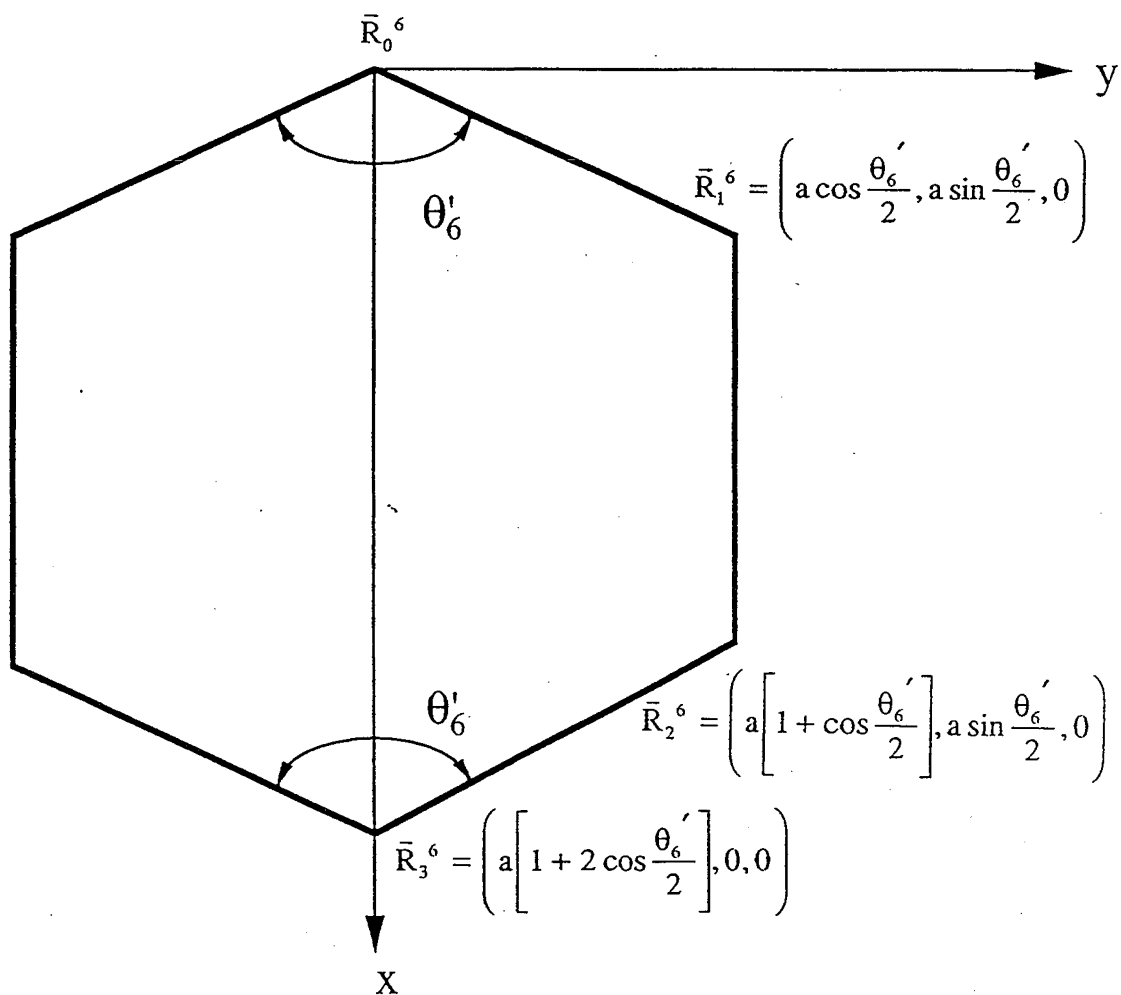


FIG. 32. Coordinates of a 6-membered ring C-atom.

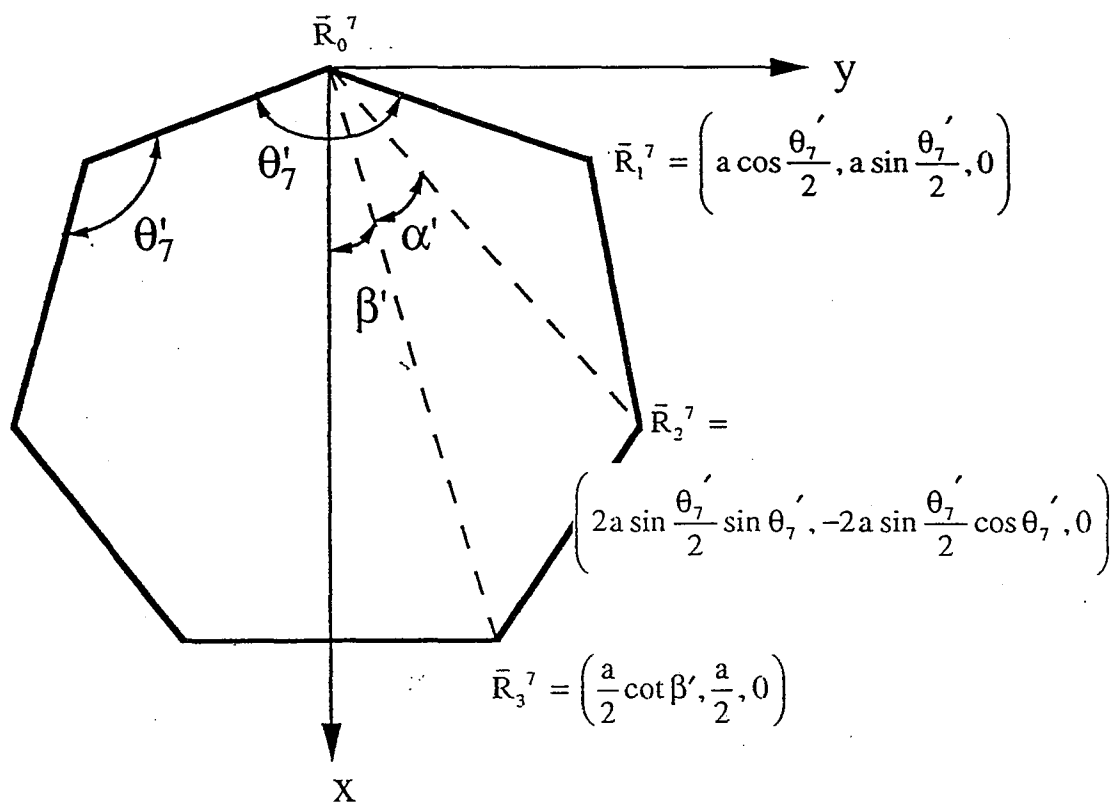


FIG. 33. Coordinates of a 7-membered ring C-atom.

$$\bar{R}_1^6 = \left(a \cos \frac{\theta_6'}{2}, a \sin \frac{\theta_6'}{2}, 0 \right). \quad (\text{A.3.7})$$

$$\bar{R}_2^6 = \left(a \left[1 + \cos \frac{\theta_6'}{2} \right], a \sin \frac{\theta_6'}{2}, 0 \right), \quad (\text{A.3.8})$$

and

$$\bar{R}_3^6 = \left(a \left[1 + 2 \cos \frac{\theta_6'}{2} \right], 0, 0 \right). \quad (\text{A.3.9})$$

A-3-3 Heptagon (see Fig. 33)

θ_7' is the distorted angle for a heptagon determined by equations (A.3.1) and (A.3.2). As with the hexagon case, we need one more constraint. We assume that the angle adjacent to θ_7' is equal to θ_7' . Again, we consider only the $x \geq 0$ and $y \geq 0$ region.

Then, the relative coordinates of the other C-atoms are given as:

$$\bar{R}_1^7 = \left(a \cos \frac{\theta_7'}{2}, a \sin \frac{\theta_7'}{2}, 0 \right), \quad (\text{A.3.10})$$

$$\bar{R}_2^7 = \left(2a \sin \frac{\theta_7'}{2} \sin \theta_7', -2a \sin \frac{\theta_7'}{2} \cos \theta_7', 0 \right), \quad (\text{A.3.11})$$

and

$$\bar{R}_3^7 = \left(\frac{a}{2} \cot \beta', \frac{a}{2}, 0 \right), \quad (\text{A.3.12})$$

where

$$\beta' = \left[\frac{-\frac{p}{2} + q^2 - \sqrt{q^4 - q^2 \left(p + \frac{1}{4} \right)}}{2(p^2 + q^2)} \right]^{1/2}, \quad (\text{A.3.13})$$

$$p = 4 \sin^2 \frac{\theta_7'}{2} - 1 + 2 \sin \frac{\theta_7'}{2} \cos \theta_7', \quad (\text{A.3.14})$$

and

$$q = 2 \sin \frac{\theta_7'}{2} \sin \theta_7'. \quad (\text{A.3.15})$$

Table A-3-1 lists the coordinates of C-atoms for each three ring cluster based on the assumptions of the DMM. In the notation of the first column of Table XIX, the first three digits denote the type of rings in the three ring cluster. The last digit indicates the ring which the central Kr atom is above. For example, the notation 566-6 indicates that the corresponding three ring cluster consists of one 5-membered ring and two 6-membered rings, and the Kr physisorption site is above one of the 6-membered rings. This notation will be used throughout this thesis. In the coordinates of C-atoms listed in Table XIX, the symmetric line of the polygon indicated by the last digit is in the xz-plane. The C-atom coordinates of arbitrary orientations of a three ring cluster are obtained by the rotation of the three ring cluster by an appropriate angle about z-axis.

TABLE XIX. (a) Coordinates of the C-atoms of convex DMM three ring clusters, (b) Coordinates of the C-atoms of concave DMM three ring clusters, and (c) Coordinates of the C-atoms of flat DMM three ring clusters.

(a) Coordinates of the C-atoms of convex DMM three ring clusters.

Convex Ring Cluster	Coordinates of C-atoms of DMM (Å)
555-5	(0,0,1.325),(1.328,0,0.819),(-0.665,-1.15,0.819), (1.487,-1.153,0),(0.255,-1.864,0),(-0.665,1.15,0.819), (0.255,1.864,0),(1.487,1.153,0),(-1.742,-0.711,0), (-1.742,0.711,0)
556-5	(0,0,1.632),(0.728,1.15,1.224),(0.728,-1.15,1.224), (1.91,0.711,0.564),(1.91,-0.711,0.564),(-1.351,0.167,1.224), (-1.459,1.423,0.564),(-1.247,-1.967,0), (-0.173,2.031,0.564),(0.105,-2.135,0.408), (-1.975,-0.816,0.408)
556-6	(0,0,1.632),(-1.361,0,1.224),(0.582,1.231,1.224), (-1.623,1.233,0.564),(-0.422,1.994,0.564), (0.582,-1.231,1.224),(-0.422,-1.994,0.564), (-1.623,-1.233,0.564),(1.747,1.231,0.408), (1.747,-1.231,0.408),(2.329,0,0)
557-5	(-2.07,-1.811,0),(0,0,1.626),(0.77,1.15,1.304), (2.019,0.711,0.783),(2.019,-0.711,0.783), (-1.357,0.275,1.304),(-1.425,1.598,0.783), (-0.11,2.138,0.783),(0.376,-2.309,0.58),(-2.279,-0.53,0.58), (-0.889,-2.603,0)
557-7	(2.657,-0.711,0),(0,0,1.626),(-1.384,0,1.304), (0.527,1.28,1.304),(-1.715,1.282,0.783),(-0.534,2.073,0.783), (0.527,-1.28,1.304),(-0.534,2.073,0.783),(0.527,-1.28,1.304), (-0.534,-2.073,0.783),(-1.715,-1.282,0.783), (1.709,1.598,0.58),(1.709,-1.598,0.58),(2.657,0.711,0)

566-5 (0,0,1.144),(0.783,1.15,0.858),(0.783,-1.15,0.858),
(-1.393,0,0.858),(2.056,0.711,0.395),(2.056,-0.711,0.395),
(-2.001,1.151,0.286),(0.176,2.302,0.286),(-1.217,2.302,0),
(0.176,-2.302,0.286),(-2.001,-1.151,0.286),(-1.217,-2.302,0)

566-6 (0,0,1.144),(0.651,-1.23,0.858),(-1.383,-0.155,0.858),
(0.65,1.231,0.858),(-0.332,-2.15,0.395),
(-1.589,-1.486,0.395),(1.953,1.231,0.286),
(-1.466,2.152,0),(1.953,-1.231,0.286),(2.604,0,0),
(-2.117,0.92,0.286),
(-0.082,2.307,0.286)

567-5 (0.235,2.41,0.309),(-2.103,-2.281,0),(0,0,0.762),
(-0.865,-2.98,0),(0.821,1.15,0.611),(0.821,-1.15,0.611),
(2.152,0.711,0.367),(2.152,-0.711,0.367),
(-1.409,0.108,0.611),(-1.997,1.368,0.309),
(-1.175,2.518,0.158),(0.437,-2.477,0.272),
(-2.346,-0.907,0.272)

567-6 (2.779,0,0.158),(-1.178,2.871,0),(0,0,0.762),
(0.695,-1.23,0.611),(-1.39,-0.257,0.611),
(-0.266,-2.251,0.367),(-1.554,-1.65,0.367),
(0.694,1.231,0.611),(2.084,1.231,0.309),
(2.084,-1.231,0.309),(-2.429,0.651,0.272),
(0.17,2.509,0.272),(-2.335,2.044,0)

567-7 (3.02,0.711,0),(3.02,-0.711,0),(0,0,0.762),
(-1.405,0.15,0.611),(-1.616,-2.261,0.158),
(0.599,1.28,0.611),(-1.677,1.525,0.367),
(-0.438,2.224,0.367),(0.599,-1.281,0.611),
(-0.21,-2.412,0.309),(-2.214,-0.98,0.309),
(1.942,1.598,0.272),(1.942,-1.598,0.272)

(b) Coordinates of the C-atoms of concave DMM three ring clusters.

Concave Ring Cluster	Coordinates of C-atoms of DMM (Å)
555-5	(0,0,-1.325),(1.328,0,-0.819),(0.665,-1.15,-0.819), (1.487,-1.153,0),(0.255,-1.864,0),(0.665,1.15,-0.819), (0.255,1.864,0),(1.487,1.153,0),(-1.742,-0.711,0), (-1.742,0.711,0)
556-5	(0,0,-1.632),(0.728,1.15,-1.224),(0.728,-1.15,-1.224), (1.91,0.711,-0.564),(1.91,-0.711,-0.564), (-1.351,0.167,-1.224),(-1.459,1.423,-0.564), (-0.173,2.031,-0.564),(0.105,-2.031,-0.408), (-1.975,-0.816,-0.408),(-1.247,-1.967,0)
556-6	(-1.361,0,-1.224),(0.582,1.231,-1.224),(-1.623,1.233,-0.564), (2.329,0,0),(-0.422,1.994,-0.564),(0.582,-1.231,-1.224), (-0.422,-1.994,-0.564),(-1.623,-1.233,-0.564),(0,0,-1.632), (1.747,-1.231,-0.408),(1.747,1.231,-0.408)
557-5	(-2.07,-1.811,0), (0,0,-1.626),(0.77,1.15,-1.304), (0.77,-1.15,-1.304),(2.019,0.711,-0.783), (2.019,-0.711,-0.783),(-1.357,0.275,-1.304), (-1.425,1.598,-0.783),(0.376,-2.309,-0.58), (-2.279,-0.53,-0.58),(-0.889,-2.603,0)
557-7	(2.657,-0.711,0),(0,0,-1.626),(-1.384,0,-1.304), (0.527,1.28,-1.304),(-1.715,1.282,-0.783), (-0.534,2.073,-0.783),(0.527,-1.28,-1.304), (0.527,-1.28,-1.304),(-0.534,2.073,-0.783), (-0.534,-2.073,-0.783),(-1.715,-1.282,-0.783), (2.657,0.711,0),(1.709,-1.598,-0.58),(1.709,1.598,-0.58)
566-5	(0,0,-1.144),(0.783,1.15,-0.858),(0.783,-1.15,-0.858), (-1.393,0,-0.858),(2.056,0.711,-0.395), (2.056,-0.711,-0.395),(-2.001,1.151,-0.286), (-1.217,-2.302,0),(0.176,2.302,-0.286),(-1.217,2.302,0), (0.176,-2.302,-0.286),(-2.001,-1.151,-0.286)

566-6 (0,0,-1.144),(-0.783,-1.15,-0.858),(-0.783,1.15,-0.858),
 (1.393,0,-0.858),(-2.056,-0.711,-0.395),
 (-2.056,0.711,-0.395),(2.001,-1.151,-0.286),
 (2.001,1.151,-0.286),(1.217,-2.302,0),(1.217,2.302,0),
 (-0.176,-2.302,-0.286)

567-5 (-1.175,2.518,-0.158),(-2.103,-2.281,0),(0,0,-0.762),
 (0.821,1.15,-0.611),(0.821,-1.15,-0.611),
 (2.152,0.711,-0.367),(2.152,-0.711,-0.367),
 (-1.409,0.108,-0.611),(-1.997,1.368,-0.309),
 (0.235,2.41,-0.309),(0.437,-2.477,-0.272),
 (-0.865,-2.98,0),(-2.346,-0.907,-0.272)

567-6 (2.799,0,-0.158),(-1.178,2.871,0),(0,0,-0.611),
 (0.695,-1.23,-0.611),(-1.39,-0.257,-0.611),
 (-0.266,-2.251,-0.367),(-1.554,-1.65,-0.367),
 (0.694,1.231,-0.611),(2.084,1.231,-0.309),
 (2.084,-1.231,-0.309),(-2.249,0.651,-0.272),
 (0.17,2.509,-0.272),(-2.335,2.044,0)

567-7 (3.02,0.711,0),(3.02,-0.711,0),(0,0,-0.762),
 (-1.405,0.15,-0.611),(-1.616,-2.261,-0.158),
 (0.599,1.28,-0.611),(-1.677,1.525,-0.367),
 (-0.438,2.224,-0.367),(0.599,-1.281,-0.611),
 (1.942,-1.598,-0.272),(-0.21,-2.412,-0.309),
 (-2.214,-0.98,-0.309),(1.942,1.598,-0.272)

(c) Coordinates of the C-atoms of flat DMM three ring clusters.

Flat Ring Cluster	Coordinates of C-atoms of DMM (Å)
577-5	(0,0,0),(0.851,-1.139,0),(0.851,1.139,0),(2.207,-0.711,0), (2.207,0.711,0),(-1.422,0,0),(-2.273,1.139,0), (-2.273,1.139,0),(0.0449,2.503,0),(-2.071,2.547,0), (-2.071,-2.547,0),(-0.8,3.183,0),(-0.8,-3.183,0)
577-7	(0,0,0),(0.637,-1.271,0),(0.637,1.271,0),(-1.4,-0.251,0), (-0.353,-2.292,0),(-1.624,-1.655,0),(2.307,-1.522,0), (2.307,1.522,0),(3.204,-0.711,0),(3.204,0.711,0), (-2.439,0.72,0),(0,2.543,0),(-2.488,2.141,0),(-1.349,2.992,0)
666-6	(0,0,0),(0.637,-1.271,0),(0.637,1.271,0),(-1.4,-0.251,0), (-0.353,-2.292,0),(-1.624,-1.655,0),(2.307,-1.522,0), (2.307,1.522,0),(3.204,-0.711,0),(3.204,0.711,0), (-2.439,0.72,0),(0,2.543,0),(-2.488,2.141,0),(-1.349,2.992,0)
667-6	(0,0,0),(0.741,-1.214,0),(0.741,1.214,0),(2.163,-1.214,0), (2.163,1.214,0),(-1.418,0.103,0),(-2.069,1.368,0), (0.09,2.478,0),(-1.328,2.582,0),(2.903,0,0),(0.183,-2.522,0), (-2.327,-0.991,0),(-1.091,-3.153,0),(-2.305,-2.413,0)
667-7	(0,0,0),(-1.421,0,0),(0.651,1.264,0),(-2.163,1.214,0), (-0.09,2.478,0),(0.651,-1.264,0),(-0.09,-2.478,0), (-2.163,-1.214,0),(-1.512,-2.478,0),(-1.512,2.478,0), (2.058,1.47,0),(2.058,-1.47,0),(3.26,0.711,0),(3.26,-0.71,0)
677-6	(-0.992,3.299,0),(0,0,0),(0.768,1.196,0),(0.768,-1.196,0), (2.19,1.196,0),(2.19,-1.196,0),(2.959,0,0),(-2.19,1.196,0), (0.177,2.49,0),(-2.24,2.618,0),(-1.421,0,0),(0.177,-2.49,0), (-2.19,-1.196,0),(-0.992,-3.299,0),(-2.24,-2.618,0)
677-7	(3.371,-0.711,0),(0,0,0),(0.682,-1.248,0),(-1.418,-0.101,0), (0,-2.496,0),(-2.1,-1.349,0),(-1.418,-2.597,0), (2.1,1.349,0),(2.1,-1.349,0),(3.371,0.711,0), (0.682,1.248,0),(-2.27,1.038,0),(0,2.496,0),(-2.42,2.452,0), (-1.223,3.221,0)

777-7. (-1.421,0,0),(3.456,-0.711,0),(0,0,0),(0.711,1.231,0),
(0.711,-1.231,0),(2.133,1.231,0),(2.133,-1.231,0),
(3.456,0.711,0),(-2.133,1.231,0),(0,2.463,0),(-2.344,2.638,0),
(-1.112,3.349,0),(0,-2.463,0),(-2.133,-1.231,0),
(-1.112,-3.349,0),(-2.344,-2.638,0)

APPENDIX 4: CALCULATION OF INTERACTION ENERGY BETWEEN
A Kr ATOM AND A SEMI-INFINITE GRAPHITE WITH
CMM

The parameters of the Kr - C-atom interaction potential:

$$\varepsilon = 9.32 \cdot 10^{-15} \text{ erg} \quad \sigma := 3.492 \text{ \AA}$$

The bulk density of graphite: $\rho_0 := 0.11284 \text{ atoms/\AA}^3$

The typical form of the Lennard-Jones 6-12 potential is given by

$$\phi(r) := 4 \cdot \varepsilon \cdot \left[\left(\frac{\sigma}{r} \right)^{12} - \left(\frac{\sigma}{r} \right)^6 \right]$$

In cylindrical coordinate system, the interaction energy between a Kr atom and a semi-infinite graphite CMM is given by

$$U(h) = \rho_0 \cdot 2 \cdot \pi \cdot \int_{-\infty}^0 \int_0^{\infty} 4 \cdot \varepsilon \cdot r \cdot \left[\left[\frac{\sigma^2}{(h-z)^2 + r^2} \right]^6 - \left[\frac{\sigma^2}{(h-z)^2 + r^2} \right]^3 \right] dr dz$$

$$U(h) = \frac{2}{45} \cdot \rho_0 \cdot \pi \cdot (2 \cdot \sigma^6 - 15 \cdot h^6) \cdot \varepsilon \cdot \frac{\sigma^6}{h^9}$$

To find the minimum interaction energy, we take the derivative and set it equal to zero.

The derivative is

$$\frac{d}{dh} \frac{2}{45} \cdot \rho_0 \cdot \pi \cdot (2 \cdot \sigma^6 - 15 \cdot h^6) \cdot \varepsilon \cdot \frac{\sigma^6}{h^9} = -4 \cdot \rho_0 \cdot \frac{\pi}{h^4} \cdot \varepsilon \cdot \sigma^6 - \frac{2}{5} \cdot \rho_0 \cdot \pi \cdot (2 \cdot \sigma^6 - 15 \cdot h^6) \cdot \varepsilon \cdot \frac{\sigma^6}{h^{10}}$$

We set the result of the derivative equal to zero, then

$$-4 \cdot \rho_0 \cdot \frac{\pi}{h^4} \cdot \varepsilon \cdot \sigma^6 - \frac{2}{5} \cdot \rho_0 \cdot \pi \cdot (2 \cdot \sigma^6 - 15 \cdot h^6) \cdot \varepsilon \cdot \frac{\sigma^6}{h^{10}} = 0$$

The roots of the equation are

$$\left[\begin{array}{c} \frac{1}{5} \cdot 2 \left(\frac{1}{6} \right) \cdot 5 \left(\frac{5}{6} \right) \cdot \sigma \\ \frac{1}{5} \cdot \left(\frac{1}{2} + \frac{1}{2} i \cdot \sqrt{3} \right) \cdot 2 \left(\frac{1}{6} \right) \cdot 5 \left(\frac{5}{6} \right) \cdot \sigma \\ \frac{1}{5} \cdot \left(\frac{-1}{2} + \frac{1}{2} i \cdot \sqrt{3} \right) \cdot 2 \left(\frac{1}{6} \right) \cdot 5 \left(\frac{5}{6} \right) \cdot \sigma \\ -\frac{1}{5} \cdot 2 \left(\frac{1}{6} \right) \cdot 5 \left(\frac{5}{6} \right) \cdot \sigma \\ \frac{1}{5} \cdot \left(\frac{-1}{2} - \frac{1}{2} i \cdot \sqrt{3} \right) \cdot 2 \left(\frac{1}{6} \right) \cdot 5 \left(\frac{5}{6} \right) \cdot \sigma \\ \frac{1}{5} \cdot \left(\frac{1}{2} - \frac{1}{2} i \cdot \sqrt{3} \right) \cdot 2 \left(\frac{1}{6} \right) \cdot 5 \left(\frac{5}{6} \right) \cdot \sigma \end{array} \right]$$

We will take the first solution since it is the only real and positive solution.

$$h_{\text{eq}} = \frac{1}{5} \cdot 2 \left(\frac{1}{6} \right) \cdot 5 \left(\frac{5}{6} \right) \cdot \sigma$$

The interaction energy between a Kr atom and CMM graphite at the height is given by

$$U(h_{\text{eq}}) = -9.886 \cdot 10^{-14} \text{ erg}$$

APPENDIX 5: INTERACTION ENERGY OF A SINGLE Kr ATOM WITH A
2D TRIANGULAR LATTICE OF Kr ATOMS

ORIGIN = 1

Basis vectors of representing the positions 2D triangular lattice of Kr atoms:

$$a_1 := \begin{pmatrix} 1 \\ 0 \\ 0 \end{pmatrix} \quad a_2 := \begin{bmatrix} \cos\left(\frac{\pi}{3}\right) \\ \sin\left(\frac{\pi}{3}\right) \\ 0 \end{bmatrix}$$

Indices indicating range of 2D triangular lattice unit cells which participate in the interaction energy calculation:

$$m := 1..10 \quad n := 1..10$$

Radial distance functions for the interaction energy calculation:

$$r_{1,m,n} := |m \cdot a_1 + n \cdot a_2| \quad : \text{radial distance function for the first quadrant}$$

$$r_{2,m,n} := |m \cdot a_1 - n \cdot a_2| \quad : \text{radial distance function for the fourth quadrant}$$

The parameters for the Kr-Kr interaction potential:

$$\varepsilon := 2.361 \cdot 10^{-14} \text{ erg} \quad \sigma := 3.6 \text{ \AA}$$

The Kr-Kr interaction potential is given by

$$\phi_{Kr}(r) = 4 \cdot \varepsilon \cdot \left[\left(\frac{\sigma}{r} \right)^{12} - \left(\frac{\sigma}{r} \right)^6 \right]$$

The interaction energy between a Kr atom at the origin and the Kr atoms on the x and y axes.

[Note] The angle between the positive x and y axes is 60°.

$$u_0(b) := 4 \cdot \left(\sum_{k=1}^{10} \phi_{Kr}(k \cdot b) \right)$$

The interaction energy between a Kr atom at the origin and the Kr atoms of the 2D triangular lattice except the Kr atoms on the x and y axes.

$$u_1(b) = 2 \cdot \sum_{m=1}^{10} \left[\sum_{n=1}^{10} \left(\phi_{Kr}(r_{1,m,n} \cdot b) + \phi_{Kr}(r_{2,m,n} \cdot b) \right) \right]$$

The total interaction energy of a single Kr atom with a 2D triangular lattice of Kr atom is the sum of u_1 and u_2 .

$$u_{total}(b) = u_0(b) + u_1(b)$$

Numerical calculation of the total interaction energy of a single Kr atom with a 2D triangular lattice of Kr atom:

Range of the nearest neighbor distance of a 2D triangular lattice:

$$b1 := 3.1, 3.2 \dots 5.0$$

$$b2 := 5.1, 5.2 \dots 7.0$$

$$b3 := 7.1, 7.2 \dots 9.0$$

$b1$ (Å)	$\frac{u_{total}(b1)}{10^{-14}}$ (erg)	$b2$ (Å)	$\frac{u_{total}(b2)}{10^{-14}}$ (erg)	$b3$ (Å)	$\frac{u_{total}(b3)}{10^{-14}}$ (erg)
3.1	193.751	5.1	-6.58	7.1	-1.007
3.2	111.196	5.2	-5.941	7.2	-0.927
3.3	59.754	5.3	-5.366	7.3	-0.854
3.4	27.849	5.4	-4.849	7.4	-0.788
3.5	8.285	5.5	-4.384	7.5	-0.728
3.6	-3.456	5.6	-3.967	7.6	-0.673
3.7	-10.231	5.7	-3.593	7.7	-0.623
3.8	-13.866	5.8	-3.257	7.8	-0.577
3.9	-15.528	5.9	-2.956	7.9	-0.535
4	-15.969	6	-2.686	8	-0.496
4.1	-15.674	6.1	-2.443	8.1	-0.461
4.2	-14.952	6.2	-2.224	8.2	-0.428
4.3	-14.004	6.3	-2.028	8.3	-0.398
4.4	-12.955	6.4	-1.85	8.4	-0.371
4.5	-11.884	6.5	-1.691	8.5	-0.346
4.6	-10.838	6.6	-1.546	8.6	-0.322
4.7	-9.843	6.7	-1.416	8.7	-0.301
4.8	-8.919	6.8	-1.298	8.8	-0.281
4.9	-8.066	6.9	-1.191	8.9	-0.263
5	-7.287	7	-1.095	9	-0.246

APPENDIX 6: CALCULATION OF POTENTIAL ENERGY SUMMATION
FOR A Kr ATOM ABOVE A CARBON RING

Calculations for Kr adsorbed on g-C

Main carbon ring size: 5

Adjacent carbon rings: 6,7

Ring cluster structure: Convex

Enter parameters for adsorbed gas and substrate:

Adatom-substrate separation [Å]:	$s_o := 1.00$	C atom radius [Å]:	$r_C := 0.91$
Interaction constant [erg-Å ⁶ /atom]:	$A := 67.6 \cdot 10^{-12}$	Kr atom radius [Å]:	$r_{Kr} := 1.03$
[Å]:	$r_o := 3.92$		
Average substrate density [atoms/Å ³]:	$\rho_o := 1.058 \cdot 10^{-1}$		
Density ratio between graphite and C1120:	$\rho_{ratio} := \frac{2.25}{2.11}$		
Number indicating the combination:	$N_{com} := 5+6+7$		
Index representing the C atoms in the ring cluster:	$i := 1..(N_{com}-5)$		

Set the coordinates for carbon atoms in the ring cluster: ORIGIN=1 TOL=1.0

sp ² bond length [Å]:	$l := 1.422$	$c := 6.714$	
Angles for pentagons, hexagons, and heptagons [radian]:	$\theta_5 := 3 \frac{\pi}{5}$	$\theta_6 := 4 \frac{\pi}{6}$	$\theta_7 := 5 \frac{\pi}{7}$
Radii of circles circumscribing the pentagon, the hexagon, and the heptagon:	$r_5 := \frac{\frac{1}{2}}{\cos\left(\frac{\theta_5}{2}\right)}$	$r_6 := \frac{\frac{1}{2}}{\cos\left(\frac{\theta_6}{2}\right)}$	$r_7 := \frac{\frac{1}{2}}{\cos\left(\frac{\theta_7}{2}\right)}$
Ring cluster height h and bond length d are given by the ring cluster geometry [Å]:		$d := 1.412$	$h := 0.151$
Angles for projected pentagons and the hexagon [radian]:	$\theta'_5 := \frac{108.898}{180} \pi$	$\theta'_6 := \frac{121.134}{180} \pi$	$\theta'_7 := \frac{129.968}{180} \pi$
Angles of the pentagons, the hexagon, and sp ² bond branch from z-axis [radian]:	$\Phi_5 := \arccos\left(\frac{h}{1 - \cos\left(\frac{\theta_5}{2}\right)}\right)$	$\Phi_7 := \arccos\left(\frac{h}{1 - \cos\left(\frac{\theta_7}{2}\right)}\right)$	
	$\Phi_6 := \arccos\left(\frac{h}{1 - \cos\left(\frac{\theta_6}{2}\right)}\right)$		$\phi := \operatorname{atan}\left(\frac{d}{b}\right)$

General formulae for carbon atom coordinates in a pentagon:

$$x_{51} := d \cdot \cos\left(\frac{\theta_5}{2}\right) \quad y_{51} := -1 \cdot \sin\left(\frac{\theta_5}{2}\right) \quad z_{51} := -1 \cdot \cos\left(\frac{\theta_5}{2}\right) \cdot \cos(\Phi_5)$$

$$x_{52} := -1 \cdot \left(\cos\left(\frac{\theta_5}{2}\right) + \cos\left(\theta_5 - \frac{\pi}{2}\right) \right) \cdot \sin(\Phi_5) \quad y_{52} := \frac{1}{2}$$

$$z_{52} := -1 \cdot \left(\cos\left(\frac{\theta_5}{2}\right) + \cos\left(\theta_5 - \frac{\pi}{2}\right) \right) \cdot \cos(\Phi_5)$$

General formulae for carbon atom coordinates in a hexagon:

$$x_{61} := d \cdot \cos\left(\frac{\theta_6}{2}\right) \quad y_{61} := -1 \cdot \sin\left(\frac{\theta_6}{2}\right) \quad z_{61} := -1 \cdot \cos\left(\frac{\theta_6}{2}\right) \cdot \cos(\Phi_6)$$

$$x_{62} := -1 \cdot \left(\cos\left(\frac{\theta_6}{2}\right) + 1 \right) \cdot \sin(\Phi_6) \quad y_{62} := -1 \cdot \sin\left(\frac{\theta_6}{2}\right) \quad z_{62} := -1 \cdot \left(\cos\left(\frac{\theta_6}{2}\right) + 1 \right) \cdot \cos(\Phi_6)$$

$$x_{63} := -1 \cdot \left(2 \cdot \cos\left(\frac{\theta_6}{2}\right) + 1 \right) \cdot \sin(\Phi_6) \quad y_{63} := 0 \quad z_{63} := -1 \cdot \left(2 \cdot \cos\left(\frac{\theta_6}{2}\right) + 1 \right) \cdot \cos(\Phi_6)$$

General formulae for carbon atom coordinates in a heptagon:

$$x_{71} := d \cdot \cos\left(\frac{\theta_7}{2}\right) \quad y_{71} := -1 \cdot \sin\left(\frac{\theta_7}{2}\right) \quad z_{71} := -1 \cdot \cos\left(\frac{\theta_7}{2}\right) \cdot \cos(\Phi_7)$$

$$x_{72} := -1 \cdot \left(\cos\left(\frac{\pi}{14}\right) + \cos\left(\frac{\theta_7}{2}\right) \right) \cdot \sin(\Phi_7) \quad y_{72} := -1 \cdot \left(\sin\left(\frac{\theta_7}{2}\right) + \sin\left(\frac{\pi}{14}\right) \right)$$

$$z_{72} := -1 \cdot \left(\cos\left(\frac{\pi}{14}\right) + \cos\left(\frac{\theta_7}{2}\right) \right) \cdot \cos(\Phi_7)$$

$$x_{73} := -1 \cdot \left(\cos\left(\frac{\pi}{14}\right) + \cos\left(3 \cdot \frac{\pi}{14}\right) + \cos\left(\frac{\theta_7}{2}\right) \right) \cdot \sin(\Phi_7) \quad y_{73} := \frac{1}{2}$$

$$z_{73} := -1 \cdot \left(\cos\left(\frac{\pi}{14}\right) + \cos\left(3 \cdot \frac{\pi}{14}\right) + \cos\left(\frac{\theta_7}{2}\right) \right) \cdot \cos(\Phi_7)$$

Define a rotation matrix:

$$R(\theta) := \begin{pmatrix} \cos(\theta) & -\sin(\theta) & 0 \\ \sin(\theta) & \cos(\theta) & 0 \\ 0 & 0 & 1 \end{pmatrix}$$

Define initial coordinate matrices of carbon atom positions in individual rings:

$$\eta'_5 := \begin{pmatrix} 0 & x_{51} & x_{51} & x_{52} & x_{52} \\ 0 & y_{51} & -y_{51} & y_{52} & -y_{52} \\ 0 & z_{51} & z_{51} & z_{52} & z_{52} \end{pmatrix} \quad \eta'_6 := \begin{pmatrix} 0 & x_{61} & x_{61} & x_{62} & x_{62} & x_{63} \\ 0 & y_{61} & -y_{61} & y_{62} & -y_{62} & y_{63} \\ 0 & z_{61} & z_{61} & z_{62} & z_{62} & z_{63} \end{pmatrix}$$

$$\eta'_7 := \begin{pmatrix} 0 & x_{71} & x_{71} & x_{72} & x_{72} & x_{73} & x_{73} \\ 0 & y_{71} & -y_{71} & y_{72} & -y_{72} & y_{73} & -y_{73} \\ 0 & z_{71} & z_{71} & z_{72} & z_{72} & z_{73} & z_{73} \end{pmatrix}$$

Matrices representing the coordinates of carbon atoms in the pentagon and the hexagons in three-ring cluster:

$$\eta_5 := \eta'_5 \quad \eta_6 := R\left(\frac{\theta_5}{2} + \frac{\theta_6}{2}\right) \cdot \eta'_6 \quad \eta_7 := R\left[-\left(\frac{\theta_5}{2} + \frac{\theta_7}{2}\right)\right] \cdot \eta'_7$$

Matrix representing the coordinates of carbon atoms in the three-ring cluster before correction:

$$\eta := \begin{bmatrix} \eta_{6,1,6} & \eta_{7,1,7} & 0 & \eta_{5,1,2} & \eta_{5,1,3} & \eta_{5,1,4} & \eta_{5,1,5} & \eta_{6,1,2} & \eta_{6,1,4} & \eta_{6,1,5} & \eta_{7,1,4} & \eta_{7,1,5} & \eta_{7,1,6} \\ \eta_{6,2,6} & \eta_{7,2,7} & 0 & \eta_{5,2,2} & \eta_{5,2,3} & \eta_{5,2,4} & \eta_{5,2,5} & \eta_{6,2,2} & \eta_{6,2,4} & \eta_{6,2,5} & \eta_{7,2,4} & \eta_{7,2,5} & \eta_{7,2,6} \\ \eta_{6,3,6} & \eta_{7,3,7} & 0 & \eta_{5,3,2} & \eta_{5,3,3} & \eta_{5,3,4} & \eta_{5,3,5} & \eta_{6,3,2} & \eta_{6,3,4} & \eta_{6,3,5} & \eta_{7,3,4} & \eta_{7,3,5} & \eta_{7,3,6} \end{bmatrix}$$

$$\eta = \begin{pmatrix} -1.175 & -2.103 & 0 & 0.821 & 0.821 & 2.152 & 2.152 & -1.409 & -1.997 & 0.235 & 0.437 & -2.346 & -0.865 \\ 2.518 & -2.281 & 0 & 1.15 & -1.15 & 0.711 & -0.711 & 0.108 & 1.368 & 2.41 & -2.477 & -0.907 & -2.98 \\ -0.604 & -0.762 & 0 & -0.151 & -0.151 & -0.395 & -0.395 & -0.151 & -0.453 & -0.453 & -0.49 & -0.49 & -0.762 \end{pmatrix}$$

Cylindrical radii of C atoms in the ring cluster [Å]:

$$\rho_i := \sqrt{(\eta_{1,i})^2 + (\eta_{2,i})^2}$$

Maximum of the cylindrical radii [Å]:

$$\rho_{\max} := \max(\rho^{<1>}) \quad \rho_{\max} = 3.103$$

Minimum of the z-component of C atom coordinates before correction [Å]:

$$z_{\min} := \min\left[\left(\eta^{\langle 3 \rangle}\right)\right] \quad z_{\min} = -0.762$$

Correcting matrix raising the C atom coordinates by amount of $-z_{\min}$:

$$Z_{\text{corr}} := (-1) \cdot \begin{pmatrix} 0 & 0 & 0 & 0 & 0 & 0 & 0 & 0 & 0 & 0 & 0 & 0 & 0 \\ 0 & 0 & 0 & 0 & 0 & 0 & 0 & 0 & 0 & 0 & 0 & 0 & 0 \\ z_{\min} & z_{\min} & z_{\min} & z_{\min} & z_{\min} & z_{\min} & z_{\min} & z_{\min} & z_{\min} & z_{\min} & z_{\min} & z_{\min} & z_{\min} \end{pmatrix}$$

Matrix representing the actual coordinates of C atoms in the three-ring cluster:

$$C := \eta + Z_{\text{corr}}$$

$$C = \begin{pmatrix} -1.175 & -2.103 & 0 & 0.821 & 0.821 & 2.152 & 2.152 & -1.409 & -1.997 & 0.235 & 0.437 & -2.346 & -0.865 \\ 2.518 & -2.281 & 0 & 1.15 & -1.15 & 0.711 & -0.711 & 0.108 & 1.368 & 2.41 & -2.477 & -0.907 & -2.98 \\ 0.158 & 0 & 0.762 & 0.611 & 0.611 & 0.367 & 0.367 & 0.611 & 0.309 & 0.309 & 0.272 & 0.272 & 0 \end{pmatrix}$$

Set up integration parameters and functions:

Set number of equally spaced values along
z-axis to evaluate:

$$M := 10$$

$$m := 1..M$$

Minimum hard core separation [Å]:

$$ZK_{r \min} := r_C + r_{Kr}$$

$$ZK_{r \min} = 1.94$$

Set x-axis index for Kr: $k := 1..13$

$$t := 2..13$$

Radial segment:

$$r_t := \frac{t-1}{6} r_5$$

$$r_1 := 0$$

x-, y-, z-coordinate components of Kr:

$$z_{Kr_m} := \left[(ZK_{r \min} + 1.56) + \frac{m}{M} s_0 \right]$$

$$y_{Kr} := 0$$

$$x_{Kr_{m,t}} := \frac{1}{\tan(\Phi_5)} \left(\frac{r_t}{\cos(\Phi_5)} + z_{Kr_m} + z_{\min} \right)$$

$$x_{Kr_{m,1}} := 0$$

Actual height:

$$AH_{m,t} := \frac{x_{Kr_{m,t}}}{\cos(\Phi_5)} - r_t \tan(\Phi_5)$$

$$AH_{m,1} := z_{Kr_m} + z_{\min}$$

z_{Kr_m}	r_k
3.6	0
3.7	0.202
3.8	0.403
3.9	0.605
4	0.806
4.1	1.008
4.2	1.21
4.3	1.411
4.4	1.613
4.5	1.814
	2.016
	2.218
	2.419

Enter data for radial distribution function (See Beeman, *et al. Phys. Rev. B30, 870 (1984)*):

Set number of data points in RDF: $N := 89$ $n := 1..N$
 $n1 := 1..30$ $n2 := 31..60$ $n3 := 61..N$
 Set limits in RDF [\AA]: $r_{\min} := 0.953$ $r_{\max} := 5.881$

Radii in RDF [\AA]:

$$r_n := \frac{-(n-1)}{N-1} (r_{\max} - r_{\min}) + r_{\min}$$

Enter RDF data:

$n1$	q_{n1}	$i_{n1} :=$	$n2$	q_{n2}	$i_{n2} :=$	$n3$	q_{n3}	$i_{n3} :=$
1	0.953	0	31	2.633	9.091	61	4.313	29.091
2	1.009	0.091	32	2.689	7.818	62	4.369	30.909
3	1.065	0.909	33	2.745	6.909	63	4.425	32.727
4	1.121	1.636	34	2.801	6.455	64	4.481	33.636
5	1.177	2.727	35	2.857	6.455	65	4.537	34.727
6	1.233	4.091	36	2.913	6.364	66	4.593	35.818
7	1.289	5.364	37	2.969	6.364	67	4.649	36.364
8	1.345	6.364	38	3.025	6.182	68	4.705	37.273
9	1.401	7.000	39	3.081	5.636	69	4.761	37.636
10	1.457	7.182	40	3.137	5.455	70	4.817	38.000
11	1.513	6.364	41	3.193	5.455	71	4.873	38.182
12	1.569	5.273	42	3.249	5.727	72	4.929	38.182
13	1.625	3.636	43	3.305	6.545	73	4.985	38.182
14	1.681	2.273	44	3.361	7.455	74	5.041	38.182
15	1.737	1.091	45	3.417	10.182	75	5.097	38.182
16	1.793	0.727	46	3.473	12.818	76	5.153	38.182
17	1.849	0.091	47	3.529	15.545	77	5.209	38.182
18	1.905	0	48	3.585	17.636	78	5.265	38.364
19	1.961	0.091	49	3.641	19.091	79	5.321	38.727
20	2.017	0.727	50	3.697	19.818	80	5.377	39.091
21	2.073	1.818	51	3.753	20.000	81	5.433	39.545
22	2.129	3.455	52	3.809	19.636	82	5.489	40.000
23	2.185	5.091	53	3.865	19.273	83	5.545	40.727
24	2.241	7.273	54	3.921	19.091	84	5.601	41.273
25	2.297	9.818	55	3.977	19.818	85	5.657	42.000
26	2.353	11.727	56	4.033	20.727	86	5.713	43.273
27	2.409	12.818	57	4.089	22.000	87	5.769	44.000
28	2.465	13.273	58	4.145	23.818	88	5.825	44.545
29	2.521	12.545	59	4.201	25.455	89	5.881	44.727
30	2.577	10.818	60	4.257	27.273			

Define radial distribution functions using linear interpolation between available data and using the average substrate density:

$$Q(r) := \text{if}(r > r_{\text{max}}, 4 \cdot \pi \cdot r^2 \cdot \rho_0, \text{interp}(q, j, r))$$

Radial distribution function for the first layer:

$$J(r) := \text{if}(3.65 < r, Q(r), 0)$$

Radial distribution function for other layers:

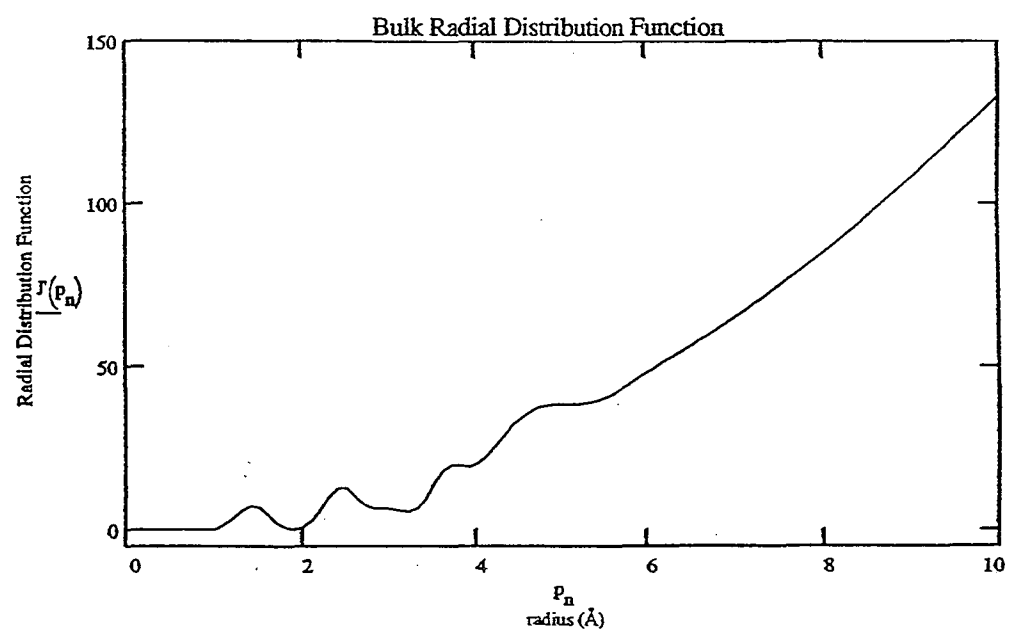
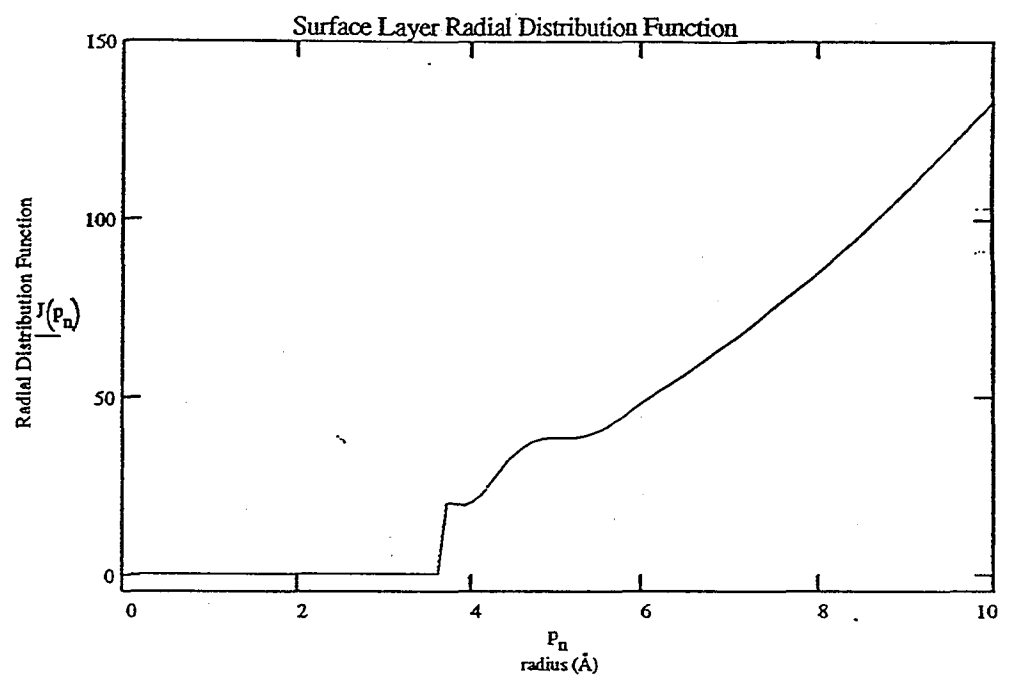
$$J(r) := \text{if}(r < r_{\text{min}}, 0, Q(r))$$

Testing of J(r) and J(r):

$$R := 10$$

$$n := 1..100$$

$$p_n := \frac{n}{100} \cdot R$$



Define RDF potential function:

Contribution from the first layer: [Note: The weighting factor $c/2$ comes from changing the volume density to the surface density.]

$$V_0 \text{ RDF}_{m,k} := \frac{c}{2} \int_{-r_{\max}}^{r_{\max}} \int_{-r_{\max}}^{r_{\max}} \left[\frac{J \sqrt{(x^2+y^2)}}{4\pi(x^2+y^2)} \left[\left[(x-x_{K_{r_m,k}})^2 + y^2 + (z_{K_{r_m}})^2 \right]^{-3} - \left(\frac{r_o}{2} \right)^6 \left[(x-x_{K_{r_m,k}})^2 + y^2 + (z_{K_{r_m}})^2 \right]^{-6} \right] \right] \cdot 10^{15} dy dx$$

$$V_1 \text{ RDF}_{m,k} := \frac{c}{2} \rho_o \int_{-50}^{-r_{\max}} \int_{-50}^{50} \left[\left[(x-x_{K_{r_m,k}})^2 + y^2 + (z_{K_{r_m}})^2 \right]^{-3} - \left(\frac{r_o}{2} \right)^6 \left[(x-x_{K_{r_m,k}})^2 + y^2 + (z_{K_{r_m}})^2 \right]^{-6} \right] \cdot 10^{15} dy dx$$

$$V_2 \text{ RDF}_{m,k} := \frac{c}{2} \rho_o \int_{-r_{\max}}^{r_{\max}} \int_{-50}^{-r_{\max}} \left[\left[(x-x_{K_{r_m,k}})^2 + y^2 + (z_{K_{r_m}})^2 \right]^{-3} - \left(\frac{r_o}{2} \right)^6 \left[(x-x_{K_{r_m,k}})^2 + y^2 + (z_{K_{r_m}})^2 \right]^{-6} \right] \cdot 10^{15} dy dx$$

$$V_3 \text{ RDF}_{m,k} := \frac{c}{2} \rho_o \int_{-r_{\max}}^{r_{\max}} \int_{r_{\max}}^{50} \left[\left[(x-x_{K_{r_m,k}})^2 + y^2 + (z_{K_{r_m}})^2 \right]^{-3} - \left(\frac{r_o}{2} \right)^6 \left[(x-x_{K_{r_m,k}})^2 + y^2 + (z_{K_{r_m}})^2 \right]^{-6} \right] \cdot 10^{15} dy dx$$

$$V_4 \text{ RDF}_{m,k} := \frac{c}{2} \rho_o \int_{r_{\max}}^{50} \int_{r_{\max}}^{50} \left[\left[(x-x_{K_{r_m,k}})^2 + y^2 + (z_{K_{r_m}})^2 \right]^{-3} - \left(\frac{r_o}{2} \right)^6 \left[(x-x_{K_{r_m,k}})^2 + y^2 + (z_{K_{r_m}})^2 \right]^{-6} \right] \cdot 10^{15} dy dx$$

$$V \text{ RDF} := V_0 \text{ RDF} + V_1 \text{ RDF} + V_2 \text{ RDF} + V_3 \text{ RDF} + V_4 \text{ RDF}$$

Contribution from the other layers: [Note] In V_{RDF} , the origin is located at the center of the second layer:

New z-coordinates for Kr atom caused by the transformation of the origin of the coordinates:

$$z'_{\text{Kr}_m} = z_{\text{Kr}_m} - \frac{c}{2}$$

$$V_{\text{RDF}_{m,k}} = \int_{-30}^{30} \int_{-30}^{30} \int_{-30}^0 \frac{J_1 \left[\sqrt{(x^2 + y^2 - z^2)} \right]}{4 \cdot \pi \cdot (x^2 + y^2 + z^2)} \left[(x - x_{\text{Kr}_{m,k}})^2 + y^2 + (z - z'_{\text{Kr}_m})^2 \right]^{-3} \cdot 10^{15} dz dy dx$$

Contribution from the C atom located at the center of the second layer:

$$V''_{\text{RDF}_{m,k}} = \left[\frac{r_0^6}{2} \left[\sqrt{(x_{\text{Kr}_{m,k}})^2 + (z'_{\text{Kr}_m})^2} \right]^{-12} \right] \cdot 10^{15}$$

$$U_{\text{RDF}_{m,k}} = (-A) \cdot (V_{\text{RDF}_{m,k}} - V'_{\text{RDF}_{m,k}} - V''_{\text{RDF}_{m,k}})$$

$$(-A) \cdot V_{\text{RDF}} = \begin{matrix} -54.95 & -57.74 & -59.52 & -61.72 & -64.32 & -67.27 & -70.53 & -74.03 & -77.7 & -81.46 & -85.22 & -88.9 & 92.43 \\ -52.18 & -54.86 & -56.53 & -58.58 & -61 & -63.75 & -66.8 & -70.1 & -73.6 & -77.21 & -80.89 & -84.56 & -88.17 \\ -49.54 & -52.1 & -53.66 & -55.56 & -57.81 & -60.36 & -63.2 & -66.29 & -69.57 & -73 & -76.52 & -80.07 & -83.61 \\ -47.02 & -49.47 & -50.91 & -52.68 & -54.76 & -57.12 & -59.75 & -62.61 & -65.67 & -68.88 & -72.19 & -75.56 & -78.95 \\ -44.62 & -46.95 & -48.3 & -49.93 & -51.84 & -54.02 & -56.45 & -59.09 & -61.92 & -64.89 & -67.98 & -71.13 & -74.32 \\ -42.34 & -44.57 & -45.8 & -47.31 & -49.07 & -51.08 & -53.3 & -55.73 & -58.33 & -61.07 & -63.92 & -66.85 & -69.81 \\ -40.18 & -42.29 & -43.44 & -44.82 & -46.44 & -48.27 & -50.31 & -52.54 & -54.92 & -57.44 & -60.05 & -62.74 & -65.47 \\ -38.12 & -40.12 & -41.18 & -42.46 & -43.93 & -45.62 & -47.48 & -49.52 & -51.69 & -53.99 & -56.38 & -58.84 & -61.34 \\ -36.18 & -38.06 & -39.04 & -40.21 & -41.58 & -43.1 & -44.81 & -46.66 & -48.65 & -50.74 & -52.92 & -55.16 & -57.43 \\ -34.33 & -36.11 & -37.01 & -38.09 & -39.33 & -40.74 & -42.29 & -43.97 & -45.77 & -47.68 & -49.66 & -51.69 & -53.76 \end{matrix}$$

$$(-A) \cdot V'_{\text{RDF}} = \begin{matrix} -8.775 & -8.809 & -8.831 & -8.857 & -8.889 & -8.925 & -8.966 & -9.011 & -9.06 & -9.112 & -9.168 & -9.226 & -9.287 \\ -8.455 & -8.488 & -8.508 & -8.533 & -8.563 & -8.596 & -8.634 & -8.676 & -8.721 & -8.769 & -8.821 & -8.874 & -8.93 \\ -8.15 & -8.181 & -8.2 & -8.224 & -8.251 & -8.283 & -8.318 & -8.356 & -8.398 & -8.443 & -8.49 & -8.54 & -8.591 \\ -7.858 & -7.888 & -7.906 & -7.928 & -7.954 & -7.983 & -8.015 & -8.051 & -8.09 & -8.131 & -8.175 & -8.221 & -8.269 \\ -7.579 & -7.608 & -7.625 & -7.645 & -7.669 & -7.696 & -7.727 & -7.76 & -7.796 & -7.834 & -7.875 & -7.917 & -7.961 \\ -7.312 & -7.34 & -7.356 & -7.375 & -7.398 & -7.423 & -7.451 & -7.482 & -7.515 & -7.551 & -7.588 & -7.628 & -7.668 \\ -7.057 & -7.084 & -7.099 & -7.117 & -7.138 & -7.161 & -7.187 & -7.216 & -7.247 & -7.28 & -7.315 & -7.351 & -7.389 \\ -6.813 & -6.839 & -6.853 & -6.87 & -6.889 & -6.911 & -6.936 & -6.962 & -6.991 & -7.021 & -7.054 & -7.087 & -7.122 \\ -6.579 & -6.604 & -6.618 & -6.633 & -6.651 & -6.672 & -6.695 & -6.719 & -6.746 & -6.774 & -6.804 & -6.836 & -6.868 \\ -6.355 & -6.38 & -6.392 & -6.407 & -6.424 & -6.443 & -6.464 & -6.487 & -6.512 & -6.538 & -6.566 & -6.595 & -6.625 \end{matrix}$$

$$(-A) \cdot V^m \text{ RDF} = \begin{bmatrix} -0.587 & -0.568 & -0.557 & -0.543 & -0.527 & -0.509 & -0.489 & -0.468 & -0.447 & -0.424 & -0.402 & -0.379 & -0.356 \\ -0.539 & -0.522 & -0.511 & -0.499 & -0.484 & -0.468 & -0.45 & -0.431 & -0.412 & -0.392 & -0.371 & -0.35 & -0.33 \\ -0.496 & -0.48 & -0.47 & -0.459 & -0.446 & -0.431 & -0.415 & -0.398 & -0.38 & -0.361 & -0.343 & -0.324 & -0.305 \\ -0.457 & -0.442 & -0.433 & -0.422 & -0.41 & -0.397 & -0.382 & -0.367 & -0.351 & -0.334 & -0.317 & -0.3 & -0.283 \\ -0.421 & -0.407 & -0.399 & -0.389 & -0.378 & -0.366 & -0.353 & -0.339 & -0.324 & -0.309 & -0.294 & -0.278 & -0.263 \\ -0.389 & -0.375 & -0.368 & -0.359 & -0.349 & -0.338 & -0.326 & -0.313 & -0.3 & -0.286 & -0.272 & -0.258 & -0.244 \\ -0.359 & -0.347 & -0.34 & -0.332 & -0.323 & -0.313 & -0.302 & -0.29 & -0.278 & -0.265 & -0.253 & -0.24 & -0.227 \\ -0.332 & -0.32 & -0.314 & -0.307 & -0.298 & -0.289 & -0.279 & -0.269 & -0.258 & -0.246 & -0.234 & -0.223 & -0.211 \\ -0.308 & -0.296 & -0.291 & -0.284 & -0.276 & -0.268 & -0.259 & -0.249 & -0.239 & -0.229 & -0.218 & -0.207 & -0.196 \\ -0.285 & -0.275 & -0.269 & -0.263 & -0.256 & -0.248 & -0.24 & -0.231 & -0.222 & -0.212 & -0.203 & -0.193 & -0.183 \end{bmatrix}$$

$$U \text{ RDF} = \begin{bmatrix} -64.31 & -67.11 & -68.91 & -71.12 & -73.73 & -76.7 & -79.98 & -83.51 & -87.21 & -91 & -94.79 & -98.5 & -102.1 \\ -61.17 & -63.87 & -65.55 & -67.61 & -70.04 & -72.81 & -75.88 & -79.21 & -82.73 & -86.38 & -90.08 & -93.79 & -97.43 \\ -58.18 & -60.76 & -62.33 & -64.25 & -66.5 & -69.08 & -71.94 & -75.04 & -78.35 & -81.8 & -85.35 & -88.93 & -92.51 \\ -55.33 & -57.8 & -59.25 & -61.03 & -63.12 & -65.5 & -68.15 & -71.03 & -74.11 & -77.34 & -80.68 & -84.08 & -87.5 \\ -52.62 & -54.97 & -56.32 & -57.96 & -59.89 & -62.09 & -64.53 & -67.19 & -70.04 & -73.03 & -76.15 & -79.33 & -82.55 \\ -50.04 & -52.28 & -53.52 & -55.04 & -56.82 & -58.84 & -61.08 & -63.52 & -66.15 & -68.91 & -71.78 & -74.73 & -77.72 \\ -47.59 & -49.72 & -50.88 & -52.26 & -53.9 & -55.75 & -57.8 & -60.04 & -62.45 & -64.98 & -67.62 & -70.33 & -73.08 \\ -45.27 & -47.28 & -48.35 & -49.64 & -51.12 & -52.82 & -54.7 & -56.75 & -58.94 & -61.26 & -63.67 & -66.15 & -68.67 \\ -43.06 & -44.96 & -45.95 & -47.13 & -48.5 & -50.04 & -51.76 & -53.63 & -55.63 & -57.74 & -59.94 & -62.2 & -64.5 \\ -40.97 & -42.76 & -43.67 & -44.76 & -46.01 & -47.43 & -49 & -50.69 & -52.51 & -54.43 & -56.43 & -58.48 & -60.57 \end{bmatrix}$$

Define the distances between C-atoms in the ring cluster and the Kr atom:

$$D1_{m,k} := \sqrt{(C_{1,1-x} Kr_{m,k})^2 + (C_{2,1-y} Kr)^2 + (C_{3,1-z} Kr_m)^2}$$

$$D2_{m,k} := \sqrt{(C_{1,2-x} Kr_{m,k})^2 + (C_{2,2-y} Kr)^2 + (C_{3,2-z} Kr_m)^2}$$

$$D3_{m,k} := \sqrt{(C_{1,3-x} Kr_{m,k})^2 + (C_{2,3-y} Kr)^2 + (C_{3,3-z} Kr_m)^2}$$

$$D4_{m,k} := \sqrt{(C_{1,4-x} Kr_{m,k})^2 + (C_{2,4-y} Kr)^2 + (C_{3,4-z} Kr_m)^2}$$

$$D5_{m,k} := \sqrt{(C_{1,5-x} Kr_{m,k})^2 + (C_{2,5-y} Kr)^2 + (C_{3,5-z} Kr_m)^2}$$

$$D6_{m,k} := \sqrt{(C_{1,6-x} Kr_{m,k})^2 + (C_{2,6-y} Kr)^2 + (C_{3,6-z} Kr_m)^2}$$

$$D7_{m,k} := \sqrt{(C_{1,7-x} Kr_{m,k})^2 + (C_{2,7-y} Kr)^2 + (C_{3,7-z} Kr_m)^2}$$

$$D8_{m,k} := \sqrt{(C_{1,8-x} Kr_{m,k})^2 + (C_{2,8-y} Kr)^2 + (C_{3,8-z} Kr_m)^2}$$

$$D9_{m,k} := \sqrt{(C_{1,9-x} Kr_{m,k})^2 + (C_{2,9-y} Kr)^2 + (C_{3,9-z} Kr_m)^2}$$

$$D10_{m,k} := \sqrt{(C_{1,10-x} Kr_{m,k})^2 + (C_{2,10-y} Kr)^2 + (C_{3,10-z} Kr_m)^2}$$

$$D11_{m,k} := \sqrt{(C_{1,11-x} Kr_{m,k})^2 + (C_{2,11-y} Kr)^2 + (C_{3,11-z} Kr_m)^2}$$

$$D12_{m,k} := \sqrt{(C_{1,12-x} Kr_{m,k})^2 + (C_{2,12-y} Kr)^2 + (C_{3,12-z} Kr_m)^2}$$

$$D13_{m,k} := \sqrt{(C_{1,13-x} Kr_{m,k})^2 + (C_{2,13-y} Kr)^2 + (C_{3,13-z} Kr_m)^2}$$

Define the nearest neighbor interaction potential:

$$U_{nn,m,k} = A \cdot 10^{15} \left[\left(\frac{r_o}{D_{1m,k}} \right)^6 - \left(\frac{r_o}{2D_{1m,k}} \right)^{12} + \left(\frac{r_o}{D_{2m,k}} \right)^6 - \left(\frac{r_o}{2D_{2m,k}} \right)^{12} + \left(\frac{r_o}{D_{3m,k}} \right)^6 - \left(\frac{r_o}{2D_{3m,k}} \right)^{12} + \left(\frac{r_o}{D_{4m,k}} \right)^6 - \left(\frac{r_o}{2D_{4m,k}} \right)^{12} + \left(\frac{r_o}{D_{5m,k}} \right)^6 - \left(\frac{r_o}{2D_{5m,k}} \right)^{12} + \left(\frac{r_o}{D_{6m,k}} \right)^6 - \left(\frac{r_o}{2D_{6m,k}} \right)^{12} + \left(\frac{r_o}{D_{7m,k}} \right)^6 - \left(\frac{r_o}{2D_{7m,k}} \right)^{12} + \left(\frac{r_o}{D_{8m,k}} \right)^6 - \left(\frac{r_o}{2D_{8m,k}} \right)^{12} + \left(\frac{r_o}{D_{9m,k}} \right)^6 - \left(\frac{r_o}{2D_{9m,k}} \right)^{12} + \left(\frac{r_o}{D_{10m,k}} \right)^6 - \left(\frac{r_o}{2D_{10m,k}} \right)^{12} + \left(\frac{r_o}{D_{11m,k}} \right)^6 - \left(\frac{r_o}{2D_{11m,k}} \right)^{12} + \left(\frac{r_o}{D_{12m,k}} \right)^6 - \left(\frac{r_o}{2D_{12m,k}} \right)^{12} + \left(\frac{r_o}{D_{13m,k}} \right)^6 - \left(\frac{r_o}{2D_{13m,k}} \right)^{12} \right]$$

311.1	225.1	180.4	137.1	99	67.72	43.25	24.38	9.49	-2.913	-13.77	-23.37	-31.55	
149.3	97.74	71.34	45.81	23.4	5.161	-8.853	-19.3	27.12	-33.2	-38.12	-42.1	45.09	
51.04	20.45	5.096	-9.616	-22.34	-32.42	39.8	-44.84	48.12	50.17	-51.36	-51.86	-51.69	
-7.761	-25.45	-34.08	-42.16	-48.91	-53.9	57.09	-58.73	-59.14	-58.67	-57.58	-55.99	-53.97	
41.92	-51.6	-56.12	-60.14	-63.2	-65.04	-65.65	-65.16	-63.82	-61.85	-59.42	-56.65	-53.59	
$U_{nn} =$	-60.65	-65.33	-67.34	-68.89	-69.7	-69.62	-68.66	-66.92	-64.56	-61.74	-58.59	-55.2	-51.64
	-69.74	-71.31	-71.8	-71.86	-71.32	-70.11	-68.25	-65.81	-62.91	-59.67	-56.19	-52.55	-48.82
	-72.87	-72.51	-72.1	-71.28	-69.96	-68.12	-65.78	-63	-59.87	-56.48	-52.93	-49.27	-45.57
	-72.37	-70.83	-69.9	-68.59	-66.86	-64.71	-62.16	-59.26	-56.1	-52.74	-49.26	-45.72	-42.17
	-69.72	-67.49	-66.29	-64.73	-62.82	-60.55	-57.95	-55.09	-52.01	-48.79	-45.48	-42.13	-38.79

Total potential is given by:

$$U_{total,m,k} = U_{RDF,m,k} + U_{nn,m,k}$$

246.79	157.99	111.49	65.98	25.27	-8.98	36.73	59.13	77.72	93.913	-108.56	-121.87	133.65	
88.13	33.87	5.79	-21.8	-46.64	-67.649	-84.733	-98.51	-109.85	-119.58	-128.2	-135.89	-142.52	
-7.14	-40.31	-57.234	-73.866	-88.84	-101.5	-111.74	-119.88	-126.47	-131.97	-136.71	-140.79	-144.2	
-63.091	-83.25	-93.33	-103.19	-112.03	-119.4	-125.24	-129.76	-133.25	-136.01	-138.26	-140.07	-141.47	
-94.54	-106.57	-112.44	-118.1	-123.09	-127.13	-130.18	-132.35	-133.86	-134.88	-135.57	-135.98	-136.14	
$U_{total} =$	-110.69	-117.61	-120.86	-123.93	-126.52	-128.46	-129.74	-130.44	-130.71	-130.65	-130.37	-129.93	-129.36
	-117.33	-121.03	-122.68	-124.12	-125.22	-125.86	-126.05	-125.85	-125.36	-124.65	-123.81	-122.88	-121.9
	-118.14	-119.79	-120.45	-120.92	-121.08	-120.94	-120.48	-119.75	-118.81	-117.74	-116.6	-115.42	-114.24
	-115.43	-115.79	-115.85	-115.72	-115.36	-114.75	-113.92	-112.89	-111.73	-110.48	-109.2	-107.92	-106.67
	-110.69	-110.25	-109.96	-109.49	-108.83	-107.98	-106.95	-105.78	-104.52	-103.22	-101.91	-100.61	-99.36

List results:

$$U_{\min_k} := \min(U_{\text{total}} \langle k \rangle)$$

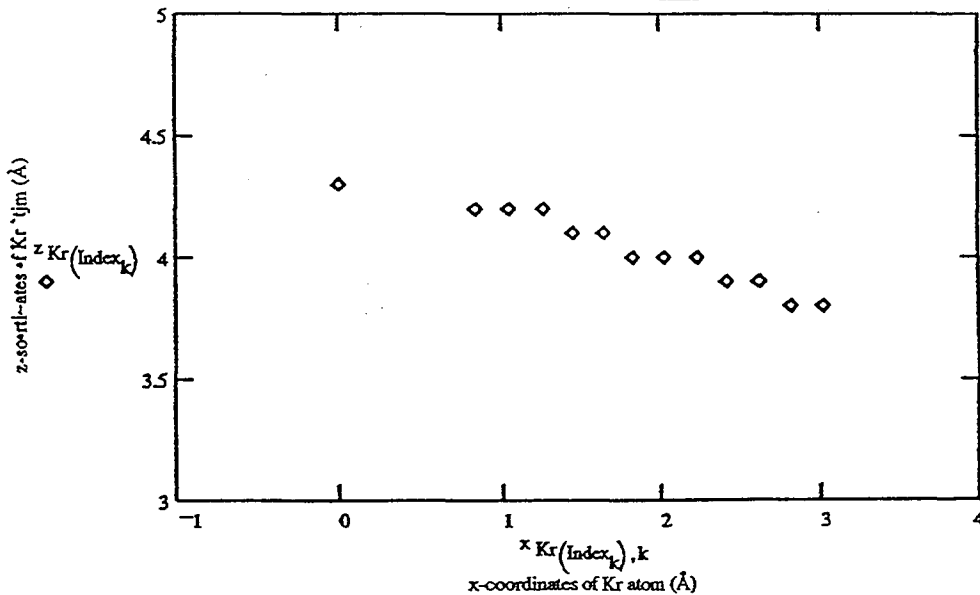
$$\text{Index}_k := \sum_m \text{if}(U_{\text{total}_m, k} = U_{\min_k}, m, 0)$$

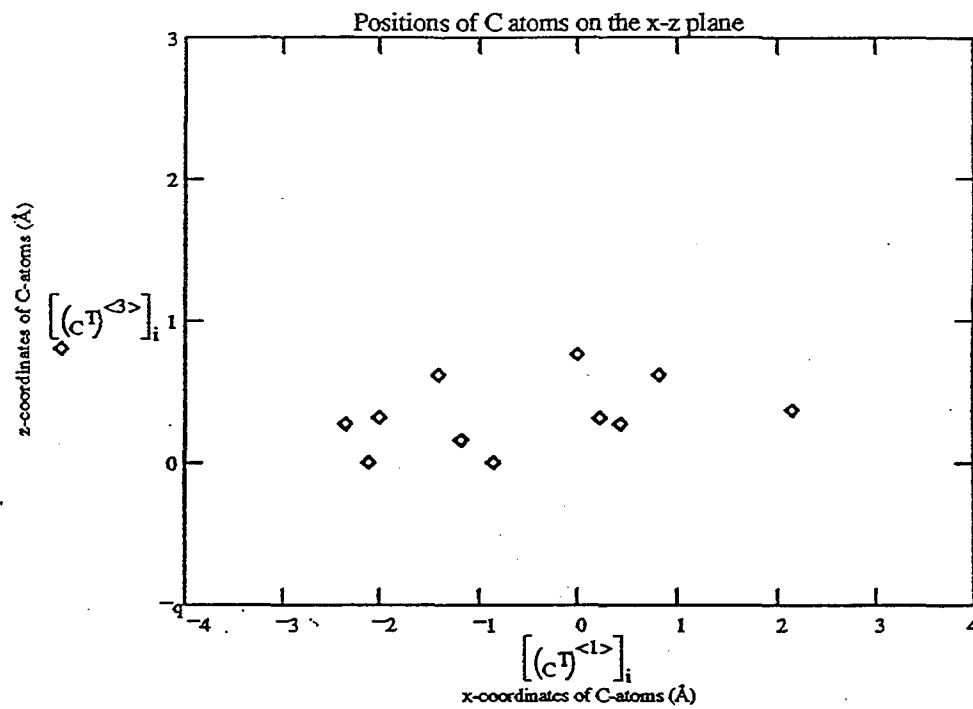
FILE: J567530

Index _k	AH(Index _k), k	U _{min_k}	z _{Kr} (Index _k)	x _{Kr} (Index _k), k	r _k	z _{Kr_m}
8	3.538	-118.14	4.3	0	0	3.6
7	3.532	-121.031	4.2	0.836	0.202	3.7
7	3.569	-122.68	4.2	1.041	0.403	3.8
7	3.606	-124.126	4.2	1.246	0.605	3.9
6	3.542	-126.517	4.1	1.433	0.806	4
6	3.579	-128.458	4.1	1.638	1.008	4.1
5	3.514	-130.173	4	1.825	1.21	4.2
5	3.551	-132.352	4	2.03	1.411	4.3
5	3.588	-133.858	4	2.235	1.613	4.4
4	3.523	-136.01	3.9	2.421	1.814	4.5
4	3.56	-138.258	3.9	2.626	2.016	
3	3.496	-140.798	3.8	2.813	2.218	
3	3.533	-144.204	3.8	3.018	2.419	

$$C = \begin{pmatrix} -1.175 & -2.103 & 0 & 0.821 & 0.821 & 2.152 & 2.152 & -1.409 & -1.997 & 0.235 & 0.437 & -2.346 & -0.865 \\ 2.518 & -2.281 & 0 & 1.15 & -1.15 & 0.711 & -0.711 & 0.108 & 1.368 & 2.41 & -2.477 & -0.907 & -2.98 \\ 0.158 & 0 & 0.762 & 0.611 & 0.611 & 0.367 & 0.367 & 0.611 & 0.309 & 0.309 & 0.272 & 0.272 & 0 \end{pmatrix}$$

Kr atom positions where U_{min}'s are located





Print data files
for J567530:

WRITEPRN(JUR56730) :=U RDF

WRITEPRN(JUN56730) :=U_m

WRITEPRN(JU56730) :=U_{total}

WRITEPRN(JR156730) :=-A·V RDF

WRITEPRN(JR256730) :=-A·V' RDF

WRITEPRN(JR356730) :=-A·V'' RDF

WRITEPRN(JV056730) :=-A·V0 RDF

WRITEPRN(JV156730) :=-A·V1 RDF

WRITEPRN(JV256730) :=-A·V2 RDF

WRITEPRN(JV356730) :=-A·V3 RDF

WRITEPRN(JV456730) :=-A·V4 RDF